

12-2021

Synthesis of Polyethylene Glycol-Based Hydrogels and Silver/Gold Nanostructures for Biomedical Applications

Isabelle Ishimwe Niyonshuti
University of Arkansas, Fayetteville

Follow this and additional works at: <https://scholarworks.uark.edu/etd>

 Part of the [Nanoscience and Nanotechnology Commons](#), [Polymer and Organic Materials Commons](#), and the [Polymer Chemistry Commons](#)

Citation

Niyonshuti, I. I. (2021). Synthesis of Polyethylene Glycol-Based Hydrogels and Silver/Gold Nanostructures for Biomedical Applications. *Graduate Theses and Dissertations* Retrieved from <https://scholarworks.uark.edu/etd/4285>

This Dissertation is brought to you for free and open access by ScholarWorks@UARK. It has been accepted for inclusion in Graduate Theses and Dissertations by an authorized administrator of ScholarWorks@UARK. For more information, please contact scholar@uark.edu, uarepos@uark.edu.

Synthesis of Polyethylene Glycol-Based Hydrogels and Silver/Gold Nanostructures for
Biomedical Applications

A dissertation submitted in partial fulfillment
of the requirements for the degree of
Doctor of Philosophy in Chemistry

by

Isabelle I. Niyonshuti
Spelman College
Bachelor of Science in Biochemistry, 2016

December 2021
University of Arkansas

This dissertation is approved for recommendation to the Graduate Council

Jingyi Chen, Ph.D.
Dissertation Director

Roger Koeppe, Ph.D.
Committee Member

Kyle Quinn, Ph.D.
Committee Member

Yong Wang, Ph.D.
Committee Member

Suresh Thallapuram, Ph.D.
Committee Member

Colin D. Heyes, Ph.D.
Committee Member

Abstract

This work focuses on the synthesis of biocompatible polyethylene glycol (PEG)-based hydrogels, silver nanoparticles (AgNPs), and silver-gold nanocages (Ag-AuNCs) for biomedical applications. The dissertation includes two parts with Part I on the work of PEG-based hydrogel for wound healing applications and Part II on the work of Ag/Au nanostructures for antimicrobial applications. Part I studies PEG-based hydrogel for the delivery of fibroblast growth factors (FGFs) for wound healing applications, aiming to overcome the challenge of designing hydrogels capable of the sustained release of bioactive FGFs. This research develops new biocompatible anionic injectable hydrogel formulations based on Poly (Oligo Ethylene Glycol Monoacrylate- Acrylic Acid- N-Isopropylacrylamide) (POEGA-AA-NIPAM) using a simple and robust free-radical polymerization reaction. Chemical and physical properties of these hydrogels were characterized while feasibility for controlled release of FGFs from these hydrogels was examined *in vitro*. P(OEGA-AA-NIPAM) hydrogels were able to achieve sustained release of active human acidic FGF (hFGF1) which improved wound healing *in vivo*. This study promises a delivery system with tunable charge distribution for the delivery of active positively charged proteins for wound healing applications. Part II explores the effects of surface chemistry, morphology, and composition of Ag/Au nanostructures on their antimicrobial properties. It was found that the positively charged AgNPs caused a reorganization of histone-like nucleoid structuring (H-NS) protein of *E. coli*, resulting in enhanced antimicrobial activity while polydopamine (PDA) coating could synergize with AgNPs to increase antimicrobial killing against *E. coli*. The synergistic effect of PDA on antimicrobial activity of AgNPs that spectroscopic studies revealed to be from coordination of catechol group of PDA and Ag in the coating to generate reactive oxygen species (ROS). Further, Ag-AuNCs with different Ag/Au

molar ratios showed higher antimicrobial activity than pure AgNPs unveiling a synergistic effect between Au and AgNPs that depends on the Ag/Au composition and morphology of the alloy. This study provides insights on tailoring the antimicrobial properties of Ag/Au nanostructures through nanochemistry.

Acknowledgements

I would like to thank my mentor and advisor, Professor Jingyi Chen, for being a constant source of support and giving me opportunities that challenged me to learn. Her enthusiastic passion for science and patience to teach has made me a better scientist. I would like to thank my committee members Profs. Roger Koeppe, Colin Heyes, Suresh Thallapuram, Kyle Quinn and Yong Wang for their helpful suggestions, constructive criticisms, and advice during this journey. Special thanks to Prof. Colin Heyes for mentoring me during the 2015 summer as REU student at the University of Arkansas which shaped my interests and paved ways for graduate school studies. I offer my sincerest thanks to all my labmates for making lab a good environment to work and their friendships. I thank all collaborators and coauthors Dr. Ravi Kumar, Dr. Shilpi Agrawal, Dr. Jake Jones, Gianna Busch, Venkata Krishnamurthi, Ariel Rogers and Meaad Alqahtany for their contributions to this work. I would like to thank Felix Nyarugabo who saw potential in me at early age, supported and gave me opportunities to further my education. I would like to thank all my family members and friends for their prayers and support that helped me throughout the journey.

Dedication

This dissertation is dedicated to my mother, Verediane Mukabatangineza, and my father, Faustin Nkundabatware who have always believed in me, supported, and inspired me to accomplish my dreams and higher goals.

Table of Contents

Chapter I: Introduction	1
1.1. Polyethylene glycol-based injectable hydrogels for wound healing applications	1
Polyethylene glycol (PEG)-based hydrogels	1
Injectable hydrogels	4
Controlled delivery of Proteins from PEG-based injectable hydrogels	6
Fibroblast growth factors in wound healing	8
Current challenges of using hydrogels.....	10
1.2. Silver nanoparticles for antimicrobial applications	11
General biomedical applications of silver and silver nanoparticles.....	11
Antimicrobial applications of silver nanoparticles	13
Mechanisms guiding antimicrobial activity of silver nanoparticles	14
Effect of size on silver nanoparticles' antimicrobial performance	15
Effect of shape on AgNPs antimicrobial performance	16
Effect of surface chemistry on antimicrobial properties of silver nanoparticles ..	17
Overview of this research	20
References.....	21
Chapter II: Biocompatible, Injectable based on Poly (Oligo Ethylene Glycol Monoacrylate- Acrylic Acid- N-Isopropylacrylamide) Anionic Hydrogel for Delivery of Fibroblast Growth Factors to Enhance Wound Healing*	33
Abstract.....	33
Introduction.....	34
Experimental methods	38
Results and discussion	43
References.....	59

Appendix A: Supplemental information	64
Appendix B: Controlled release of proteins from injectable P(OEGA- <i>co</i> -AA) hydrogel*	66
Chapter III. Polydopamine Surface Coating Synergizes the Antimicrobial Activity of Silver Nanoparticles*	70
Abstract	70
Introduction	71
Results and Discussion	79
Conclusion	93
References	95
Appendix A: Supporting Information	102
Appendix B: Surface Modification of AgNPs with different polymeric ligands for antimicrobial applications	104
Overview	104
Introduction	105
Experimental methods, ligand exchange methods for surface modification of AgNPs with different polymeric ligands	106
Part 1: Results and Discussion	107
Conclusion	111
References	102
Appendix C. Effects on stability of AgNPs with different polymeric ligands	113
Overview	113
Introduction	113
Experimental Methods	114
Part 2: Results and Discussion	115
References	122

Chapter IV: Towards understanding the antimicrobial properties of silver/gold alloy nanocages against <i>Escherichia coli</i>*	123
Abstract	123
Introduction	124
Experimental methods	126
Results and Discussion	129
Conclusion	139
References	140
Appendix: Supplemental information: Effect of shape on antimicrobial properties of Ag and Au nanostructures	144
References	155
Chapter V: Conclusion and Future Work	156
References	158

List of Abbreviations

Ag	Silver
AgNC	Silver nanocubes
Ag-AuNCs	Silver-gold alloy nanocages
Au	Gold
AuNPs	Gold nanoparticles
AgNPs	Silver nanoparticles
AuNSts	Gold nanostars
AuNTs	Gold nanotriangles
BSA	Bovine serum albumin
FGF	Fibroblast growth factor
hFGF1	human acidic fibroblast growth factor
Dh	Hydrodynamic diameter
DLS	Dynamic light scattering
LSPR	Localized surface plasmon resonance
PBS	Phosphate buffered saline
PDA	Polydopamine
PVP	Polyvinylpyrrolidone
PDT	Photodynamic therapy
PEG	Poly (ethylene glycol)
POEGA	Poly (oligo ethylene Glycol Monoacrylate)
PEI	Poly(ethyleneimine)
PNIPAM	Poly (N-isopropyl acrylamide)

MBAm	N,N'-Methylenebisacrylamide
APS	Ammonium persulfate
LCST	Low critical solution temperature
AgNO ₃	Silver nitrate
E. coli	Escherichia coli
PDA-AgNPs	Polydopamine coated AgNPs
DNA	Deoxyribonucleic acid
AA	Acrylic acid
H-NS	Histone-like nucleoid structuring protein
ROS	Reactive oxygen species
ICP-MS	Inductively coupled plasma mass Spectrometry
STEM	Scanning-tunneling electron microscopy
TEM	Transmission electron microscopy
UV-Vis	Ultraviolet-visible
NIR	Near-infrared
DSC	Differential scanning calorimetry
TGA	Thermogravimetric analysis
XPS	X-Ray photoelectron spectroscopy
CTAC	Hexadecyltrimethylammonium
CTAB	Cetrimonium bromide

List of Figures

Chapter I

Figure 1: Chemical structure of PEG	4
Figure 2: Schematic representation of injectable hydrogels	5
Figure 3: Mechanisms of release of proteins from hydrogels	8
Figure 4: Designing hydrogel for controlled delivery of drugs	9
Figure 5: FGFs in wound healing	10
Figure 6: Structure of bacterial cell wall and antimicrobial mechanisms of NPs	13
Figure 7: Antimicrobial mechanism of AgNPs	15
Figure 8: Properties of AgNPs affecting their antimicrobial activity	15

Chapter II

Figure 1: Schematic of synthesis of P(OEGA-AA-NIPAM) hydrogel	44
Figure 2: FTIR absorbance spectra of P(OEGA-AA-NIPAM) hydrogels	47
Figure 3: DSC and TGA of P(OEGA-AA-NIPAM) copolymers	49
Figure 4: Swelling and degradation studies of P(OEGA-AA-NIPAM), Gel 8	51
Figure 5: MTT assay viability data for PEG-based hydrogels	52
Figure 6: hFGF1 release profiles from Gel 8	55
Figure 7: In vivo study for wound healing	57
Figure S1: Photograph of injectable hydrogels	64
Figure S2: Raman spectrum of P(OEGA-AA-NIPAM) hydrogel, Gel 8	64
Figure S3: Release profiles of hFGF1 from P(OEGA-AA-NIPMA) hydrogels	65
Figure S4: Release profiles of FGFs mutations	65
Figure S5: Controlled release of lysozyme P(OEGA-co-AA) hydrogel	66

Figure S6: SDS-PAGE of release Lysozyme	67
Figure S7: Controlled release of hFGF1 from P(OEGA- <i>co</i> -AA) hydrogel	67
Figure S8: Controlled release of hFGF1 from P(OEGA- <i>co</i> -AA) at different anionic strengths	68
Figure S9: SDS-PAGE of hFGF1 from P(OEGA- <i>co</i> -AA) hydrogel	68
Figure S10: Release profile of hFGF1 from Gel 8 and Gel 900	69

Chapter III

Figure 1: Schematic representation of PDA deposition on AgNPs	80
Figure 2: UV-Vis spectra and XPS data of PDA-AgNPs	82
Figure 3: Fluorescence-based growth curves of bacteria treated with PDA-AgNPs	83
Figure 4: Fluorescence-based growth curves of bacteria treated with PDA with no AgNPs	84
Figure 5: Dependence of the heights and locations of the fluorescence growth curves	85
Figure 6: XPS of Ag 3d and O 1s	87
Figure 7: FTIR spectra of samples with and without AgNPs	89
Figure 8: Promoted ROS generation	91
Figure 9: Higher membrane damage caused by PDA-AgNPs	92
Figure S1: TEM characterization of DA-AgNPs	102
Figure S2: PD growth curves of bacteria treated with PDA-AgNPs, AgNPs and DA	103
Figure S3: XPS of deconvoluted spectra of o 1s for different samples	103
Figure S4: Fluorescence and SEM images of bacteria and AgNPs	104
Figure S5: Schematic representation of ligand exchange to make PEI-AgNPs	107
Figure S6: UV-vis spectra and TEM images of AgNPs coated with different polymers	109
Figure S7: UV-vis spectra and TEM images of AgNplates coated with different polymers	110
Figure S8: Experimental set up for evaluation of stability of AgNPs	113

Figure S9: UV-vis spectra of PVP-AgNPs at different time points	116
Figure S10: UV-vis spectra of PEI-AgNPs at different time points	117
Figure S11: UV-vis spectra of PEG-AgNPs at different time points	118
Figure S12: UV-vis spectra of PVP-AgNPs stored in solution and powder form	119
Figure S13: UV-vis spectra of PEI-AgNPs stored in solution and powder form	119
Figure S14: UV-vis spectra of PEG-AgNPs stored in solution and powder form	120
Figure S15: UV-Vis and TEM images showing size-dependent stability of PVP-AgNPs	121

Chapter IV

Figure 1: TEM and UV vis of AgNC used to make Ag-AuNCs	130
Figure 2: Schematic representation of galvanic replacement reaction to make Ag-AuNCs	131
Figure 3: Photography and UV -Vis spectra of different Ag-AuNCs	132
Figure 4: TEM images of Ag-AuNCs of different molar ratios	134
Figure 5: Fluorescence based growth curves of the bacteria treated with Ag-AuNCs	135
Figure 6: Fluorescence based growth curves of the bacteria treated with AgNCs and AuNPs	136
Figure S1: UV-Vis and fluorescence-based growth curved for <i>E. coli</i> treated with AgNCs	150
Figure S2: TEM, UV-Vis spectra and size distribution of AgNCs and Ag nanoplates	151
Figure S3: TEM, UV-Vis spectra and size distribution of Ag nanoplates of different sizes	152
Figure S4: TEM, UV-Vis spectra and size distribution of AuNPs of different shapes	152
Figure S5: Fluorescence based growth curves of bacteria treated with AgNCs and AgNplates	153
Figure S6: Fluorescence based growth curves of <i>E. coli</i> treated with AuNPs	154

List of Tables

Chapter II

Table 1: Different formulations of injectable hydrogels based on P(OEGA-AA-NIPAM)	45
Table 2: Experimental details for cytotoxicity studies	52
Table S1: Hydrodynamic and zeta potential of Gel 8 and Gel 900	65

Chapter III

Table S1: Hydrodynamic diameter and zeta potential of PDA-coated AgNPs	98
Table S2: Hydrodynamic diameter and zeta potential of surface modified AgNCs	109
Table S3: Hydrodynamic diameter and zeta potential of surface modified AgNplates	110
Table S4: Hydrodynamic diameter and zeta potential of PVP-AgNPs at different time points	116
Table S5: Hydrodynamic diameter and zeta potential of PEI-AgNPs at different time points	117
Table S6: Hydrodynamic diameter and zeta potential of PEG-AgNPs at different time points	118

Chapter IV

Table 1: Ag-AuNCs of different molar ratios	127
Table 2: Summary of characterization of Ag-AuNCs of different molar ratios	134
Table S1: Summary of characterization of Ag and AuNSs	153

List of Published Articles

Chapter III: Polydopamine Surface Coating Synergizes the Antimicrobial Activity of Silver Nanoparticles, Niyonshuti, I.I.;† Krishnamurthi, V.R.;† Okyere, D.; Song, L.; Benamara, M.; Tong, X.; Wang, Y.;* Chen, J.* *ACS Appl. Mater. Interfaces* **2020**, 12, 40067-40077. (†equal contribution)

Chapter I: Introduction

1.1. Polyethylene glycol-based injectable hydrogels for wound healing applications

Polyethylene glycol (PEG)-based hydrogels

Hydrogels are three-dimensional networks of polymers that can absorb and retain a significant amount of water in their structures. The water retention property of hydrogels is given by the hydrophilic functional groups attached to the backbone of their polymeric structure.¹ The chemically or physically cross-linked networks in the hydrogels help to prevent them from dissolving in water. Over the past few decades, hydrogels have raised a lot of interest to many scientists because of their hydrophilicity, biocompatibility, and flexibility.² The hydrogels' resemblance to biological tissues gives many opportunities for their applications in biomedicine. The applications of hydrogels include but are not limited to drug delivery systems and tissue engineering.³⁻⁶ These biomaterials' lack of toxicity and biodegradability have rendered them useful as carriers for many drugs in the body.^{2,6} There are different kinds of hydrogel either from synthetic polymers or derived from natural polymers. The choice of polymers used to prepare hydrogels depends on the hydrogel's intended application. Hydrogels from natural polymers have high biocompatibility and biodegradability which are desired for biomedical applications; however, their purification techniques can be tedious which leads differences in formulations and modification from one batch to another. Moreover, hydrogels from natural polymers are hard to chemically functionalize.^{5,7} Unlike natural polymers, synthetic polymers present an advantage to tune degradation, mechanical, physical and chemical properties of hydrogels to match their biological site of application.⁸ Hydrogels from synthetic polymers such as poly(vinyl alcohol), poly (N,N isopropylacrylamide) (PNIPAM)) and Poly-ethylene glycol (PEG) have been studied extensively for their applications as drug delivery systems.⁹⁻¹⁴ PEG-based hydrogels, for instance,

are one of the common hydrogels that are being used in drug delivery because of their excellent biocompatibility and flexible physical properties; its biological functionality is preserved by the backbone of the polymeric network.^{7, 10} PEG-based hydrogels have contributed to some great clinical results when they are properly designed; they can help promote cellular functions such as proliferation and differentiation.^{9, 15} The highly usable PEG hydrogels are given by PEG's low toxicity, immunogenicity, antifouling properties which provide the hydrophilic nature, electrically neutrality, and hydrogen-bond acceptor/donor capabilities.^{16, 17} The antifouling nature of PEG-based hydrogels rendered them relevant in wound healing applications because of resistance to proteins.¹⁸⁻²¹ PEG by itself is non-reactive, so the end-functionalization such as adding acrylate is usually required before PEG can be used to make hydrogels (**Figure 1**).²² Different methods to modify PEG hydrogel and functionalizing them with small molecules or co-polymerizing with other macromolecules/polymers have been studied.^{23, 24} PEG provides enhanced biocompatibility of the copolymers it is part of.^{25, 26} In addition, copolymerization of PEG helps to easily incorporate other functional moieties in the hydrogels.^{9, 27} The criteria to design PEG-based hydrogel depend on their applications. In controlled release applications, designing the hydrogel should be done to target two main jobs, one being to achieve drug availability and to preserve therapeutics' molecular bioactivity.⁹ There are three commonly used mechanisms for loading of drugs from PEG hydrogels. The loading can be done through entrapment where the drugs are dispersed in the hydrogel by incubating them or in-situ encapsulation during network crosslinking. A tether can also be used where the drug is modified with a cross-linkable linker that can be degraded by proper enzymes at the release site. Lastly, the drugs can be pre-loaded in the micro/nanoparticles that then get entrapped into the hydrogel.^{9, 28} Among the loading mechanisms, the former ensures the stability of the drug during release as there is no interactions that happens between drug and

hydrogel to affect its stability. PEG-hydrogels can be designed for diffusion-controlled, swelling-controlled, and chemically controlled delivery of drugs. To ensure bioavailability of released therapeutics especially small molecules and proteins, PEG can be copolymerize with stimuli (pH, temperature, light) responsive polymer to release the drug under proper stimuli when the hydrogel is in swollen state, this way the hydrophilicity of PEG hydrogel is not compromised while the protein/drug is protected at the same time.^{9, 29} A degradable linker can also be added to covalently bind the drug to the hydrogel where the drug is released once the linker is enzymically or hydrolytically degraded. It is important to ensure the stability of the drug/proteins released from PEG-based hydrogel during the entire release by tuning monomers, crosslinker and initiators concentration ratios during the design to avoid the immunogenicity that can be caused by denatured therapeutics *in vivo*.

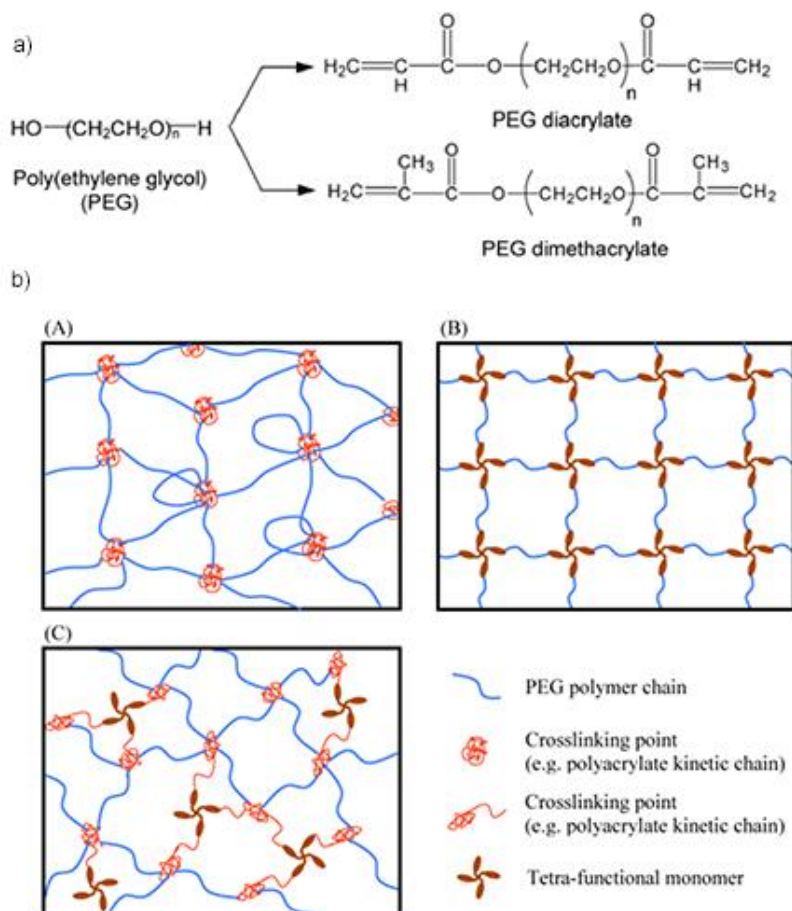


Figure 1: a) Chemical structures of PEG and its derivatives that polymerize to form hydrogel networks useful for biomaterial applications.⁹ and b) Schematic structures of PEG hydrogels formed via: (A) chain-growth, (B) step-growth, and (C) mixed-mode step and chain growth polymerization. (Components do not scale to actual size). Reproduced with permission from reference 9.

Injectable hydrogels

Injectable hydrogels have found a lot of interest in the past decade compared to other delivery systems such as coatings and conventional hydrogels.³⁰ Delivery coatings are known to have excellent delivery of therapeutics, but they bring some challenges such as poor bioavailability, requiring a large amount of loading, severe side effects, development of several drug resistance, and non-specificity of targeted delivery.^{30,31} Injectable hydrogels provide the same benefits as delivery coatings with minimal invasiveness, more precise, implantation and site-

specific delivery to irregularly shaped tissues.³² The injectable hydrogels are made through either physical or chemical crosslinking of monomers. The physical crosslinking methods are non-covalent interactions such as ionic crosslinking, hydrogen bonding, hydrophobic interactions, or host-guest chemistry (**Figure 2A**) are easy and reversible, but the resultant hydrogels' stability is not guaranteed due to easy dissociation of hydrogen bonds, for instance, between polymer chains during hydration.³² On the other hand, chemical crosslinking methods provide stable and tunable properties of the resultant injectable hydrogel from covalent and irreversible interactions. The crosslinking can be achieved by adding a small crosslinking molecule such as Schiff base³³⁻³⁵, Michael addition reaction³⁶, click chemistry³⁷ or enzyme-mediated crosslinking method (**Figure 2B**).³⁸⁻⁴⁰

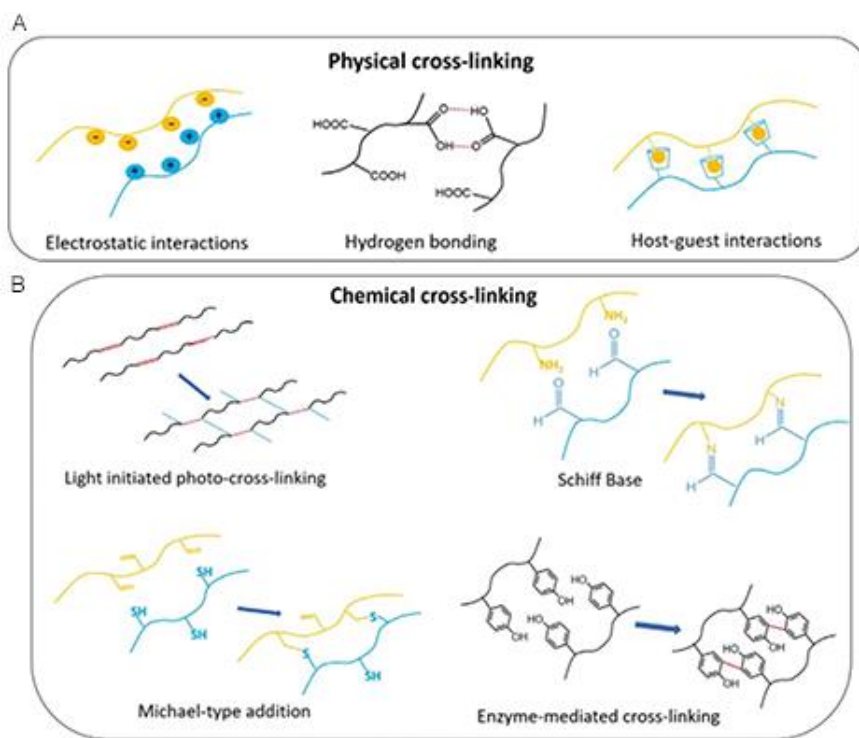


Figure 2. Schematic presentation of injectable hydrogels prepared by physically or chemically crosslinking polymers.³² Reproduced with permission from reference 32 and copyright from John Wiley and Sons.

Controlled delivery of Proteins from PEG-based injectable hydrogels

It has been found that proteins have various advantages over small molecule drugs that currently dominate the pharmaceutical market because proteins can achieve highly specific and complex functions, which is impractical for small molecule drugs.^{1,5} Therefore, therapeutic proteins like insulin are commonly used to treat different diseases. Despite their great usage, protein delivery systems have faced many issues in the past decades since common delivery systems do not guarantee stability of protein upon delivery.⁷⁻¹⁰ For instance; proteins are at high risk of being degraded in the gut when delivered through the oral route. Other current routes of delivery of therapeutic proteins, mainly enteral and parenteral administration, have shown different challenges despite their convenience and cost-effectiveness. The enteral administration is the most used method to deliver proteins because of its convenience, safety, and cost-effectiveness, but during the delivery protein comes in contact with low pH in the stomach and this can easily degrade the protein and ruin its activity.³ Another issue with this route is the size and hydrophilicity of protein that limit their absorption into biological membranes, for the protein passes through the intestinal wall and travels to the liver before being transported via the bloodstream (first-pass effect) to its target site.^{3,4} Therefore, degradation and low bioavailability of delivered protein associated with this route make it ineffective. Parenteral routes, which involve injection or infusion of drugs using needles inserted in the body give a long-term therapeutic effect because the drug can stay and be absorbed slowly by tissues ensuring 100% bioavailability as the drug is direct to the bloodstream.⁴ The pitfalls of parenteral routes, however, are the associated immunogenicity and pain. The type of administration route of protein has a profound effect on its efficiency and speed. Therefore, there is still a great need for a better delivery system that is cost-efficient and

ensures stability of the proteins after delivery with no immunogenicity. Therefore, hydrogels have been long used as an alternative delivery vehicle for several proteins.

PEG-based hydrogels provide local and sustained release of loaded proteins to increase the therapeutic effect and prevent/reduce adverse effect to preserve the bioactivity of proteins. Delivery of proteins from the hydrogel system depends on swelling of the hydrogels and/or diffusion of loaded proteins and chemistry between hydrogel-proteins (**Figure 3**). The release rate can be regulated by controlling the rate of swelling or diffusion or both. Chemical interactions between hydrogel and proteins can also help to have control over the release rate. Diffusion-controlled release is mainly for porous hydrogels that act as a reservoir or matrix for drug to be encapsulated or homogeneously dispersed in the gel following Fickian diffusion theory.^{9, 41, 42} Swelling-controlled release follows zero-order model and the rate is mainly controlled by the ability of hydrogel to swell and its thickness.^{41, 43} Chemically-controlled release is dependent on the cleavage of polymer chain to release the protein.^{9, 41, 42} The hydrogel network properties, the size of drug/protein released and degradation rate of the hydrogels explain the release kinetics of the drug.⁴⁴⁻⁴⁶ In addition, some studies show that the delivery can be controlled by protein structure.⁴⁶⁻⁴⁸ Electrostatic interactions between hydrogel and proteins hold the protein in the hydrogel network preventing burst release on delivery site.^{47, 49, 50} Therefore, hydrogels can ensure stability of these bioactive molecules by encapsulating them in their matrix. Henceforth, hydrogels address the issue of proteins that suffer from substandard physical and chemical instability during the current delivery methods because of chemical and proteolytic degradation, unfolding and aggregation. Therefore, to minimize self-aggregation of the protein, researchers can enhance efficiency of the delivery by using hydrogels to make a complex of protein and polymer that will enable evaluation of protein's activity.¹⁻⁵ Polymeric micelles of hydrogels provide a good chemical

flexibility to customize their molecular architecture and to bestow on responsiveness to different and multiple stimuli such as temperature and pH.⁶ They also have the capacity to host, solubilize and stabilize the poorly water-soluble proteins.^{6, 8}

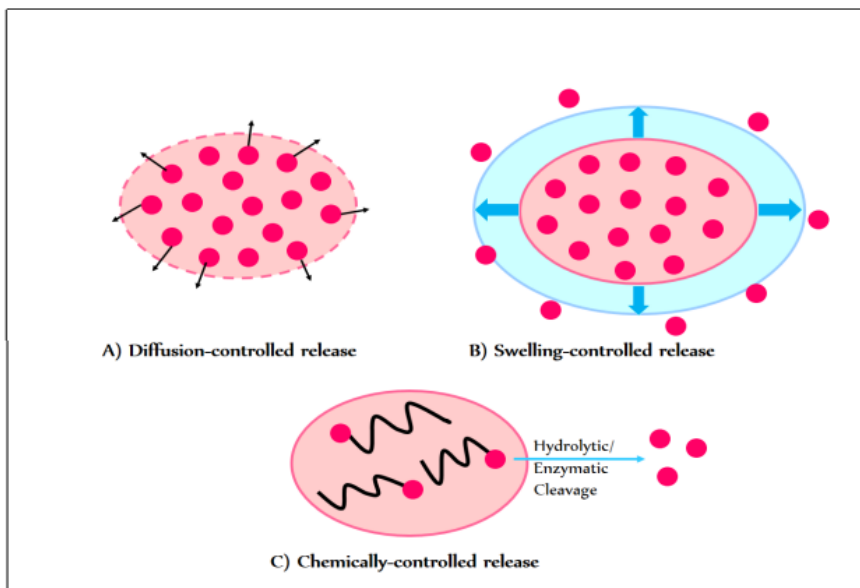


Figure 3. Different release mechanisms of proteins from hydrogels; A) diffusion-controlled release, B) swelling-controlled release, and C) chemically controlled release.⁷ Adapted with permission from reference 7.

Fibroblast growth factors in wound healing

Fibroblast growth factors (FGFs) are involved in fibroblast proliferation, embryonic development, homeostasis, and different diseases developments like cancer.⁵¹⁻⁵³ FGFs' multifunction have allowed them to be used in wound healing applications and this has given them advantages for use in tissue regeneration applications and during implants as repair factors.^{53, 54} During wound healing, different types of FGFs including FGF1, FGF2, FGF7, FGF10, and FGF22 are expressed at the wound site.⁵³ FGFs are mainly involved in angiogenesis, and they can be used to prevent fibrosis in myocardial infarction.^{52, 55} Different studies showed the importance of FGFs in wound healing of different type of wounds, namely, diabetics ulcers, burns and chronic wounds.

These studies show that FGF2 shorten the healing time and thickness of the wound.⁵⁶ The FGFs proteins are released at the wound site by proliferative cells to help immigration of extracellular matrix from neighboring blood vessels into the wound (**Figure 5**).^{57, 58} The injectable hydrogels have been used for delivery of FGFs because hydration and moisture provided by the hydrogels can fasten the epithelialization process during proliferation phase of wound healing.^{58, 59} Monomers like poly acrylic acid (PAA) can mimic heparin which possess antithrombin-activating properties.⁶⁰ Therefore, hydrogel based on PAA may promote anti-inflammatory processes when used for controlled release of FGFs at the wound site.⁶¹

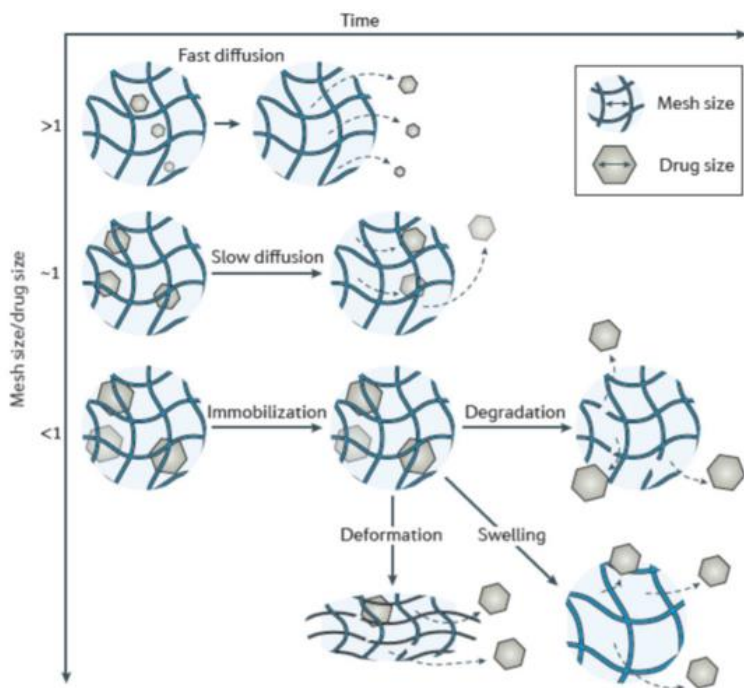


Figure 4: Designing hydrogel for controlled delivery of drugs by controlling mesh size.⁶² Adapted with permission from reference 62 and copyright from Springer nature.

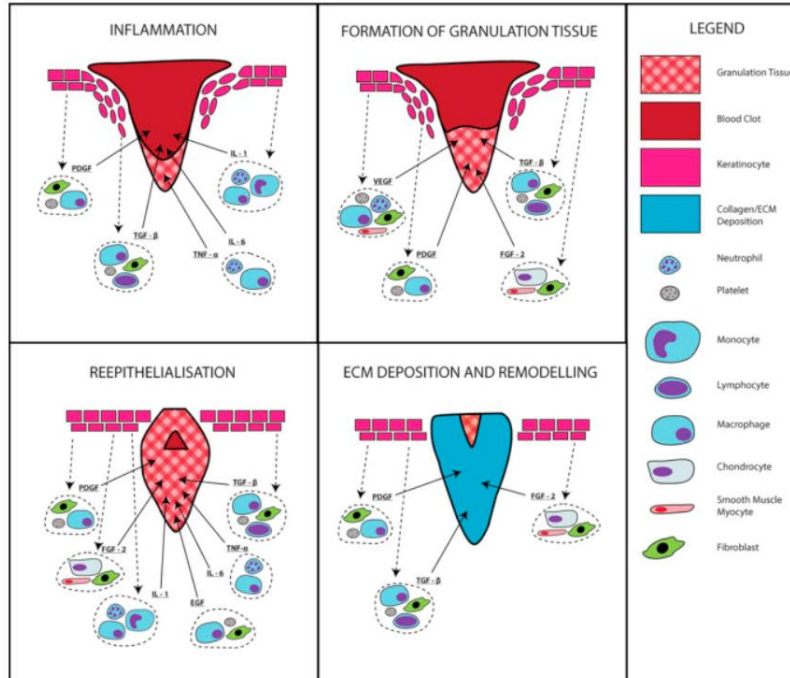


Figure 5: FGFs in wound healing process.⁶³ Adapted with permission from reference 63 and copyright from Elsevier.

Current challenges of using hydrogels

Stimuli or environmental responsive hydrogels have found interests as delivery system because they account for a typical environmental condition occurring at the site of disease. The common stimuli responsive hydrogel is poly (N-isopropylacrylamide) (PNIPAM) with critical solution temperature (LCST) near 32 °C. Because the PNIPAM's temperature response is near the human body temperature, PNIPAM based hydrogels have been used in biomedical applications.⁶⁴ PNIPAM hydrogels expels water out of its polymer networks at higher temperature than its LCST as results of weakened hydrogen bonds. At the same time the interactions between hydrophobic groups (-CH(CH₃)₂) become stronger.^{27, 64, 65,66} Different studies have modified PNIPAM hydrogel to control its LCST, for instance by copolymerizing it with other monomers like PEG.⁶⁷ Some of the limitations of synthetic hydrogels are non-biodegradable properties of some synthetic polymers. The problem has been addressed by incorporating biodegradable moieties in the

hydrogel such as Polyethylene glycol – poly(lactic-*co*-glycolic acid) – polyethylene glycol (PEG-PLGA-PEG) or using polymers that have hydrolysable moieties.^{7, 13, 68} A burst and fast release of drug can be observed for small drugs from large pores of the hydrogels (**Figure 4**). The fast release can be controlled by physically or covalently linking the drug to the hydrogel prior to gelation or making copolymers by covalent linking to overcome the drug dissolution from hydrogels.⁶⁸ In addition, the hydrogels or scaffolds can present a risk of infection when applied on wound through surgical implantation, but injectable hydrogels solve the problem by minimizing the risk of infections and inadequate adaptation to the wound site with minimal invasiveness.⁶⁹ Also, hydrogels carriers that are based on copolymers of small molecules like acrylic acid and methyl acrylate were developed to solve the problem of small molecular weights drug/therapeutics that are also hydrophobic.⁷⁰ Despite their great application, hydrogels have not been explored in clinical setting as much as it should. While their material properties important to make stable 3D structure of proteins can be easily controlled through the chemistry of hydrogel formation, development of hydrolytically degradable and biocompatible hydrogels can allow for sustained material degradation and controlled release of therapeutic proteins.

1.2. Silver nanoparticles for antimicrobial applications

General biomedical applications of silver and silver nanoparticles

Silver (Ag) is a lustrous transitional metal with the highest thermal conductivity, electrical conductivity, and reflectivity of any metals. The Ag's properties have raised so much interest in nanotechnology.⁷¹ Ag is biologically active when soluble in aqueous medium in its monoatomic ionic state (Ag⁺).^{72, 73} Therefore, Ag has found many applications in biomedicine to date. The antimicrobial properties of Ag was recognized early in 1500 BC where it was used in needles for acupuncture, making vessels for preservation of liquids and prevention of infections.^{3,74} Ag is

known for its anti-inflammatory properties from the ancient time where it has been used to treat burn wounds.⁷⁴ Ag found more and more applications over time and mostly in wound treatment, fighting pathogens, water purification system and over the counter drug.⁷³ Then later silver compounds such as silver nitrate (AgNO_3) started being used to treat infections.^{75,3} In addition, different types of colloidal Ag, as well as other forms of Ag have found applications as antimicrobial agents to treat different bacteria.⁷⁶ Moreover, Ag has a relatively high reduction potential, which makes its nanomaterials easy to synthesize using wet chemistry. Different methods to synthesize silver nanoparticles (AgNPs) were developed including green chemistry and polyol methods. AgNPs have sizes ranging from 1 to 100 nm and their color depends upon the shape of the particles.^{71,77} These nanoparticles have a strong scattering and absorption properties of electrons as result of oscillation created when electrons interact with silver metal surface upon excitation by the light at a particular wavelength; ^{1,77,78} this phenomenon is called localized surface plasmon resonance (LSPR) and it is responsible for the brilliant colors of colloidal Ag. LSPR changes with nanoparticles shape and size. Like other noble metal nanomaterials AgNPs have an increased chemical activity due to their large surface area to volume ratio,⁷⁹ which allows their biomedical applications.

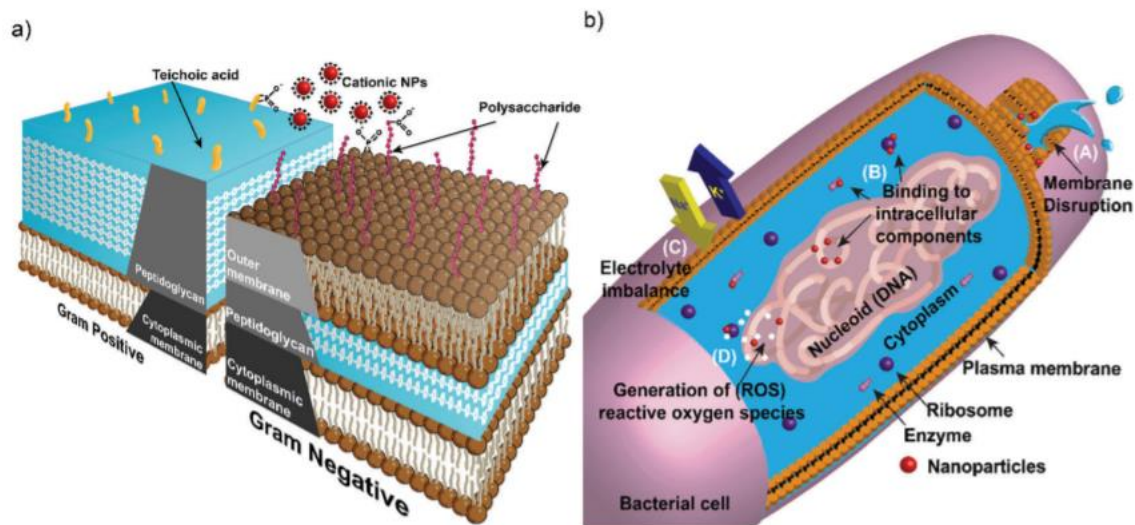


Figure 6: a) cell wall structures of Gram-positive and Gram-negative bacteria. b) antimicrobial mechanisms of NPs. A) disruption of cell membrane resulting in cytoplasmic leakage. B) binding and disruption of intracellular components. C) disrupting electron transport causing electrolyte imbalance. D) generation of reactive oxygen species (ROS).¹⁰¹ Adapted with permission from reference 101 and copyright from Royal Society of Chemistry.

Antimicrobial applications of silver nanoparticles

AgNPs have been known to have antimicrobial effect through their interactions with proteins and/or deoxyribonucleic acid inside the bacteria.^{1,80-83,84} The antimicrobial effect of these nanoparticles opens a new venue to fighting against drug resistance of microbes, which has been a severe concern to public health.^{79, 85} Microbes are less likely to generate resistance against silver, as they do against other antibiotics, because Ag attacks a broad range of targets in the microorganisms (bacteria or virus), which would take the organisms to develop a host of mutations simultaneously to protect themselves.⁷⁹ Researchers have studied the source of AgNPs antimicrobial properties and mostly attributed its toxicity to the release of Ag⁺ ion upon oxidation of AgNPs,⁸⁶ which can lead to production of reactive oxygen species (ROS) that cascade and to cause oxidative stress in bacterial cell, which eventually lead to inhibition of important metabolic reactions then bacterial death. However, the physical nanoparticle-cell interactions were also found

to be the major mechanism that lead to bacteria death caused by disruption of cell membrane and leakage of cell content.^{87,88, 89} Therefore, both Ag⁺ ions and AgNPs contribute to the governing mechanisms of antimicrobial activity against bacteria.⁸⁸ The main mechanisms of antimicrobial activity of AgNPs are due to their large surface areas to volume ratio that help them to interact with bacterial cells.

Mechanisms guiding antimicrobial activity of silver nanoparticles

The antimicrobial performance of AgNPs is believed to happen in four mechanisms which can work either parallel or independently (**Figure 6b**). First, the nanoparticles adsorb on the surface of AgNPs via electrostatic interactions and the interactions can cause bacterial surface charge neutralization which then allow permeability of cell.⁹⁰⁻⁹² Secondly, the adhesion of AgNPs to the surface of bacteria can trigger membrane rigidity and disintegration of membrane's carbohydrates, proteins and fatty acids.⁹²⁻⁹⁴ AgNPs then destroy the cell wall which lead to cell content leakage and inactivation of bacteria (**Figure 7B**). The third step is ROS generation which causes oxidative stress. AgNPs produce ROS (superoxide, hydrogen peroxide and hydroxyl radicals) which induces oxidative stress responsible for cell membrane damage then cell death.^{90, 95, 96,97} The ROS production depends on nanoparticles size, shape, surface area and surface chemistry.^{2,98} Some studies have suggested that size of AgNPs is the main factor guiding ROS generation where smaller NPs produced more ROS even at the lower concentration than bigger AgNPs.⁹⁹ Other studies showed that ROS generation was dependent on the concentration of AgNPs.³⁵ Oftentimes ROS generation has been used as a great marker of AgNPs toxicity as it leads to lipid, protein and DNA damages (**Figure 9**), leakage of cellular biomolecules and cell apoptosis as a result. The small nanoparticles can also enter the inside of bacterial cell to destroy the bacterial structure, affecting the cell's signal transduction pathways. Size, surface chemistry and shape have

important effect on antimicrobial performance of AgNPs and determine the mechanism at which the nanoparticles go through.^{84, 88}

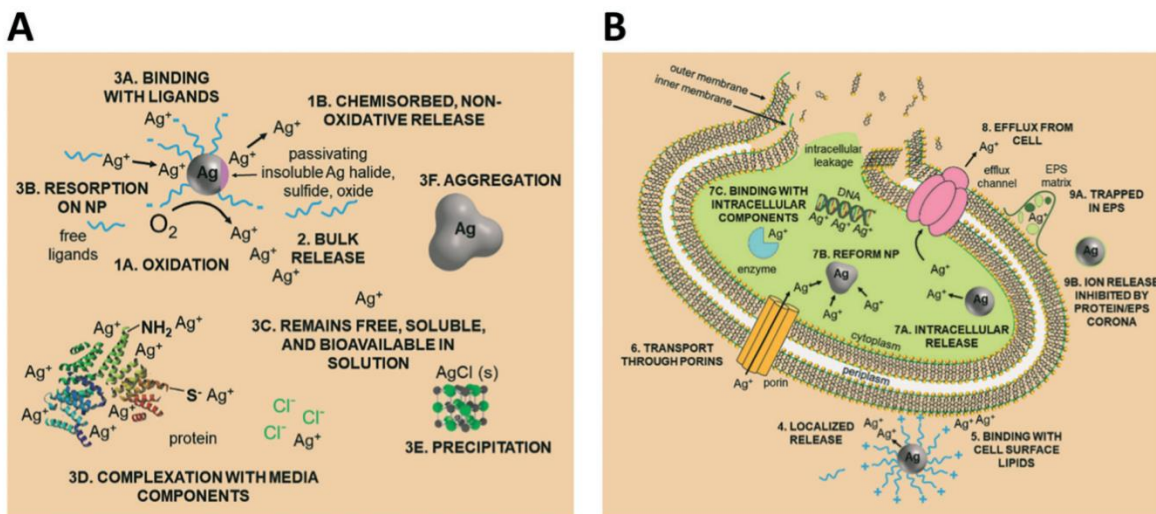


Figure 7: Antimicrobial mechanisms of AgNPs. (A) State of Ag in the media outside of the bacterial cell. (B) Interaction of Ag with the bacterial cell. Note: figure is not to scale as the particle is enlarged to demonstrate effect.⁸⁸ Reprinted with permission from reference 86 and copyright from Royal Society of Chemistry.

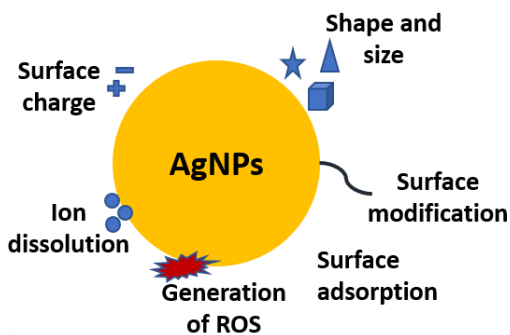


Figure 8: Properties of Silver nanoparticles (AgNPs) affecting their antimicrobial activity.

Effect of size on silver nanoparticles' antimicrobial performance

The bactericidal activity of AgNPs over a broad spectrum of bacteria strains was found to be dependent on size of the nanoparticles as the size dictates their distribution *in vivo* and interactions with the microorganisms, thus toxicity. It was found that smaller size of AgNPs

interact more with bacteria,⁷⁹ because size influences on Ag⁺ ion uptake and contact with bacterial cell which determines the extent of cell damage. Agnihotri et al., evidenced enhancement of bactericidal efficacy against *Escherichia coli* MTCC 443 and *Staphylococcus aureus* NCIM 5201 as the size of the AgNPs decreased to 10 nm,¹⁰⁰ and realized a further enhancement of bactericidal when the size was down to 5 nm. Higher surface area of small nanoparticles compared to big ones is associated with more surface reactivity that can lead to more toxicity. Another study done on different sizes of AgNPs by Huk et al. lead to a combination of size, concentration and type of damages on gene mutation effect of these AgNPs, it was concluded that evaluation of AgNPs should be evaluated based on the number of AgNPs and surface area of the nanoparticles.¹⁰¹ Size of AgNPs also determines passive uptake and intracellular release of Ag⁺ ion. It was found that there is a synergetic mechanism between contact killing and Ag⁺ ion release for the existing antimicrobial activity of AgNPs.^{100,101-105} In some cases, smaller size of the AgNPs does not improve their antimicrobial activity when the nanoparticles are used in powder form because the powder form increase particle-particle aggregation, that leads to reduction in the effective surface area available for antimicrobial activity.¹⁰³ The antibacterial effect of AgNPs of different sizes would differ due to changes in their interactions with pathogenic cells and release of Ag⁺ ions.¹⁰⁶

Effect of shape on AgNPs antimicrobial performance

The shape of AgNPs has a big impact on their toxicity by influencing the contact with the cell and damage through physical mechanism. The shape also influences ion release either localized or intracellularly.⁸⁴ For instance, Alshareef et al.⁷⁸ found that truncated octahedral AgNPs (AgNOct) were more active compared to the spherical AgNPs (AgNS) because of their higher surface area. Moreover, AgNOct exhibit (111) intensities lattice planes compared to AgNS.¹⁰⁷ AgNPs reactivity increases with more surface density facets, and more surface energies compared to spherical

AgNPs, hence better efficacy in antimicrobial activity.¹⁰⁸ In another study, Ag nanospheres (AgNSs), nanoplatelets (AgNTs), nanocubes (AgNDs) and nanorods prepared with the same ligand showed a correlation between surface area to dissolution rate of Ag⁺ ions in the media.¹⁰⁹ Ag nanoplatelets showed the highest antimicrobial potency among tested shapes as platelet's exposed facets lead to direct interactions with bacteria surface then more surface binding, high dissolution rate as well as specific surface area.¹⁰⁹⁻¹¹³ The nanoparticles with high specific surface area exhibited fast dissolution rate, which then led to more oxidation of AgNPs to Ag⁺ ions as the amount of Ag ions was found to have been released in the order of Ag NSs > Ag NDs > Ag NTs.¹⁰⁹ The antimicrobial activity of the Ag NPs was mainly dependent on their morphology, which was closely associated with the total surface area and the amount of Ag ions (dissolution rate) that were released.^{109,114, 110}

Effect of surface chemistry on antimicrobial properties of silver nanoparticles

Surface chemistry is more important than morphology and size of the nanoparticles in catalytic reaction and antimicrobial effects of different nanoparticles.^{115,102} Surface chemistry of AgNPs is an essential parameter for their antimicrobial properties because it has an impact on their chemical and dispersion stability which affect Ag⁺ ion release.^{110, 116} Surface chemistry of AgNPs is influenced by the surface charge that depends on surface ligand, and surface charge has shown a big effect on the antimicrobial behaviors of the nanoparticles as it dictates NP-cell interactions. Electrostatic barrier between negative cell wall and negatively charged NPs limits their interactions, thus reducing the toxicity.¹⁰⁵ AgNPs coated with positively charged ligands such as polyethyleneimine (PEI) show better toxicity against various strains of bacteria compared to negative or neutral ligands.^{105, 117-119} It was previously demonstrated that the positively charged PEI-AgNPs exhibit a larger reorganization of H-NS proteins and higher changing rates of the

molecular and clustering parameters compared to negatively charged PVP-AgNPs at the same concentration. Tang et al. found that surface charge-dependent toxicity of AgNPs where BPEI-AgNPs presented the highest toxicity against *bacillus species* as result of the electrostatic interactions between oppositely charged nanoparticles and bacterial cell wall.^{81, 120, 121} Furthermore, negatively charged AgNPs such as citrate-AgNPs would present less toxicity from an electrostatic barrier that hinders interaction of bacteria and NPs.^{112, 122, 123}

Moreover, the type of capping agent has a big effect on toxicity of AgNPs and depending on the nature of the stabilizing agent, electrostatic repulsion or steric hindrance prevent nanoparticles from agglomeration. Steric stabilization is given by uncharged polymers like (poly(vinylpyrrolidone) (PVP) while electrostatic stabilization is given by charged coating such as gum Arabic (GA).¹²⁴ Different coatings (neutral PVP and Tween 80, positive PLL and CTAB, negatively charged coatings AOT and CIT) were used on the AgNPs to find out the how the surface of these nanoparticles impact the interaction between bacteria and NPs. The effect of stabilizing agent was also observed on 50 nm AgNPs where CTAB and Tween 80 show the lowest antimicrobial activity.

The toxicity of AgNPs can be controlled by the choice of coating used on these nanoparticles. Various researchers studied the effect of surface modification on antimicrobial performance *in vitro* and *in vivo*.^{119, 125, 126} Das et al. noticed that polyethylene glycol (PEG) and bovin serum albumin (BSA) exhibit different effects on AgNPs toxicity where PEG-functionalized AgNPs showed much reduced effect on bacteria compared to BSA-AgNPs.¹¹⁹ In addition, generation of ROS such as superoxide ions were significantly reduced after the NPs were coated with PEG and BSA suggesting that functionalizing the surface of AgNPs lead to minimum toxicity as the coating protects AgNPs from leaching Ag⁺ ions.¹¹⁹ Some of the coatings like CTAB already

have antimicrobial properties so when on AgNPs, there is synergetic or additive antimicrobial effects. They, furthermore, studied the synergistic effect of AgNPs using fractional inhibitory concentration (FICs) wherein the combination of PVP-AgNPs with curcumin was highly synergistic and both *E. coli* and *B. Subtilis* with FIC induces of 0.375 and 0.5, respectively. The antimicrobial effects were based on Ag⁺ ions that was released and intracellular ROS generated by curcumin-AgNPs.⁹⁷ The study proved the coatings are not the main cause of toxicity on the AgNPs as the minimum bactericidal concentration of the coatings were order of magnitude higher than that of coated AgNPs.²² Polydopamine layer increased the adhesion of AgNPs on the catheters by increasing the hydrophilicity of the usually hydrophilic surface of the catheters and AgNP-coated catheters showed an antimicrobial performance that was dependent on AgNPs density.¹²⁷ It is very important to study synergic versus additive effect of coating and AgNPs when using coating have an already know antimicrobial activity. In addition, small capping agent like citrate bind to the surface of AgNP through its oxygen with a weak binding affinity and so this facilitates the adsorption of the AgNPs as it binds with surrounding oxygen. The citrate's short carbon chain and weak binding enables easier access to the silver core by surrounding oxygen compared to the thiol group terminated ligands.¹⁴ These results and others in the literature show reliance of AgNPs antimicrobial activities on the chemisorbed Ag⁺ formed from responsiveness to environmental oxygen, that also depends on surface ligands.^{14,128,129, 130}

More recently it is becoming clearer that the antimicrobial effects of AgNPs is more related to released Ag⁺ ions, which depended on the type of bacteria, time exposed to the bacteria, size and surface coatings. Small nanoparticles that are more stable in water (more dissolution of Ag⁺ ions) tend to show higher antimicrobial activity than bigger AgNPs, less soluble in water have lower activity. The type of bacteria strain is also a factor of antimicrobial effect of AgNPs. *E. coli*

(gram negative), for instance, was found to be more prone to growth inhibition than *S.aureus* (gram positive) because of the nature of cell wall (**Figure 6A**).^{102, 117, 131-133} Therefore, when designing the AgNPs as antimicrobial agents surface chemistry is very important factor to consider as it determines its behavior rather than specific properties of the NPs determined by their size and shape.

Overview of this research

This research has two independent projects that is reported in 5 chapters. The first project aims to fabricate novel biocompatible PEG-based anionic hydrogels for controlled release of positively charged proteins like acidic human growth factors (hFGF1) for wound healing applications. Here we report preparation of a new PEG-based injectable anionic hydrogel system using a simple and robust free-radical polymerization reaction. The application of the hydrogel in delivery of proteins for wound healing applications. The second project aims to optimize properties of silver nanoparticles and silver/gold alloy nanostructures for better understanding of the mechanisms involved in their antimicrobial performance at the molecular level. Synthesis, surface modifications, stability, and antimicrobial studies of various silver nanoparticles against a gram-negative bacterium, *E. coli* are reported here.

The work is organized according to previously published articles or work in preparation for publication. Chapter 2 presents synthesis of a new biocompatible injectable hydrogel, P(OEGA-AA-NIPAM) with capability of controlled release of positively charged proteins, hFGF1 and its mutation. This research seeks to explore feasibility of using the new anionic hydrogel to release of different proteins where changing parameters such as mole ratios between co-monomers in polymers and crosslinking can help to optimize the release profile of the proteins. The stability of released protein is also studied *in vitro* and *in vivo* in wound healing. Furthermore, we determine

physical properties like swelling behaviors which is very important for the ability of hydrogels to encapsulate the protein. For evaluation of degradability of the hydrogel, we performed hydrolytic degradation in simulated body fluid. This research addresses the problem of poor stability of proteins and contribute to sustained release of active proteins for wound healing applications.

Chapters 3 and 4 investigate the effects surface chemistry, morphology, and compositions properties of AgNPs on their antimicrobial properties. Chapter 3 extrapolates surface chemistry effect on AgNPs focusing on surface charge and effect of PDA coating. The antimicrobial activity can be controlled to render high interactions between bacteria and AgNPs, enhanced stability of AgNPs to prevent aggregation and coordination of Ag and surface coating to optimize their antimicrobial properties. It is also here we confirm that the surface charge of AgNPs should be as positive as possible to increase the surface interaction with surface of gram-negative bacterial like *E. coli*. Chapter 4 elaborates on the effects of morphology and composition of Ag/AuNCs on their antimicrobial effects. Lastly, chapter 5 is a conclusion of the two parts of the dissertation and elaborates future work.

References

1. Ahmed, E. M., Hydrogel: Preparation, characterization, and applications: A review. *Journal of Advanced Research* **2015**, *6* (2), 105-121.
2. Thurmer, M. B.; Diehl, C. E.; Brum, F. J. B.; dos Santos, L. A., Preparation and Characterization of Hydrogels with Potential for Use as Biomaterials. *Materials Research-Ibero-American Journal of Materials* **2014**, *17*, 109-113.
3. Censi, R.; Di Martino, P.; Vermonden, T.; Hennink, W. E., Hydrogels for protein delivery in tissue engineering. *Journal of Controlled Release* **2012**, *161* (2), 680-692.
4. Vermonden, T.; Censi, R.; Hennink, W. E., Hydrogels for Protein Delivery. *Chemical Reviews* **2012**, *112* (5), 2853-2888.
5. Narayanaswamy, R.; Torchilin, V. P., Hydrogels and Their Applications in Targeted Drug Delivery. *Molecules* **2019**, *24* (3), 18.

6. Onaciu, A.; Munteanu, R. A.; Moldovan, A. I.; Moldovan, C. S.; Berindan-Neagoe, I., Hydrogels Based Drug Delivery Synthesis, Characterization and Administration. *Pharmaceutics* **2019**, *11* (9), 24.
7. Ghasemiyeh, P.; Mohammadi-Samani, S., Hydrogels as Drug Delivery Systems; Pros and Cons. *Trends in Pharmaceutical Sciences* **2019**, *5* (1), 7-24.
8. Madduma-Bandarage, U. S. K.; Madihally, S. V., Synthetic hydrogels: Synthesis, novel trends, and applications. *Journal of Applied Polymer Science* **2021**, *138* (19), 23.
9. Lin, C. C.; Anseth, K. S., PEG hydrogels for the controlled release of biomolecules in regenerative medicine. *Pharm Res* **2009**, *26* (3), 631-43.
10. Almany, L.; Seliktar, D., Biosynthetic hydrogel scaffolds made from fibrinogen and polyethylene glycol for 3D cell cultures. *Biomaterials* **2005**, *26* (15), 2467-2477.
11. Bashir, S.; Hina, M.; Iqbal, J.; Rajpar, A. H.; Mujtaba, M. A.; Alghamdi, N. A.; Wageh, S.; Ramesh, K.; Ramesh, S., Fundamental Concepts of Hydrogels: Synthesis, Properties, and Their Applications. *Polymers* **2020**, *12* (11), 60.
12. Kopecek, J.; Yang, J. Y., Revie - Hydrogels as smart biomaterials. *Polymer International* **2007**, *56* (9), 1078-1098.
13. Li, Z.; Ning, W.; Wang, J.; Choi, A.; Lee, P. Y.; Tyagi, P.; Huang, L., Controlled gene delivery system based on thermosensitive biodegradable hydrogel. *Pharm Res* **2003**, *20* (6), 884-8.
14. Wang, D. N.; Yang, X. W.; Liu, Q.; Yu, L.; Ding, J. D., Enzymatically cross-linked hydrogels based on a linear poly(ethylene glycol) analogue for controlled protein release and 3D cell culture. *Journal of Materials Chemistry B* **2018**, *6* (38), 6067-6079.
15. Alexander, A.; Ajazuddin; Khan, J.; Saraf, S., Poly(ethylene glycol)-poly(lactic-co-glycolic acid) based thermosensitive injectable hydrogels for biomedical applications. *Journal of Controlled Release* **2013**, *172* (3), 715-729.
16. Harris, J. M., *Poly(ethylene glycol) chemistry : biotechnical and biomedical applications*. Plenum Press: New York; London, 1992.
17. Chen, S.; Li, L.; Zhao, C.; Zheng, J., Surface hydration: Principles and applications toward low-fouling/nonfouling biomaterials. *Polymer* **2010**, *51* (23), 5283-5293.
18. Gong, Z.; Zhang, G.; Zeng, X.; Li, J.; Li, G.; Huang, W.; Sun, R.; Wong, C., High-Strength, Tough, Fatigue Resistant, and Self-Healing Hydrogel Based on Dual Physically Cross-Linked Network. *ACS Applied Materials & Interfaces* **2016**, *8* (36), 24030-24037.
19. Zhu, D.; Ye, Q.; Lu, X.; Lu, Q., Self-healing polymers with PEG oligomer side chains based on multiple H-bonding and adhesion properties. *Polymer Chemistry* **2015**, *6* (28), 5086-5092.

20. Ito, T.; Yoshida, C.; Murakami, Y., Design of novel sheet-shaped chitosan hydrogel for wound healing: A hybrid biomaterial consisting of both PEG-grafted chitosan and crosslinkable polymeric micelles acting as drug containers. *Materials Science and Engineering: C* **2013**, *33* (7), 3697-3703.
21. Moulay, S., Dopa/Catechol-Tethered Polymers: Bioadhesives and Biomimetic Adhesive Materials. *Polymer Reviews* **2014**, *54* (3), 436-513.
22. Zustiak, S. P.; Leach, J. B., Hydrolytically Degradable Poly(Ethylene Glycol) Hydrogel Scaffolds with Tunable Degradation and Mechanical Properties. *Biomacromolecules* **2010**, *11* (5), 1348-1357.
23. Atta, S.; Khaliq, S.; Islam, A.; Javeria, I.; Jamil, T.; Athar, M. M.; Shafiq, M. I.; Ghaffar, A., Injectable biopolymer based hydrogels for drug delivery applications. *International Journal of Biological Macromolecules* **2015**, *80*, 240-245.
24. Gorochovceva, N.; Makuška, R., Synthesis and study of water-soluble chitosan-O-poly(ethylene glycol) graft copolymers. *European Polymer Journal* **2004**, *40* (4), 685-691.
25. Won, C.-Y.; Chu, C.-C.; Lee, J. D., Novel biodegradable copolymers containing pendant amine functional groups based on aspartic acid and poly(ethylene glycol). *Polymer* **1998**, *39* (25), 6677-6681.
26. Pasut, G.; Caboi, F.; Schrepfer, R.; Tonon, G.; Schiavon, O.; Veronese, F. M., New active poly(ethylene glycol) derivative for amino coupling. *Reactive and Functional Polymers* **2007**, *67* (6), 529-539.
27. Wang, T.; Jones, J. D.; Niyonshuti, I. I.; Agrawal, S.; Gundampati, R. K.; Kumar, T. K. S.; Quinn, K. P.; Chen, J., Biocompatible, Injectable Anionic Hydrogels Based on Poly(Oligo Ethylene Glycol Monoacrylate-co-Acrylic Acid) for Protein Delivery. *Advanced Therapeutics* **2019**, *2* (9).
28. Fu, Y. P.; Ding, Y.; Zhang, L. T.; Zhang, Y. M.; Liu, J.; Yu, P., Poly ethylene glycol (PEG)-Related controllable and sustainable antidiabetic drug delivery systems. *European Journal of Medicinal Chemistry* **2021**, *217*, 21.
29. Peppas, N. A.; Keys, K. B.; Torres-Lugo, M.; Lowman, A. M., Poly(ethylene glycol)-containing hydrogels in drug delivery. *Journal of Controlled Release* **1999**, *62* (1-2), 81-87.
30. Bhujbal, S. S.; Darade, S. B.; Dharmadhikari, S. S., BIOMATERIAL BASED INJECTABLE HYDROGEL FOR CONTROLLED DRUG DELIVERY: A REVIEW. *International Journal of Pharmaceutical Sciences and Research* **2020**, *11* (3), 1007-1021.
31. Kumar, P.; Choonara, Y. E.; Modi, G.; Naidoo, D.; Pillay, V., Multifunctional Therapeutic Delivery Strategies for Effective Neuro-Regeneration Following Traumatic Spinal Cord Injury. *Current Pharmaceutical Design* **2015**, *21* (12), 1517-1528.

32. Rizzo, F.; Kehr, N. S., Recent Advances in Injectable Hydrogels for Controlled and Local Drug Delivery. *Advanced Healthcare Materials* **2021**, *10* (1), 2001341.
33. Davoodi, P.; Ng, W. C.; Yan, W. C.; Srinivasan, M. P.; Wang, C.-H., Double-Walled Microparticles-Embedded Self-Cross-Linked, Injectable, and Antibacterial Hydrogel for Controlled and Sustained Release of Chemotherapeutic Agents. *ACS Applied Materials & Interfaces* **2016**, *8* (35), 22785-22800.
34. Wu, X.; He, C.; Wu, Y.; Chen, X.; Cheng, J., Nanogel-Incorporated Physical and Chemical Hybrid Gels for Highly Effective Chemo-Protein Combination Therapy. *Advanced Functional Materials* **2015**, *25* (43), 6744-6755.
35. Ren, B.; Chen, X.; Du, S.; Ma, Y.; Chen, H.; Yuan, G.; Li, J.; Xiong, D.; Tan, H.; Ling, Z.; Chen, Y.; Hu, X.; Niu, X., Injectable polysaccharide hydrogel embedded with hydroxyapatite and calcium carbonate for drug delivery and bone tissue engineering. *Int J Biol Macromol* **2018**, *118* (Pt A), 1257-1266.
36. Shu, X. Z.; Ahmad, S.; Liu, Y.; Prestwich, G. D., Synthesis and evaluation of injectable, in situ crosslinkable synthetic extracellular matrices for tissue engineering. *J Biomed Mater Res A* **2006**, *79* (4), 902-12.
37. Abandansari, H. S.; Ghanian, M. H.; Varzideh, F.; Mahmoudi, E.; Rajabi, S.; Taheri, P.; Nabid, M. R.; Baharvand, H., In situ formation of interpenetrating polymer network using sequential thermal and click crosslinking for enhanced retention of transplanted cells. *Biomaterials* **2018**, *170*, 12-25.
38. Compaan, A. M.; Song, K.; Chai, W.; Huang, Y., Cross-Linkable Microgel Composite Matrix Bath for Embedded Bioprinting of Perfusable Tissue Constructs and Sculpting of Solid Objects. *ACS Applied Materials & Interfaces* **2020**, *12* (7), 7855-7868.
39. Wang, X.; Chen, S.; Wu, D.; Wu, Q.; Wei, Q.; He, B.; Lu, Q.; Wang, Q., Oxidoreductase-Initiated Radical Polymerizations to Design Hydrogels and Micro/Nanogels: Mechanism, Molding, and Applications. *Adv Mater* **2018**, *30* (17), e1705668.
40. Carthew, J.; Frith, J. E.; Forsythe, J. S.; Truong, V. X., Polyethylene glycol-gelatin hydrogels with tuneable stiffness prepared by horseradish peroxidase-activated tetrazine-norbornene ligation. *Journal of Materials Chemistry B* **2018**, *6* (9), 1394-1401.
41. Lin, C. C.; Metters, A. T., Hydrogels in controlled release formulations: network design and mathematical modeling. *Adv Drug Deliv Rev* **2006**, *58* (12-13), 1379-408.
42. Peppas, N. A.; Bures, P.; Leobandung, W.; Ichikawa, H., Hydrogels in pharmaceutical formulations. *Eur J Pharm Biopharm* **2000**, *50* (1), 27-46.

43. Siepmann, J.; Peppas, N. A., Modeling of drug release from delivery systems based on hydroxypropyl methylcellulose (HPMC). *Adv Drug Deliv Rev* **2001**, *48* (2-3), 139-57.
44. Bertz, A.; Wohl-Bruhn, S.; Mieth, S.; Tiersch, B.; Koetz, J.; Hust, M.; Bunjes, H.; Menzel, H., Encapsulation of proteins in hydrogel carrier systems for controlled drug delivery: Influence of network structure and drug size on release rate. *Journal of Biotechnology* **2013**, *163* (2), 243-249.
45. Park, M. R.; Chun, C.; Cho, C. S.; Song, S. C., Enhancement of sustained and controlled protein release using polyelectrolyte complex-loaded injectable and thermosensitive hydrogel. *European Journal of Pharmaceutics and Biopharmaceutics* **2010**, *76* (2), 179-188.
46. Branco, M. C.; Pochan, D. J.; Wagner, N. J.; Schneider, J. P., The effect of protein structure on their controlled release from an injectable peptide hydrogel. *Biomaterials* **2010**, *31* (36), 9527-9534.
47. Liu, Y. H.; Zhang, F. H.; Ru, Y. Y., Hyperbranched phosphoramidate-hyaluronan hybrid: A reduction-sensitive injectable hydrogel for controlled protein release. *Carbohydrate Polymers* **2015**, *117*, 304-311.
48. Xu, Y.; Lu, G.; Chen, M.; Wang, P.; Li, Z.; Han, X.; Liang, J.; Sun, Y.; Fan, Y.; Zhang, X., Redox and pH dual-responsive injectable hyaluronan hydrogels with shape-recovery and self-healing properties for protein and cell delivery. *Carbohydrate Polymers* **2020**, *250*, 116979.
49. Zhang, F. H.; Ru, Y. Y.; Liu, Y. H., Reduction-sensitive injectable hyperbranched polyphosphoramidate-hyaluronan hybrid hydrogels for controlled protein release. *Journal of Controlled Release* **2015**, *213*, E141-E142.
50. Wang, C.; Wang, M.; Xia, K.; Wang, J.; Cheng, F.; Shi, K.; Ying, L.; Yu, C.; Xu, H.; Xiao, S.; Liang, C.; Li, F.; Lei, B.; Chen, Q., A bioactive injectable self-healing anti-inflammatory hydrogel with ultralong extracellular vesicles release synergistically enhances motor functional recovery of spinal cord injury. *Bioactive Materials* **2021**, *6* (8), 2523-2534.
51. Balasubramanian, R.; Zhang, X., Mechanisms of FGF gradient formation during embryogenesis. *Seminars in cell & developmental biology* **2016**, *53*, 94-100.
52. Tassi, E.; McDonnell, K.; Gibby, K. A.; Tilan, J. U.; Kim, S. E.; Kodack, D. P.; Schmidt, M. O.; Sharif, G. M.; Wilcox, C. S.; Welch, W. J.; Gallicano, G. I.; Johnson, M. D.; Riegel, A. T.; Wellstein, A., Impact of Fibroblast Growth Factor-Binding Protein-1 Expression on Angiogenesis and Wound Healing. *The American Journal of Pathology* **2011**, *179* (5), 2220-2232.
53. Werner, S., A Novel Enhancer of the Wound Healing Process The Fibroblast Growth Factor-Binding Protein. *American Journal of Pathology* **2011**, *179* (5), 2144-2147.

54. Xie, L.; Zhang, M.; Dong, B.; Guan, M.; Lu, M.; Huang, Z.; Gao, H.; Li, X., Improved refractory wound healing with administration of acidic fibroblast growth factor in diabetic rats. *Diabetes Research and Clinical Practice* **2011**, *93* (3), 396-403.
55. Wu, Y.; Chang, T.; Chen, W.; Wang, X.; Li, J.; Chen, Y.; Yu, Y.; Shen, Z.; Yu, Q.; Zhang, Y., Release of VEGF and BMP9 from injectable alginate based composite hydrogel for treatment of myocardial infarction. *Bioactive Materials* **2021**, *6* (2), 520-528.
56. Nunes, Q. M.; Li, Y.; Sun, C.; Kinnunen, T. K.; Fernig, D. G., Fibroblast growth factors as tissue repair and regeneration therapeutics. *PeerJ* **2016**, *4*, e1535-e1535.
57. Pastar, I.; Stojadinovic, O.; Yin, N. C.; Ramirez, H.; Nusbaum, A. G.; Sawaya, A.; Patel, S. B.; Khalid, L.; Isseroff, R. R.; Tomic-Canic, M., Epithelialization in Wound Healing: A Comprehensive Review. *Advances in wound care* **2014**, *3* (7), 445-464.
58. Werner, S., A Novel Enhancer of the Wound Healing Process: The Fibroblast Growth Factor-Binding Protein. *The American Journal of Pathology* **2011**, *179* (5), 2144-2147.
59. Qu, J.; Zhao, X.; Liang, Y. P.; Xu, Y. M.; Ma, P. X.; Guo, B. L., Degradable conductive injectable hydrogels as novel antibacterial, anti-oxidant wound dressings for wound healing. *Chemical Engineering Journal* **2019**, *362*, 548-560.
60. Monien, B. H.; Cheang, K. I.; Desai, U. R., Mechanism of Poly(acrylic acid) Acceleration of Antithrombin Inhibition of Thrombin: Implications for the Design of Novel Heparin Mimics. *Journal of Medicinal Chemistry* **2005**, *48* (16), 5360-5368.
61. Kowal-Vern, A.; Orkin, B. A., Antithrombin in the treatment of burn trauma. *World Journal of Critical Care Medicine* **2016**, *5* (1), 17-26.
62. Li, J.; Mooney, D. J., Designing hydrogels for controlled drug delivery. *Nature Reviews Materials* **2016**, *1* (12), 16071.
63. Jhamb, S.; Vangaveti, V. N.; Malabu, U. H., Genetic and molecular basis of diabetic foot ulcers: Clinical review. *J Tissue Viability* **2016**, *25* (4), 229-236.
64. Haq, M. A.; Su, Y. L.; Wang, D. J., Mechanical properties of PNIPAM based hydrogels: A review. *Materials Science & Engineering C-Materials for Biological Applications* **2017**, *70*, 842-855.
65. Huang, K.; Wu, H. Y.; Jiang, F.; Shen, G. Z.; Wang, L., On the near-infrared light-responsive and mechanical properties of PNIPAM-based nanocomposite hydrogels. *Polymer Degradation and Stability* **2018**, *156*, 228-233.
66. Son, K. H.; Lee, J. W., Synthesis and Characterization of Poly(Ethylene Glycol) Based Thermo-Responsive Hydrogels for Cell Sheet Engineering. *Materials* **2016**, *9* (10), 13.

67. Raju, R.; Bandyopadhyay, S.; Sharma, A.; Gonzalez, S. V.; Carlsen, P. H.; Gautun, O. R.; Glomm, W. R., Synthesis, Characterization and Drug Loading of Multiresponsive p NIPAm-co-PEGMA (core)/p NIPAm-co-AAc (Shell) Nanogels with Monodisperse Size Distributions. *Polymers* **2018**, *10* (3), 14.
68. Hoare, T. R.; Kohane, D. S., Hydrogels in drug delivery: Progress and challenges. *Polymer* **2008**, *49* (8), 1993-2007.
69. Kondiah, P. J.; Choonara, Y. E.; Kondiah, P. P. D.; Marimuthu, T.; Kumar, P.; du Toit, L. C.; Pillay, V., A Review of Injectable Polymeric Hydrogel Systems for Application in Bone Tissue Engineering. *Molecules (Basel, Switzerland)* **2016**, *21* (11), 1580.
70. Xu, Y.; Ghag, O.; Reimann, M.; Sitterle, P.; Chatterjee, P.; Nofen, E.; Yu, H.; Jiang, H.; Dai, L. L., Development of visible-light responsive and mechanically enhanced “smart” UCST interpenetrating network hydrogels. *Soft Matter* **2018**, *14* (1), 151-160.
71. Haque, M. A.; Imamura, R.; Brown, G. A.; Krishnamurthi, V. R.; Niyonshuti, I. I.; Marcelle, T.; Mathurin, L. E.; Chen, J.; Wang, Y., An experiment-based model quantifying antimicrobial activity of silver nanoparticles on Escherichia coli. *RSC Advances* **2017**, *7* (89), 56173-56182.
72. Hoffman, R. K.; Surkiewicz, B. F.; Chambers, L. A.; Phillips, C. R., BACTERICIDAL ACTION OF MOVIDYN. *Industrial and Engineering Chemistry* **1953**, *45* (11), 2571-2573.
73. Sim, W.; Barnard, R. T.; Blaskovich, M. A. T.; Ziora, Z. M., Antimicrobial Silver in Medicinal and Consumer Applications: A Patent Review of the Past Decade (2007-2017). *Antibiotics-Basel* **2018**, *7* (4), 15.
74. Medici, S.; Peana, M.; Nurchi, V. M.; Lachowicz, J. I.; Crisponi, G.; Zoroddu, M. A., Noble metals in medicine: Latest advances. *Coordination Chemistry Reviews* **2015**, *284*, 329-350.
75. Khansa, I.; Schoenbrunner, A. R.; Kraft, C. T.; Janis, J. E., Silver in Wound Care-Friend or Foe?: A Comprehensive Review. *Plastic and Reconstructive Surgery-Global Open* **2019**, *7* (8), 10.
76. Pascu, B.; Negrea, A.; Ciopec, M.; Davidescu, C. M.; Negrea, P.; Gherman, V.; Duteanu, N., New Generation of Antibacterial Products Based on Colloidal Silver. *Materials* **2020**, *13* (7), 22.
77. Zheng, K. Y.; Yuan, X.; Goswami, N.; Zhang, Q. B.; Xie, J. P., Recent advances in the synthesis, characterization, and biomedical applications of ultrasmall thiolated silver nanoclusters. *Rsc Advances* **2014**, *4* (105), 60581-60596.
78. Acharya, D.; Singha, K. M.; Pandey, P.; Mohanta, B.; Rajkumari, J.; Singha, L. P., Shape dependent physical mutilation and lethal effects of silver nanoparticles on bacteria. *Scientific Reports* **2018**, *8*, 11.

79. Morones, J. R.; Elechiguerra, J. L.; Camacho, A.; Holt, K.; Kouri, J. B.; Ramirez, J. T.; Yacaman, M. J., The bactericidal effect of silver nanoparticles. *Nanotechnology* **2005**, *16* (10), 2346-2353.
80. Aliamradni, V.; Abolmaali, S. S.; Borandeh, S., Antifungal and Antibacterial Properties of Graphene-based Nanomaterials: A Mini-review. *Journal of Nanostructures* **2019**, *9* (3), 402-413.
81. Alqahtany, M.; Khadka, P.; Niyonshuti, I.; Krishnamurthi, V. R.; Sadoon, A. A.; Challapalli, S. D.; Chen, J. Y.; Wang, Y., Nanoscale reorganizations of histone-like nucleoid structuring proteins in Escherichia coli are caused by silver nanoparticles. *Nanotechnology* **2019**, *30* (38), 14.
82. Bera, R. K.; Mandal, S. M.; Raj, C. R., Antimicrobial activity of fluorescent Ag nanoparticles. *Letters in Applied Microbiology* **2014**, *58* (6), 520-526.
83. Meaad Alqahtany and Prabhat Khadka and Isabelle Niyonshuti and Venkata Rao Krishnamurthi and Asmaa, A. S. a. S. D. C. a. J. C. a. Y. W., Nanoscale reorganizations of histone-like nucleoid structuring proteins in escherichia coli are caused by silver nanoparticles. *Nanotechnology* **2019**.
84. Gharpure, S.; Akash, A.; Ankamwar, B., A Review on Antimicrobial Properties of Metal Nanoparticles. *Journal of Nanoscience and Nanotechnology* **2020**, *20* (6), 3303-3339.
85. Li, P.; Li, J.; Wu, C. Z.; Wu, Q. S., Synergistic antibacterial effects of beta-lactam antibiotic combined with silver nanoparticles. *Nanotechnology* **2005**, *16* (9), 1912-1917.
86. Park, H. J.; Kim, J. Y.; Kim, J.; Lee, J. H.; Hahn, J. S.; Gu, M. B.; Yoon, J., Silver-ion-mediated reactive oxygen species generation affecting bactericidal activity. *Water Research* **2009**, *43* (4), 1027-1032.
87. Duran, N.; Duran, M.; de Jesus, M. B.; Seabra, A. B.; Favaro, W. J.; Nakazato, G., Silver nanoparticles: A new view on mechanistic aspects on antimicrobial activity. *Nanomedicine-Nanotechnology Biology and Medicine* **2016**, *12* (3), 789-799.
88. Stabryla, L. M.; Johnston, K. A.; Millstone, J. E.; Gilbertson, L. M., Emerging investigator series: it's not all about the ion: support for particle-specific contributions to silver nanoparticle antimicrobial activity. *Environmental Science: Nano* **2018**, *5* (9), 2047-2068.
89. Mao, B. H.; Tsai, J. C.; Chen, C. W.; Yan, S. J.; Wang, Y. J., Mechanisms of silver nanoparticle-induced toxicity and important role of autophagy. *Nanotoxicology* **2016**, *10* (8), 1021-1040.
90. Salleh, A.; Ruth, N.; Nike Dewi, U.; Abdul Wahab, M.; Mahmoudi, E.; Mustafa, N.; Mh Busra, F., The Potential of Silver Nanoparticles for Antiviral and Antibacterial Applications: A Mechanism of Action. *Nanomaterials* **2020**, *10* (8), 1566.

91. Thill, A.; Zeyons, O.; Spalla, O.; Chauvat, F.; Rose, J.; Auffan, M.; Flank, A. M., Cytotoxicity of CeO₂ Nanoparticles for Escherichia coli. Physico-Chemical Insight of the Cytotoxicity Mechanism. *Environmental Science & Technology* **2006**, *40* (19), 6151-6156.
92. Sondi, I.; Salopek-Sondi, B., Silver nanoparticles as antimicrobial agent: a case study on E. coli as a model for Gram-negative bacteria. *J Colloid Interface Sci* **2004**, *275* (1), 177-82.
93. Lakshmi Prasanna, V.; Vijayaraghavan, R., Insight into the Mechanism of Antibacterial Activity of ZnO: Surface Defects Mediated Reactive Oxygen Species Even in the Dark. *Langmuir* **2015**, *31* (33), 9155-9162.
94. Li, H.; Huang, J.; Song, Y.; Zhang, M.; Wang, H.; Lu, F.; Huang, H.; Liu, Y.; Dai, X.; Gu, Z.; Yang, Z.; Zhou, R.; Kang, Z., Degradable Carbon Dots with Broad-Spectrum Antibacterial Activity. *ACS Appl Mater Interfaces* **2018**, *10* (32), 26936-26946.
95. Kankala, R. K.; Liu, C. G.; Chen, A. Z.; Wang, S. B.; Xu, P. Y.; Mende, L. K.; Liu, C. L.; Lee, C. H.; Hu, Y. F., Overcoming Multidrug Resistance through the Synergistic Effects of Hierarchical pH-Sensitive, ROS-Generating Nanoreactors. *ACS Biomater. Sci. Eng.* **2017**, *3* (10), 2431-2442.
96. Kankala, R. K.; Tsai, P. Y.; Kuthati, Y.; Wei, P. R.; Liu, C. L.; Lee, C. H., Overcoming multidrug resistance through co-delivery of ROS-generating nano-machinery in cancer therapeutics. *J. Mat. Chem. B* **2017**, *5* (7), 1507-1517.
97. Song, Z. Y.; Wu, Y.; Wang, H. J.; Han, H. Y., Synergistic antibacterial effects of curcumin modified silver nanoparticles through ROS-mediated pathways. *Materials Science & Engineering C-Materials for Biological Applications* **2019**, *99*, 255-263.
98. Abdal Dayem, A.; Hossain, M. K.; Lee, S. B.; Kim, K.; Saha, S. K.; Yang, G. M.; Choi, H. Y.; Cho, S. G., The Role of Reactive Oxygen Species (ROS) in the Biological Activities of Metallic Nanoparticles. *Int J Mol Sci* **2017**, *18* (1).
99. Zhang, L.; Wu, L.; Mi, Y.; Si, Y., Silver Nanoparticles Induced Cell Apoptosis, Membrane Damage of Azotobacter vinelandii and Nitrosomonas europaea via Generation of Reactive Oxygen Species. *Bulletin of Environmental Contamination and Toxicology* **2019**, *103* (1), 181-186.
100. Agnihotri, S.; Mukherji, S., Size-controlled silver nanoparticles synthesized over the range 5-100 nm using the same protocol and their antibacterial efficacy. *Rsc Advances* **2014**, *4* (8), 3974-3983.
101. Huk, A.; Izak-Nau, E.; Reidy, B.; Boyles, M.; Duschl, A.; Lynch, I.; Dusinska, M., Is the toxic potential of nanosilver dependent on its size? *Particle and Fibre Toxicology* **2014**, *11*, 16.
102. Kubo, A. L.; Capjak, I.; Vrcek, I. V.; Bondarenko, O. M.; Kurvet, I.; Vija, H.; Ivask, A.; Kasemets, K.; Kahru, A., Antimicrobial potency of differently coated 10 and 50 nm silver nanoparticles against clinically relevant bacteria Escherichia coli and Staphylococcus aureus. *Colloids and Surfaces B-Biointerfaces* **2018**, *170*, 401-410.

103. Ginjupalli, K.; Shaw, T.; Tellapragada, C.; Alla, R.; Gupta, L.; Perampalli, N. U., Does the size matter? Evaluation of effect of incorporation of silver nanoparticles of varying particle size on the antimicrobial activity and properties of irreversible hydrocolloid impression material. *Dental Materials* **2018**, *34* (7), e158-e165.
104. Kim, T. H.; Kim, M.; Park, H. S.; Shin, U. S.; Gong, M. S.; Kim, H. W., Size-dependent cellular toxicity of silver nanoparticles. *Journal of Biomedical Materials Research Part A* **2012**, *100A* (4), 1033-1043.
105. Ivask, A.; ElBadawy, A.; Kaweeteerawat, C.; Boren, D.; Fischer, H.; Ji, Z. X.; Chang, C. H.; Liu, R.; Tolaymat, T.; Telesca, D.; Zink, J. I.; Cohen, Y.; Holden, P. A.; Godwin, H. A., Toxicity Mechanisms in Escherichia coli Vary for Silver Nanoparticles and Differ from Ionic Silver. *Acs Nano* **2014**, *8* (1), 374-386.
106. Gordienko, M. G.; Palchikova, V. V.; Kalenov, S. V.; Belov, A. A.; Lyasnikova, V. N.; Poberezhniy, D. Y.; Chibisova, A. V.; Sorokin, V. V.; Skladnev, D. A., Antimicrobial activity of silver salt and silver nanoparticles in different forms against microorganisms of different taxonomic groups. *Journal of Hazardous Materials* **2019**, *378*, 120754.
107. Alshareefa, A.; Laird, K.; Cross, R. B. M., Shape-dependent antibacterial activity of silver nanoparticles on Escherichia coli and Enterococcus faecium bacterium. *Applied Surface Science* **2017**, *424*, 310-315.
108. Tak, Y. K.; Pal, S.; Naoghare, P. K.; Rangasamy, S.; Song, J. M., Shape-Dependent Skin Penetration of Silver Nanoparticles: Does It Really Matter? *Scientific Reports* **2015**, *5*, 11.
109. Helmlinger, J.; Sengstock, C.; Gross-Heitfeld, C.; Mayer, C.; Schildhauer, T. A.; Koller, M.; Epple, M., Silver nanoparticles with different size and shape: equal cytotoxicity, but different antibacterial effects. *Rsc Advances* **2016**, *6* (22), 18490-18501.
110. Cheon, J. Y.; Kim, S. J.; Rhee, Y. H.; Kwon, O. H.; Park, W. H., Shape-dependent antimicrobial activities of silver nanoparticles. *International Journal of Nanomedicine* **2019**, *14*, 2773-2780.
111. de Melo, A. P. Z.; Maciel, M.; Sganzerla, W. G.; Almeida, A. D.; de Armas, R. D.; Machado, M. H.; da Rosa, C. G.; Nunes, M. R.; Bertoldi, F. C.; Barreto, P. L. M., Antibacterial activity, morphology, and physicochemical stability of biosynthesized silver nanoparticles using thyme (*Thymus vulgaris*) essential oil. *Materials Research Express* **2020**, *7* (1), 12.
112. Tang, S.; Zheng, J., Antibacterial Activity of Silver Nanoparticles: Structural Effects. *Adv Healthc Mater* **2018**, *7* (13), e1701503.
113. Nicomrat, D.; Chamutpong, S., Effects of Silver Nanoparticles on Heterotrophic Bacterial Community Inhabiting the Anoxic Paddy Soil of Flooded Rice Microcosms. *Applied Mechanics and Materials* **2017**, *866*, 152-155.

114. Song, Y. Y.; Jiang, H. J.; Wang, B. B.; Kong, Y.; Chen, J., Silver-Incorporated Mussel-Inspired Polydopamine Coatings on Mesoporous Silica as an Efficient Nanocatalyst and Antimicrobial Agent. *Acs Applied Materials & Interfaces* **2018**, *10* (2), 1792-1801.
115. El-Sayed, R.; Ye, F.; Asem, H.; Ashour, R.; Zheng, W. Y.; Muhammed, M.; Hassan, M., Importance of the surface chemistry of nanoparticles on peroxidase-like activity. *Biochemical and Biophysical Research Communications* **2017**, *491* (1), 15-18.
116. Tran, H. A.; Ly, K. L.; Fox, K. E.; Tran, P. A.; Nguyen, T. H., Immobilization of Antimicrobial Silver and Antioxidant Flavonoid as a Coating for Wound Dressing Materials. *International Journal of Nanomedicine* **2019**, *14*, 9929-9939.
117. Xiong, Y. J.; Brunson, M.; Huh, J.; Huang, A. R.; Coster, A.; Wendt, K.; Fay, J.; Qin, D., The Role of Surface Chemistry on the Toxicity of Ag Nanoparticles. *Small* **2013**, *9* (15), 2628-2638.
118. Long, Y. M.; Hu, L. G.; Yan, X. T.; Zhao, X. C.; Zhou, Q. F.; Cai, Y.; Jiang, G. B., Surface ligand controls silver ion release of nanosilver and its antibacterial activity against Escherichia coli. *International Journal of Nanomedicine* **2017**, *12*, 3193-3206.
119. Das, B.; Tripathy, S.; Adhikary, J.; Chattopadhyay, S.; Mandal, D.; Dash, S. K.; Das, S.; Dey, A.; Dey, S. K.; Das, D.; Roy, S., Surface modification minimizes the toxicity of silver nanoparticles: an in vitro and in vivo study. *Journal of Biological Inorganic Chemistry* **2017**, *22* (6), 893-918.
120. Zhang, J.; Xiang, Q.; Shen, L.; Ling, J.; Zhou, C.; Hu, J.; Chen, L., Surface charge-dependent bioaccumulation dynamics of silver nanoparticles in freshwater algae. *Chemosphere* **2020**, *247*, 125936.
121. Gitipour, A.; Thiel, S. W.; Scheckel, K. G.; Tolaymat, T., Anaerobic toxicity of cationic silver nanoparticles. *Science of The Total Environment* **2016**, *557-558*, 363-368.
122. Rasheed, P. A.; Jabbar, K. A.; Mackey, H. R.; Mahmoud, K. A., Recent advancements of nanomaterials as coatings and biocides for the inhibition of sulfate reducing bacteria induced corrosion. *Current Opinion in Chemical Engineering* **2019**, *25*, 35-42.
123. Slavin, Y. N.; Asnis, J.; Häfeli, U. O.; Bach, H., Metal nanoparticles: understanding the mechanisms behind antibacterial activity. *J Nanobiotechnology* **2017**, *15* (1), 65.
124. Lin, S. H.; Cheng, Y. W.; Liu, J.; Wiesner, M. R., Polymeric Coatings on Silver Nanoparticles Hinder Autoaggregation but Enhance Attachment to Uncoated Surfaces. *Langmuir* **2012**, *28* (9), 4178-4186.

125. Wu, K.; Yang, Y.; Zhang, Y. M.; Deng, J. X.; Lin, C. J., Antimicrobial activity and cytocompatibility of silver nanoparticles coated catheters via a biomimetic surface functionalization strategy. *International Journal of Nanomedicine* **2015**, *10*, 7241-7252.
126. Mazloomi-Rezvani, M.; Salami-Kalajahi, M.; Roghani-Mamaqani, H.; Pirayesh, A., Effect of surface modification with various thiol compounds on colloidal stability of gold nanoparticles. *Applied Organometallic Chemistry* **2018**, *32* (2), 11.
127. Choi, S. H.; Jang, Y. S.; Jang, J. H.; Bae, T. S.; Lee, S. J.; Lee, M. H., Enhanced antibacterial activity of titanium by surface modification with polydopamine and silver for dental implant application. *Journal of Applied Biomaterials & Functional Materials* **2019**, *17* (3), 9.
128. Lok, C. N.; Ho, C. M.; Chen, R.; He, Q. Y.; Yu, W. Y.; Sun, H.; Tam, P. K. H.; Chiu, J. F.; Che, C. M., Silver nanoparticles: partial oxidation and antibacterial activities. *Journal of Biological Inorganic Chemistry* **2007**, *12* (4), 527-534.
129. Chen, D.; Li, X.; Soule, T.; Yorio, F.; Orr, L., Effects of solution chemistry on antimicrobial activities of silver nanoparticles against *Gordonia* sp. *Science of the Total Environment* **2016**, *566*, 360-367.
130. Tejamaya, M.; Romer, I.; Merrifield, R. C.; Lead, J. R., Stability of Citrate, PVP, and PEG Coated Silver Nanoparticles in Ecotoxicology Media. *Environmental Science & Technology* **2012**, *46* (13), 7011-7017.
131. Ali, S.; Perveen, S.; Ali, M.; Jiao, T. H.; Sharma, A. S.; Hassan, H.; Devaraj, S.; Li, H. H.; Chen, Q. S., Bioinspired morphology-controlled silver nanoparticles for antimicrobial application. *Materials Science & Engineering C-Materials for Biological Applications* **2020**, *108*, 12.
132. Guo, A. Y.; Mu, Q. Z.; Cai, A. J.; Wang, X. P., Mussel-inspired green synthesis of Ag-coated polydopamine microspheres for selective antibacterial performance. *Micro & Nano Letters* **2019**, *14* (4), 394-398.
133. Jurasin, D. D.; Curlin, M.; Capjak, I.; Crnkovic, T.; Lovric, M.; Babic, M.; Horak, D.; Vrcek, I. V.; Gajovic, S., Surface coating affects behavior of metallic nanoparticles in a biological environment. *Beilstein Journal of Nanotechnology* **2016**, *7*, 246-262.

Chapter II: Biocompatible, Injectable based on Poly (Oligo Ethylene Glycol Monoacrylate-Acrylic Acid- N-Isopropylacrylamide) Anionic Hydrogel for Delivery of Fibroblast Growth Factors to Enhance Wound Healing*

2.1. Abstract

Biocompatible injectable hydrogels have gained much attention for protein delivery applications due to their minimal invasiveness and adaptability for irregularly shaped delivery sites; however, sustained release of bioactive proteins remains challenging. In this work, an anionic injectable hydrogel based on poly (oligoethylene glycol monoacrylate, acrylic acid-N-isopropylacrylamide, P(OEGA-AA-NIPAM), was developed using a free-radical polymerization reaction. Incorporating PNIPAM to the P(OEGA-AA) spaces out the charge distribution of the anionic gel allowing for the increase of the positively charged protein release. The presence of three components of the gels was confirmed by spectroscopic study while the thermal stability enhanced with increased amount of AA in the gel or decreased amount of NIPAM. The hydrogels exhibited no cytotoxic effects on human cells demonstrating their biocompatibility. P(OEGA-AA-NIPAM) hydrogels showed the capabilities for a sustained release of human acidic growth factor (hFGF1) and its mutations under physiological conditions. The released hFGF1 remained bioactive and promoted fibroblast's proliferation both *in vitro* and *in vivo*. Incorporating NIPAM in the POEGA based hydrogel has significantly enhanced release kinetics of hFGF1 by 6 times compared to the P(OEGA-co-AA) hydrogel. This study promises a potential drug delivery system with tunable charge distribution, hence control over release rate of bioactive positively charged proteins for wound healing applications.

***To be submitted:** Isabelle I. Niyonshuti, Shilpi Agrawal, Gianna T. Busch, Ravi K. Gundampati, Thallapuram K. Suresh Kumar, Kyle Quinn, and Jingyi Chen

2.2. Introduction

Hydrogels are three-dimensional networks of polymers with high water retention properties given by the hydrophilic functional groups attached to the backbone of their polymeric structure.¹ Hydrogels resemble the native extracellular matrix, which make them useful in many biomedical applications. Over the past few decades, hydrogels have raised a lot of interests because of their ability for water retention, biocompatibility, and flexibility which rendered them very applicable in drug delivery systems.² Water soluble polymers used to make hydrogels can provide increased half-life, protection of drug against degrading enzymes and increased water solubility for hydrophobic drugs. Among hydrogels, injectable hydrogels have gotten much attention in drug delivery in the last decade because of minimal invasiveness, reaching to deep tissues defect, specificity to local delivery and their easy handling.³

Poly(ethylene) glycol (PEG)-based injectable hydrogels have extensively been studied for their applications in drug delivery. PEG is known for its biocompatibility, neutrality, and antibiofouling properties that are desired for delivery systems.⁴⁻⁶ Therefore, PEG-hydrogels have shown important role in providing a controlled and sustained release of active therapeutics for important cellular functions.^{4, 5, 7, 8} More interestingly, PEG has been used to modify non-biocompatible and non-biodegradable polymers to improve their properties desired in biomedical applications. Despite their great properties, PEG hydrogels suffer from weak mechanical properties which can limit their applications. Researchers have modified PEG hydrogels by functionalizing them with biomolecules or other monomers to enhance their chemical, physical, and mechanical properties. For instance, poly (acrylic acid) (PAA) was incorporated in PEG to make double network PEG-PAA hydrogels with extremely high mechanical properties, biocompatibility, and hydrophilicity for biomedical applications.⁹ In this case PAA also brings a

negative charge to the neutral PEG and enhance its functionalities, and protein resistivity of both PEG and PAA is of great advantage. Nguyen et al elaborated the feasibility of preparing poly(amidoamine)-poly(ethylene glycol)-poly(amidoamine) (PAA-PEG-PAA) with enhanced bioadhesive properties and capabilities to prolong the retention of Flubiprofen.¹⁰ Other studies have used synthetic polymers to enhance mechanical properties of PEG hydrogels by making interpenetrating polymer networks (IPNs).^{9, 11-13} We recently developed a fast and simple synthesis method to prepare an injectable hydrogel based on P(OEGA-co-AA) using a free-radical polymerization reaction.^{13, 14} The copolymers were prepared in two steps where the POEGA and AA are reacted with N, N'-Methylenebisacrylamide (MBAm) as a crosslinker, in presence of ammonium persulfate (APS) as a initiator then the copolymer was swollen in PBS to make injectable anionic hydrogel.¹⁴ Other different methods such as click-chemistry have been employed to prepare PEG-based hydrogels for protein delivery, but these methods do not give opportunity to control the network structure and some use metals such as copper as catalysts whose ions can be cytotoxic.^{5, 15 16} Therefore, simple chain-growth method is preferable for synthesis of PEG-based hydrogel to have tailorable hydrogel properties without compromising the biocompatibility.

Moreover, stimuli responsive hydrogels have been explored as drug delivery systems because a specific stimulus (i.e temperature, pH, light) can be used to effectively tune delivery of therapeutics from the hydrogels as they account for a typical environmental condition occurring at the site of disease. Poly (N-isopropylacrylamide), PNIPAM is a thermo-responsive polymer that is known to have a lower critical solution temperature (LCST) that is close to human body temperature making it unique for applications in biomedical applications.^{17,18} Therefore, PNIPAM based hydrogels have been used as drug delivery systems as they can release drug at human body

temperature due to its change in structure.^{19,20} This temperature responsiveness of PNIPAM comes from the weak balance between its monomers' hydrophobic (propyl group) and hydrophilic (amide group) moieties.²¹ When there is a change in temperature, polymer-polymer and polymer-solvent interactions change and dictate the state of the hydrogel. At the temperature lower than LCST the amide groups (-CONH-) from NIPAM monomer is solvated by the water molecules making it soluble and when the temperature is higher than its LCST the hydrogen interactions are weakened and the hydrophobic groups (-CH(CH₃)₂) interactions become strong.^{14, 17, 22} Therefore, the polymer undergoes phase separation where it expels water molecules out from the polymer networks due to dominant hydrophobic interactions between isopropyl groups.^{17,23} The change in structure of PNIPAM upon change in temperature is taken advantage of for drug delivery applications.^{24,25,26} Native PNIPAM hydrogels often experience slow temperature response on top of their weak mechanical properties. Therefore, properties of PNIPAM such as its LCST can be regulated by copolymerization with other monomers to meet intended applications.²⁷ Researchers demonstrated that adding PEG increases thermo-responsiveness of PNIPAM by providing the pores that can allow water flow at high temperature that otherwise PNIPAM would not be able to do.^{28, 29} More recently, PEG was reported to increase degradation temperature of PNIPAM when it was added to the PNIPAM hydrogel at high temperature.³⁰ Like other polymers, PNIPAM is prone to poor mechanical properties because of the intense swelling that lead to low density of its polymeric chains.¹⁷ The poor mechanical strength of PNIPAM has been addressed by adding other monomers to make IPNs^{12, 13, 31} in which the crosslinking between two networks in IPNs can be adjusted to improve the mechanical properties of the hydrogel without compromising other properties.³² Making PNIPAM nanocomposites³³ and adding side ring molecules/polymers³⁴ also proved to increase their mechanical strength. The mechanical strength of PNIPAM depends on the

applications intended and the polymer can be modified to achieve desired mechanical strength depending on the application.

Controlled site-specific delivery of therapeutics from biocompatible PEG- based injectable hydrogels in wound healing can provide enhanced therapeutic efficiency and maintain the therapeutic concentration. Delivery of proteins from the hydrogel system have been proven to depend on swelling behaviors of the hydrogel which dictate the diffusion of loaded proteins out of the hydrogel matrix.³⁵ Therefore, the release kinetics can be regulated by controlling the rate of swelling of hydrogel or diffusion of proteins or both.^{8, 36} However, diffusion-controlled delivery is associated with a rapid burst release of drugs which is not desired for delivery of therapeutics such as growth factors that usually require small amount to reach their therapeutic effect and can cause adverse effect when their therapeutic margin is exceeded. In addition, a sustained release is a necessity to ensure a complete long process of tissue regeneration that can take up to months to complete.³⁷ Therefore, there is a need for hydrogels formulations that can provide sustained release of such therapeutics. In addition, slow responsiveness of some hydrogels makes it hard to be used for drug delivery, so improving the responsiveness of such hydrogels by copolymerizing them with other monomers will help to reach desired release profile of various drugs.

Taking into consideration PEG's excellent tunable properties and biocompatibility and PNIPAM thermo-responsiveness when modified with other polymers, we developed injectable hydrogels based on Poly (Oligo Ethylene Glycol Monoacrylate-*co*-Acrylic Acid-*co*- N-isopropylacrylamide) [P(OEGA-AA-NIPAM)]. Introducing NIPAM would bring thermo-responsive properties to the copolymer in physiological conditions that is desired for drug delivery application intended. A slow release rate of human acidic growth factor (hFGF1) from P(OEGA-*co*-AA) hydrogel in physiological conditions we recently observed¹⁴ and associated to heavy

positive charges on the protein can be improved by tuning the distribution of the negative charges in the anionic hydrogels. NIPAM's neutrality would help to space out the negative charges when incorporated in the anionic P(OEGA-*co*-AA) hydrogel which would improve the release profile of hFGF1 as electrostatic interactions, the key factor for the release rate, between the positively charged protein and anionic hydrogel will be minimized to enable faster but sustained release rate in physiological conditions. Moreover, thermo-responsiveness of PNIPAM will be of advantage for controlled release in physiological conditions as the hydrogel collapses at temperature above its LCST near body temperature to release loaded protein.³⁸ It is important to keep hydrogel properties such as biocompatibility after NIPAM is incorporated, so important properties of the P(OEGA-AA-NIPAM) were studied. We used hFGF1 with $pI > 7.0$ and mutated FGF proteins and bovine serum albumin (BSA, $pI = 5.4$) as a control to demonstrate the capacity of the new anionic hydrogel system for controlled and sustained release of positively charged proteins. The *in vivo* pilot animal study was done to evaluate the effect of controlled release of hFGF1 from P(OEGA-AA-NIPAM) hydrogel on wound healing.

2.3. Experimental methods

Materials and chemicals: POEGA (average $M_n = 480$), AA, DPBS (10 mM, pH 7.4) were purchased from Sigma-Aldrich. NIPAM was purchased from TCI. MBAm and KBr were purchased from Alfa Aesar. APS was purchased from VWR. Dialysis membrane (MWCO 2 kDa) was purchased from Spectrum Laboratories. Transwell membrane plates were purchased from Corning Incorporated. Inhibitors were removed POEGA and AA by purification through a basic and neutral Al_2O_3 columns for PEOGA and AA, respectively. APS was recrystallized from ethanol/water (1:1) while MBAm was recrystallized from ethanol. NIPAM was recrystallized from

hexanes and few drops of acetone. All other chemicals were used as received and ultrapure 18 MΩ H₂O was used in all procedures unless specified.

2.3.1. Synthesis of injectable anionic hydrogels

P(OEGA-AA-NIPAM) injectable anionic hydrogel was prepared using an established simple and robust free radical polymerization method described by Wang et al.¹⁴ The hydrogel was synthesized from copolymerization of PEOGA, AA and NIPAM. In a typical experiment, 1g of monomers (PEOGA, AA, and NIPAM) and crosslinker, N, N'-Methylenebisacrylamide (MBAm, 0.1 mmol). was dissolved 10 ml of water and purged under N₂ for 5 minutes. The mix was then transferred to a 25-mL Stopcock, Airfree, Schlenk flask and exposed to N₂ and three evacuate refill cycles with Argon to purge dissolved oxygen then it was incubated at 70 °C under argon. After 30 minutes, 200 μl of aqueous APS (15 mg) was added to the flask under argon flow, followed by another three evacuate-refill cycles. The reaction was left to run for 5 min under magnetic stirring at 350 rpm. After another 5 minutes, the reaction was stopped by cooling the flask in an ice bath for 15 minutes. The mix was then dialyzed in MWCO 2kDa membrane in 1L of water for a week while renewing water every day to remove residual monomers. The hydrogel solution was lyophilized in vacuum dryer at 70 °C to make a dry gel. The dry copolymer was swollen in 10 ml of 1x DPBS buffer for 24 h to make the injectable anionic hydrogel.

2.3.2. Characterization methods

The copolymers were characterized by chemical structure using FTIR to ensure that all the monomers were incorporated in the hydrogels. The FTIR spectrum of the copolymers were attained on an FTIR spectrometer (Shimadzu IRAffinity-1S) using a KBr pellet method where about 10 mg of the lyophilized copolymer was used. The FTIR spectra were recorded between

400-4000 cm^{-1} at resolution 4. Thermal stability of the copolymers was investigated using DSC measurements, about 5 mg of each copolymer was put in a standard aluminum sample pan and covered with aluminum lid. The pan was crimped with a crimp press SSCP-1. An empty aluminum sample pan was used as a control and measurements were done at the rate of 40 $^{\circ}\text{C}/\text{min}$ and hold temperature was set to 500 $^{\circ}\text{C}$ using a DSC calorimeter (PerkinElmer Pyris-Diamond). Control-Heating (3 cycles) DSC curve was recorded over 50-500 $^{\circ}\text{C}$ to track thermal transitions of the copolymer. The thermograms were taken using a TGA instrument (TA Q50) where 25 mg of the copolymer was used. The sample was equilibrated for 10 min at 30 $^{\circ}\text{C}$ and run under N_2 at a flow rate of 60 mL min^{-1} from 30 to 500 $^{\circ}\text{C}$ at a rate of 10 $^{\circ}\text{C min}^{-1}$. Swelling behaviors of the copolymers were studied by incubating around 150 mg (W_d) of the dry hydrogel in 2 mL of simulated body fluid (pH 7.4) in a transwell membrane plate and incubated at 37 $^{\circ}\text{C}$ with mild shaking. Changes of weight and swelling degree of hydrogel were measured and normalized to their initial values before swelling and degradation. At predetermined time intervals (7, 10, 28, 31, and 40 days), the hydrogel samples were removed, and the swollen hydrogel sample weights were measured (W_s), then the hydrogel was lyophilized, and the weight was recorded (W_f).

2.3.3. Cytotoxicity studies

Cytotoxicity studies of P(OEGA-AA-NIPAM) were performed using modified version of already known protocol reported by Cooperstein et al.^{39, 40} In the normal procedure, polymer was lyophilized for 3 days. Around 200 mg of dry hydrogels (Gel 900 and Gel 6) were sterilized by leaving them under UV light for 2 hours. The polymers were incubated in DMEM culture media for 72 hrs at 37 $^{\circ}\text{C}$ in CO_2 incubator (5%). Fibroblast cells were then incubated in culture media to 80% confluency. The polymers were isolated from extract media (stock :0.001 $\text{g}/\mu\text{L}$) and diluted with media to obtain different concentrations ranging from 0-30% polymer. Polymer of different

concentrations (polymer weights per volume) were added to the 96-well plate coated with cells to the total volume of 100 μ l; cell number 10,000 cells/well. After incubation for 72 hours, the viability of the fibroblast cells was measured by 3-(4, 5-dimethylthiazolyl-2)-2, 5-diphenyltetrazolium bromide (MTT) assay. Cells growth in just the media were used as a control.

2.3.4. *In vitro* proteins release studies

In vitro release studies of the injectable P(OEGA-AA-NIPAM) hydrogel were conducted in 12 transwell membrane plates. In a typical experiment, around 200 μ L of the injectable hydrogel was mixed with a certain amount of protein at the final concentration of 1 mg/mL and the mix was stored at 4 $^{\circ}$ C overnight. After incubation, the mixture of gel and protein was transferred to a transwell membrane insert (12 mm diameter, 3 μ m pore size) then immersed in 1.5 mL of DPBS (pH 7.4). The sample was shaken at 150 rpm throughout the release experiment at 37 $^{\circ}$ C. At different time points 1.5 mL of release media containing protein was taken for fluorescence measurements then replaced by fresh media. The emission spectra were collected at excitation wavelength of 280 nm and 295nm and emission wavelengths of 309 nm, and 345 nm in the range of 300-400 nm for hFGF1 and BSA respectively. Percentage of cumulatively released proteins was calculated using developed calibration curves corresponding to the protein. After fluorescence measurements, the samples were kept at 4 $^{\circ}$ C for bioactivity assays. The bioactivity of released hFGF1 was evaluated by cell proliferation assay. Briefly, NIH fibroblast cells were grown to 80% confluency and then incubated with 50 ng/mL of the released protein/hFGF1 in serum-supplemented media at a concentration of 10,000 cell per well. The cell viability was determined by Cell Titer-Glo luminescent assay.

2.3.5. *In vivo* animal study for controlled release of hFGF1 from Gel 8 for wound closure

The injectable P(OEGA-AA-NIPAM) hydrogel, Gel 8 capacity of sustained release of hFGF1 was tested *in vivo*. The hydrogels were first sterilized by leaving them in a Biohood, under UV light for 2 h. The PBS/Borax (0.1 w/v%) buffer was also sterilized at the same time. Then, the gels are diluted to the final concentration by adding FGF containing PBS/Borax mixture and wait for 2 hours for hydrogel to swell into injectable hydrogel. Working concentration of protein was 1 mg/mL. Total volume of the control and loaded hydrogels was 3 mL. First prepare 10 mL 2.0 X PBS from 2 mL 10 X PBS by adding 8 mL water. Then 10 mg of Borax was added to 10 mL 2 X PBS, heating at 100 °C until all the solid were dissolved. The Borax was cooled down at room temperature. The pH of the sample was recorded to be about 8. Then, 20 µl of HCl was added the buffer to reduce the pH to 7-7.2. Then, 1.5 mL of 2 X PBS (borax 0.1 v/w %) to 1.5 g of control sterile hydrogel, left it in the biohood for 2 h for swelling (no UV light) into injectable hydrogel. To make concentrated hydrogel for loading of hFGF1, 1.0 mL of 2 X PBS (borax 0.1 v/w %,) was mixed with 1.0 ml of hFGF1 (3 mg/mL). Then the mixture was added to concentrated sterile gel 8 left in the biohood for 2 h for swelling into injectable hydrogel. The gel was shaken for several mins to make sure hFGF1 dispersed well. For wound closure experiment, every mice received 100µL of either an hFGF1-loaded gel 8 or an unloaded control gel. Wounds were bandaged with Tegaderm and a secondary layer of surgical tape to prevent Tegaderm removal. Wound size was monitored by tracing the wound borders on days 0, 1, 3, 5, 7, and 10. The average wound area was calculated using Custom MATLAB code that quantified the area of each trace.⁴¹ Although all metrics of wound size were calculated for both the top and the bottom wounds, the values for the bottom wounds were used in statistical analysis.

2.4. Results and discussion

Synthesis of P(OEGA-AA-NIPAM) injectable hydrogel

Different formulations of biocompatible injectable hydrogel based on PEG was prepared using our previously-established protocol with modifications.¹⁴ The hydrogel was synthesized by copolymerization of three monomers, OEGA, AA and NIPAM in aqueous medium to make P(OEGA-AA-NIPAM). This reaction happens through radical polymerization reaction initiated by APS (**Figure 1**) where MBAm was used as a crosslinker. We systematically developed 8 different formulations by changing molar ratios between the three monomers to evaluate the effect of each monomer content on hydrogel properties (**Table 1**). Gel 7 has the highest OEGA molar content, Gel 1 has the highest AA concentration and Gel 8 has the highest NIPAM content (**Table 1**). It was observed that increasing the weight of OEGA in the formulation increases fluidity of the hydrogel, same thing that was previously observed in P(OEGA-co-AA) hydrogel.¹⁴ The order of increasing PEOGA molar ratio in hydrogel formulations was Gel 1 < Gel 6 < Gel 5 < Gel 4 < Gel 8 < Gel 3 < Gel 2 < Gel 7. This is explained by the fact that POEGA is the backbone polymer for the hydrogel, and its hydrophilicity dominate in the structure.

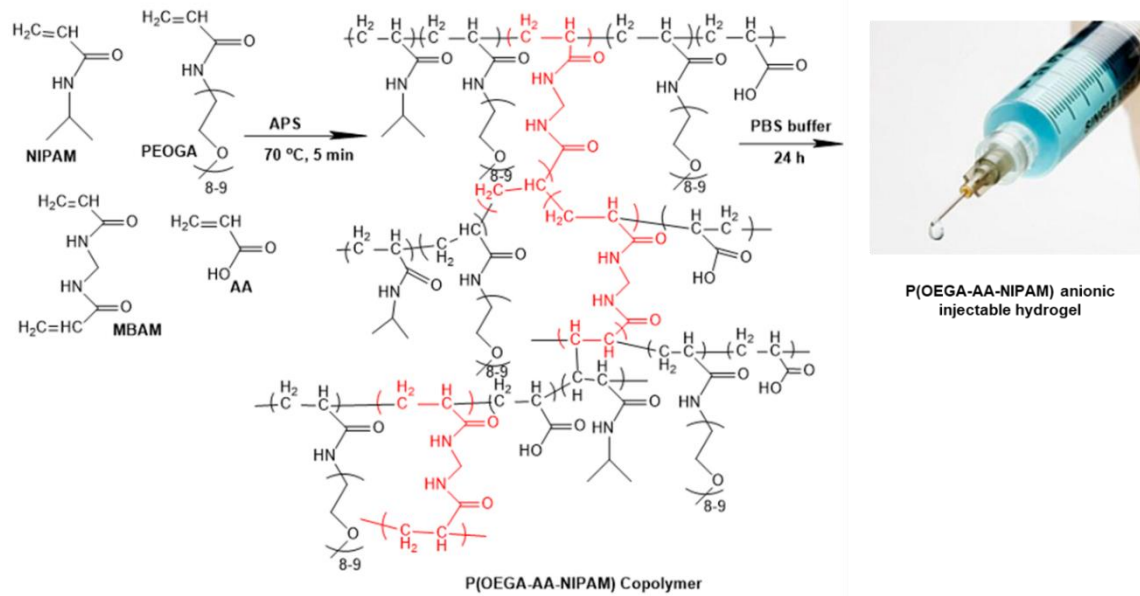


Figure 1: A Schematic showing mechanism of synthesis of injectable anionic P(OEGA-AA-NIPAM) hydrogel via a free-radical polymerization reaction. The crosslinker, MBAM is highlighted in red.

In addition, more AA increased viscosity of the hydrogel because of more hydrogen bonding and other intermolecular interactions in the polymer chain. For instance, Gel 1, which has the lowest OEGA concentration and highest AA among the formulations was very viscous (**Figure S1**). To optimize the right molar concentration of hydrogel the judgement was based on hydrogel physical properties such as fluidity. The more injectable the formulation was the better it would be applied for *in vivo* controlled release experiments for wound healing application. Crosslinking extent was tuned by varying the molar ratios between crosslinker to monomers (**Table 1**). By increasing the molar percent of crosslinker (MBAm) to monomers (i.e. lightly to highly crosslinked) the number of efficient cross-links per unit volume increases, therefore crosslink density and network chain density increase.^{42, 43} Also, by increasing the number of crosslinks per unit volume there is less volume to accommodate water and hence the degree of swelling is expected to decrease.

Table 1: Different formulations of injectable anionic hydrogels based on P(OEGA-AA-NIPAM).

Sample ID	OEGA/AA/NIPAM (w/w/w, mg)	OEGA/AA/NIPAM (mol/mol/mol, mmol)	MBAM (mmol)	MBAM/(OEGA+AA+NIPAM) (mol/mol/mol, mmol)	APS (mg)	Time (min)	Temp (°C)	Volume (mL)
Gel 1	700/200/100	0.29/0.52/0.17	0.1	0.1/4.97	15	5	70	10
Gel 2	900/50/50	0.63/0.22/0.14	0.1	0.1/2.97	15	5	70	10
Gel 3	900/75/25	0.60/0.32/0.07	0.1	0.1/3.08	15	5	70	10
Gel 4	850/100/50	0.50/0.37/0.12	0.1	0.1/3.52	15	5	70	10
Gel 5	800/100/100	0.43/0.34/0.22	0.1	0.1/3.86	15	5	70	10
Gel 6	800/150/50	0.40/0.48/0.10	0.1	0.1/4.08	15	5	70	10
Gel 7	900/10/90	0.66/0.04/0.28	0.1	0.1/3.80	15	5	70	10
Gel 8	850/25/125	0.55/0.10/0.34	0.1	0.1/3.20	15	5	70	10

Characterization of the injectable hydrogels

The IR spectra of all the copolymers tested show major peaks representing monomers used during formulation. The -OH stretch small peak around 3000 cm^{-1} , C-H from POEGA around 2870 cm^{-1} , ester C=O stretch around 1730 cm^{-1} and amide C=O stretch band at 1645 cm^{-1} and C-O from PEOGA were present in all formulations (**Figure 2B**). There is also band around 3500 cm^{-1} that represents NH stretch band from PNIPAM and MBAM in all copolymers.^{3,4} All the hydrogels have similar peaks; however, their peak intensity reflects the monomers content used in the hydrogel. For instance, ester C=O peak intensities at 1735 cm^{-1} are weak for Gel 8 and Gel 7 representing their low AA content of 10% and 4% AA, respectively compared to other

formulations. In addition, the peak integration by area shows a correlation between peak area and number of monomers in the hydrogel. For instance, C=O and C-O peaks are the weakest for Gel 1 because it has the highest molar ratio of (MBAm+OEGA+AA+NIPAM) to (OEGA+MBAm) (**Table 1**). Gel 1 also has a high area of COOH peak which could suggest presence of both amide and COOH functional groups from NIPAM and AA, respectively. The peak around 1645 cm^{-1} could be associated with C=O stretch weakly coupled to C-N stretch and N-H bending from amide group of NIPAM. C=O peak of carbonyl at 1730 cm^{-1} (from AA, OEGA, and MBAm) to C=O peak of amide ratio is different and dependent on NIPAM content of the formulation. Gel 8 (34% NIPAM) has the highest ratio of 0.84 as result of more amide functional groups than any of the other formulations. The ratio of two C=O peaks was found to increase as the molar concentration of NIPAM increased in the formulation (**Figure 2D**). Other hydrogels seem to have no significant difference in peak area nor peak positions of the main functional groups because there is little difference between molar compositions of the monomers in the hydrogels. FTIR data suggest that all three monomers and crosslinker were incorporated in the hydrogels and the amount of monomer was reflected by the intensity of the peaks representing its main functional groups. Raman spectrum of Gel 8 agrees with FTIR data showing the main peaks as the FTIR (**Figure S2**).

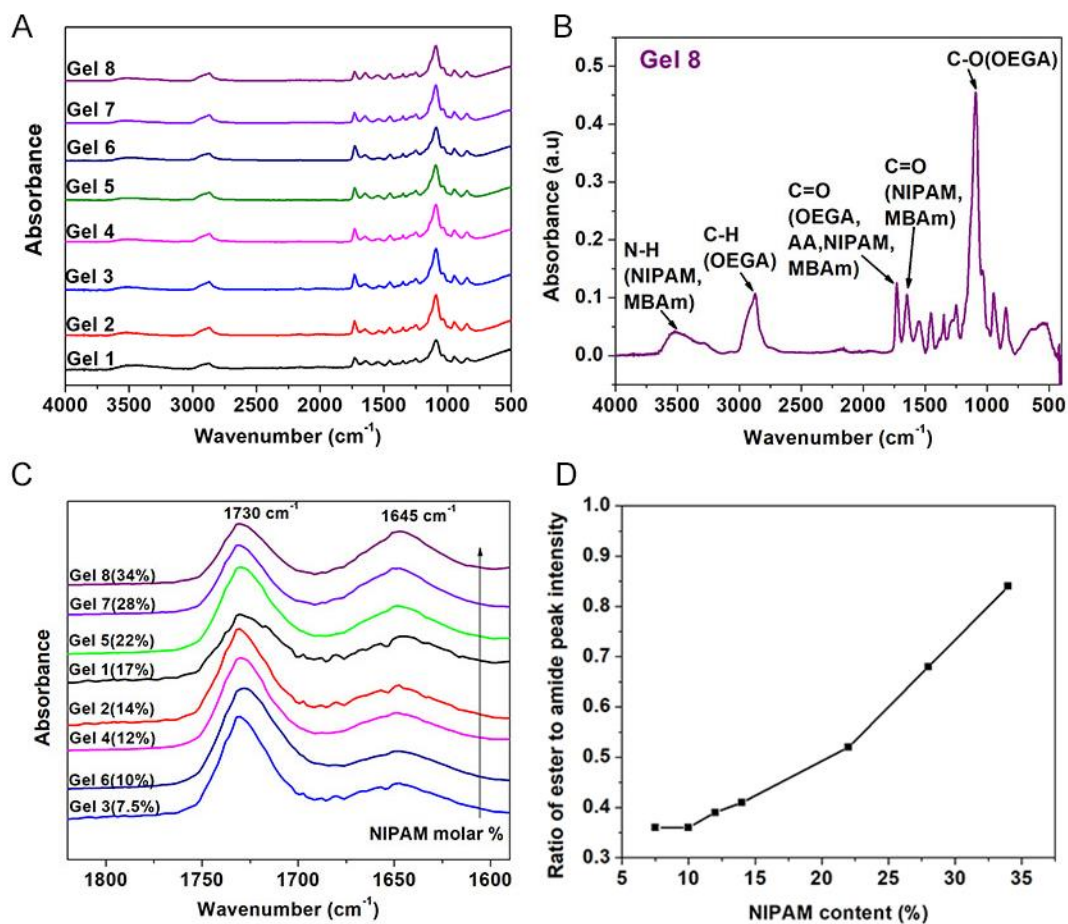


Figure 2: FTIR absorbance spectra of (A) P(OEGA-AA-NIPAM) copolymers of 8 different gel formulations, (B) Gel 8 showing main representative peaks and (C) copolymers of different formulations with zoomed in 1780-1600 cm^{-1} area. (D) Change in intensity of ester C=O stretch to amide C=O stretch peak ratios as a function of NIPAM concentration in the hydrogel formulations.

Thermal properties of P(OEGA-AA-NIPAM) copolymers

Differential scanning calorimetry (DSC) and thermogravimetric analysis (TGA) were used to study the thermal properties of the copolymers based on P(OEGA-AA-NIPAM) and Gel 9 00 (POEGA-co-AA) was added for comparison. DSC curves show different behaviors of the copolymers, but mostly similar behaviors were observed between 25-100 $^{\circ}\text{C}$ (**Figure 3A**). Around 100 $^{\circ}\text{C}$ is the evaporation of water in the copolymers before melting is reached (endothermic

process). The endothermic peaks were observed between 400-450 °C range following exothermic peaks around 350°C for all measured hydrogels (**Figure 3B**). After 350°C, the endothermic process could be an indication of the beginning of melting of some of the monomers.⁴⁴ Gel 6, having the highest percentage of AA of all formulations showed the highest melting point at 430°C (**Figure 3B**) and Gel 7 with the lowest AA molar % at around 405°C. The DSC data suggest that P(OEGA-AA-NIPAM) hydrogel melts between 400-430°C and the melting point is dependent on AA content in the formulation where more AA give a more stable hydrogel because of more hydrogen bonding in the hydrogel network. Interestingly, Gel 5 (34%AA) showed an exception with lower endothermic peak at 410 °C compared to Gel 8 (10% AA), and this can be explained by lower crosslinking density in Gel 5 and same weight ratio of AA and NIPAM content (**Table 1**) that can have other effects on this gel behaviors beside AA. It is also noted that P(OEGA-AA-NIPAM) copolymer is stable at the range of temperature where it is intended to be used (physiological conditions) during wound healing. TGA was performed using a TGA instrument (TA Q50) and TGA curves of P(OEGA-AA-NIPAM) hydrogels of different molar ratios are presented in **Figure 3C**. The peak temperature of water loss was slightly different for each of the hydrogel formulations. The temperature values could be obtained from the first derivative plots of the TGA as 112 °C for Gel 9, 108 °C for Gel3, 115 °C for Gel 8, 130 °C for Gel 900 and 137 °C for GEL 6 (**Figure 3C**). As the concentration of AA increased in copolymers, the water evaporation temperature slightly increased (Gel 6 has more AA than Gel 3 and Gel 8) and its water evaporates at higher temperature than the other two formulations. This is due to more hydrogen bonds in the polymer with higher AA content. Further increase in temperature caused the polymers to decompose between 350–380 °C. The thermal responses of the copolymer is in good agreement with the previous studies on polyvinyl alcohol-copoly (methacrylic acid) hydrogels, suggesting

that the copolymers can serve as better carriers for drug delivery.⁴⁵ It is worthy to mention that the hydrogel with highest NIPAM content (Gel 9, 43% NIPAM) decomposed at lowest temperature at 323 °C with great mass loss (around 14%) compared to when there is no NIPAM in the hydrogel (Gel 900, 0% NIPAM) or less NIPAM (Gel 3, 7.5% NIPAM) (**Figure 3D**). In addition, high NIPAM content resulted in fast water evaporation and highest decomposition rate at later temperature. The behavior of Gel 9 can be explained by the phase separation at the temperature above PNIPAM' LCST where it expels water molecules out from the polymer networks due to dominant hydrophobic interactions between its isopropyl groups.^{17,23, 46} Both DSC and TGA suggest that AA content in the polymer has more effect on thermal response of P(OEGA-AA-NIPAM) hydrogel linking it to its stability of hydrogel at high temperature.

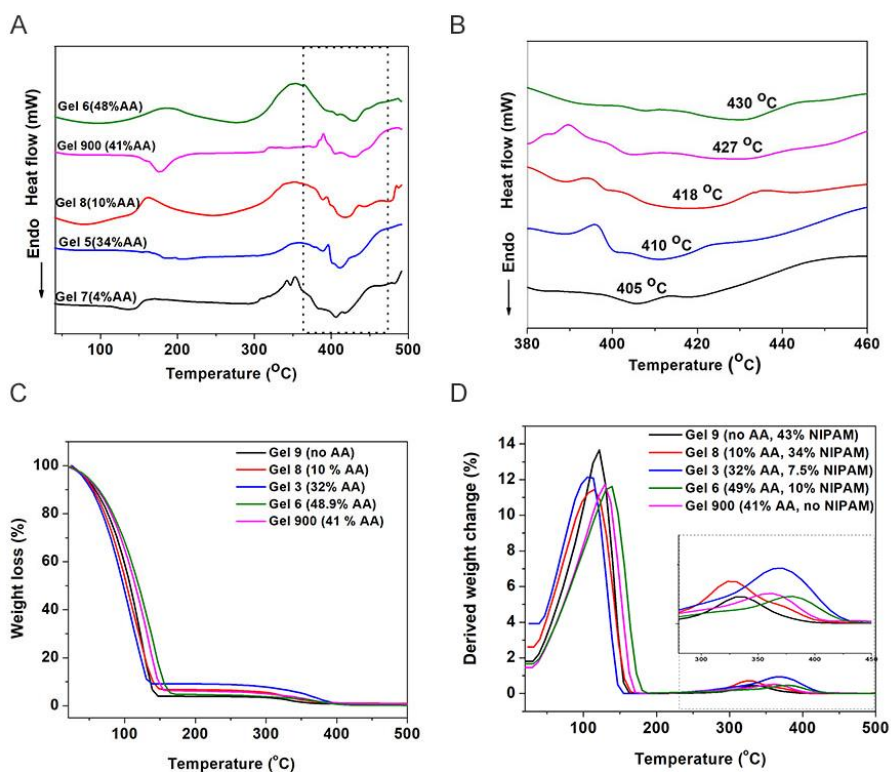


Figure 3: (A) DSC thermograms of the copolymers in the temperature range from 50 to 500 °C with (B) Zoomed in of A for 380-460 °C area. (C) TGA curves of the hydrogel formulations in 0-500 °C temperature range. (D) Derivative plots of TGA curves.

Swelling and degradation studies of P(OEGA-AA-NIPAM) hydrogel

Degradation of P(OEGA-AA-NIPAM) hydrogels were tested in SBF buffer in 40 days. This was to study the capability of hydrogel be degraded by the body in wound healing applications that is intended. In addition, swelling behaviors of hydrogels have been reported to be closely related to its mechanical properties,^{9,47} and hydrogel capacity to retain water in its porous structure is very important to ensure protein/drug encapsulation. Therefore, hydrolytic swelling and degradation of P(OEGA-AA-NIPAM) hydrogels were explored to better understand its mechanical properties. The percent swelling ratio of the hydrogels was calculated by the following equation 1 (N = 4 for each time point) W_d =weight of dry hydrogel and W_s is weight of swollen hydrogel.

$$\text{Swelling ratio} = ((W_s - W_d)/W_d) \times 100 \quad (1)$$

After the swollen hydrogel samples were weighed, lyophilized, and then weighed (W_f) again. The degradation of the hydrogel samples was measured as the percent mass loss of the hydrogel samples, calculated by the following equation 2 (N = 4 for each time point).

$$\text{Weight loss \%} = ((W_d - W_f)/W_d) \times 100 \quad (2)$$

The swelling behaviors of hydrogel showed that it was swollen in the first 28 days up to 950 wt% then we observed deswelling after 40 days to 261 wt% (**Figure 4A**). The decline in swelling ratio at 40 days might be due to water evaporation from hydrogel. The *in vitro* degradation was monitored using weight loss percentage at different time points. The percent weight loss was 60% in 40 days (**Figure 4B**) along with swelling behavior suggests that Gel 8 could be partially degraded making it lose its capacity to take in anymore water at later time points. In addition,

P(OEGA-AA-NIPAM) being a charged hydrogels the electrostatic repulsion between charges dominates the osmotic forces that make the hydrogel swell,⁴³ so the swelling equilibrium is reached after 10 days.

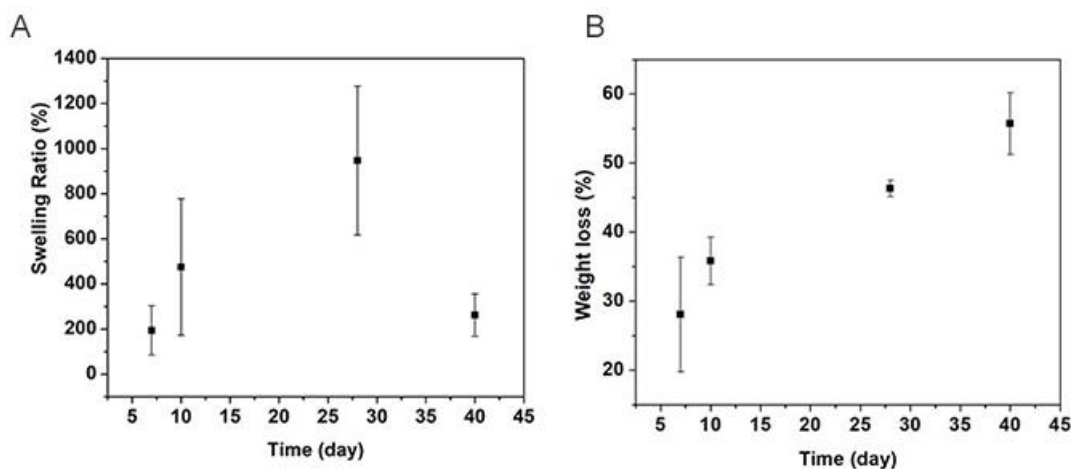


Figure 4: A) Swelling behaviors and B) Hydrolytic degradation of P(OEGA-AA-NIPAM) injectable hydrogel in simulated body fluid (SBF, pH 7.4) measured at 37 °C over 40 days.

Cytotoxicity studies of the P(OEGA-AA-NIPAM) hydrogel

Cytotoxicity studies of the P(OEGA-AA-NIPAM) hydrogel was evaluated at different polymer concentrations (**Table 2**) on human fibroblast cells. MTT assay, a cell proliferation assay to determine cell viability that depends on mitochondrial respiration and access cellular energy capacity was performed.⁴⁸ MTT is converted to insoluble purple formazan that is impermeable to cell membrane, in presence of mitochondrial reductase so the accumulation of formazan can be analyzed to estimate cell viability.⁴⁹ MTT assay de viability data show that the new hydrogel P(OEGA-AA-NIPAM) formulation is not toxic to fibroblast cells at the concentration of 30 wt%. The cell viability to more than 80% (**Figure 5**) and it is comparable to the control (Gel 900) that was previously proven to be biocompatible.¹⁴ It was reported that the viability less than 70% shows the compound (NIPAM) toxic to cells³⁹, and this is not the case for our hydrogel system. Our

hydrogel system contains ~10% polymer according to TGA. Viability was calculated using equation 3.

$$\% \text{ Cell viability} = (I_{\text{sample}}/I_{\text{control}}) \times 100 \quad (3)$$

I_{sample} : Number of viable cells (intensity of formazan) treated with polymer with specific concentration and I_{control} : Number of viable cells with no polymer treatment (control).

Table 2: Experimental details for the cytotoxicity experiment of P(OEGA-AA-NIPAM) hydrogels.

Polymer wt %	Polymer wt by g	Stock gel (μL)	Medium (μL)	Cells (μL)
5	0.005	5	45	50
10	0.011	11	39	50
15	0.017	18	32	50
20	0.025	25	25	50
25	0.033	33	17	50
30	0.042	43	7	50
PBS Media	0	0	50	50

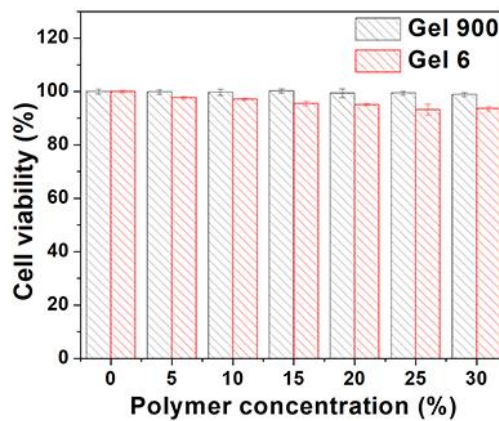


Figure 5: MTT-assay viability data showing polymer concentration effect on cell viability after treatment with Gel 900 (P(OEGA-co-AA)) and Gel 6 P(OEGA-AA-NIPAM).

In vitro controlled release of proteins from P(OEGA-AA-NIPAM) hydrogel

Different formulations of P(OEGA-AA-NIPAM) hydrogel were tested for their capability for controlled and sustained release of human acidic growth factor (hFGF1) in physiological conditions. Released hFGF1 was monitored by fluorescence spectroscopy for at least 10 days. The released amount of hFGF1 was calculated using a calibration curve and cumulative amount was obtained. The order of decreasing release is Gel 1 > Gel 8 > Gel 7 > Gel 6 > Gel 5 > Gel 3 > Gel 4 > Gel 2 (Figure 11). Gel 1 showed the fastest release rate because of lowest POEGA content that provide less room for hydrogel-protein interaction so fast diffusion. More AA Gel 8 has the highest NIPAM concentration (34% NIPAM) while Gel 7 has the highest NIPAM/AA ratio (3rd column of Table 1) and both formulations show close release rate with Gel 8 being slightly higher with 54% and 43% release rate from Gel 8 and Gel 7, respectively (**Figure S3**). As expected, low concentration of NIPAM in the hydrogel such as in Gel 3 (7% NIPAM) showed the lowest release rate because of presence of strong electrostatic interactions between hFGF1 and hydrogel. More NIPAM in the formulation help to space out the negative charges of the injectable hydrogel leading to less interactions between hFGF1 and hydrogel. Comparing the release profiles of hFGF1 from P(OEGA-co-AA) and the current data one can say that incorporating NIPAM in P(OEGA-co-AA) has improved the released profile of hFGF1 by 6 times from less than 7% (**Figure S3**) to 45% (**Figure 6C**) in 5 days in physiological conditions. Moreover, the release profile of hFGF1 can be tuned by changing hydrogel composition, which involved changing molar ratios of monomers.

Based on release profiles of hFGF1 and physical properties from different formulations such as their injectability, Gel 8 was chosen as the best formulation to be used for further application of this hydrogel as shows the best sustained release, and its physical properties are close the properties of commercial Tegaderm and Gel 900 that was studied previously and used in

wound healing applications. There was a significant difference between release at room temperature versus at 37 °C. The release rate was much slower (two times) at 25 °C compared to 37 °C (**Figure 6A and B**). This could be explained by PNIPAM properties where it collapses at temperature higher than its LCST to facilitate release of loaded protein.^{22, 23, 28} The release rate of FGFs proteins from P(OEGA-AA-NIPAM) hydrogel was depended on the type of FGFs being released (**Figures S3A**) and this can be associated with the charge distribution on proteins and hydrogels that can tell how much the interactions are going to happen which also affect the release rate as result. Proliferation assay performed showed that the bioactivity of released hFGF1 was sustained up to 60% after 7 days (**Figure 6B**). The protein activity of released hFGF1 declined overtime because of some denaturation and or aggregations. After P(OEGA-AA-NIPAM) has shown capacity for a sustained release of growth factors related proteins (FGFs) with bioactivity above 60%. It is believed that the sustained release was made possible by strong electrostatic interactions between the anionic hydrogel and positively charged proteins in physiological conditions. These interactions are thought to stabilize the proteins in the hydrogel network to maintain their biological activity over a period of at least ten days before it starts getting inactive.

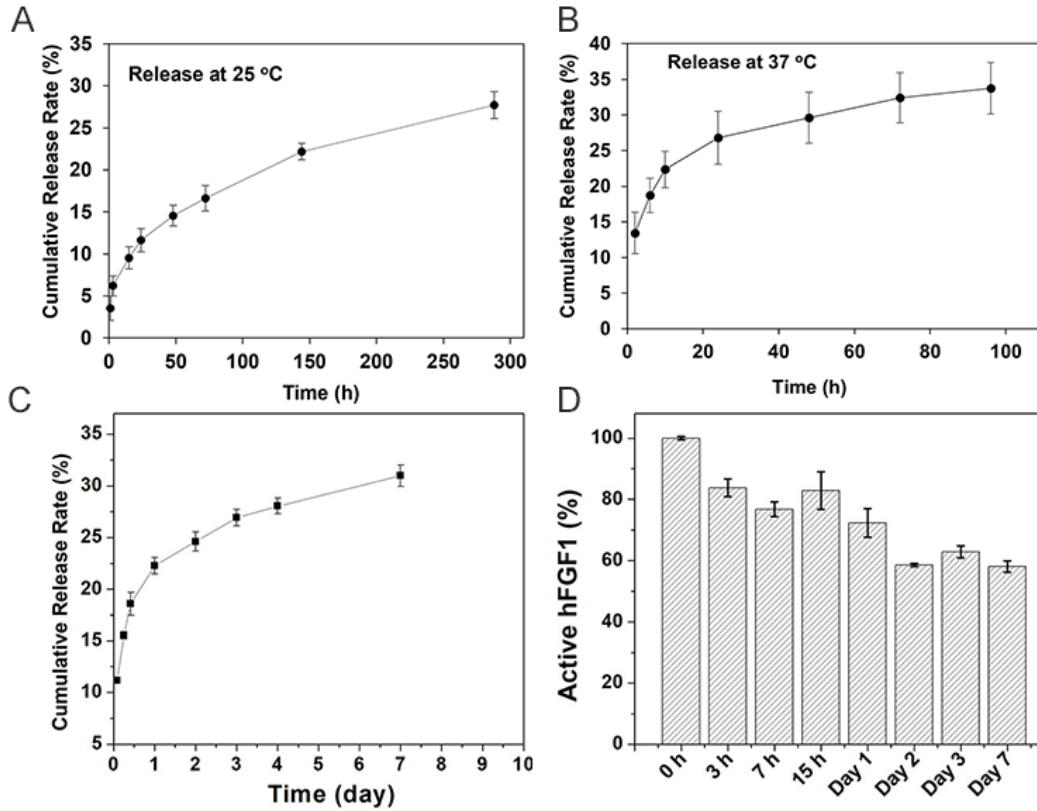


Figure 6: hFGF1 release profile as a function of time from Gel 8 using fluorescence spectroscopy ($\lambda_{exc}=308$ nm) in the range of 300-400 nm (A) at 25 °C and (B) at 37 °C. (C) Controlled release of hFGF1 from Gel 8 for 7 days in physiological conditions. (D) Bioactivity of released hFGF1 from (C). Each data was measured in triplicate (n=3). Error bars represent standard deviation.

As a control, a negatively charged model protein, BSA (pI=5.4) was loaded in P(OEGA-AA-NIPAM) injectable and incubated into PBS at 37 °C for 5 days. The released BSA was quantified by fluorescence spectroscopy at $\lambda_{exc}=295$ nm and cumulative release amount was calculated using a developed calibration curve. BSA is a negatively charged protein in physiological conditions (pI=4.5-5.0). BSA was used as a control to see if the anionic hydrogel system can be released in same physiological conditions as previously release FGFs proteins. The cumulative data shows burst release of BSA in the first few hours in the media where 50% of the loaded BSA was released in 1 day. The burst release is explained by the repulsive forces between

similarly charged BSA that led to hydrogel did not hold the protein in its network. The rest of the protein (90%) was released in 5 days with slow release (**Figure S3B**). This proved that the electrostatic interactions between the hydrogel system and positively charged proteins are important of controlled and sustained release observed.

In vivo study

In vivo study was conducted to evaluate the controlled release of hFGF1 from P(OEGA-AA-NIPAM) hydrogel on wound healing. Sterile hydrogels were used to load hFGF1 in the final concentration of 3 mg/mL. Borax (0.1 w/v%) was used as antiseptic in the PBS for in vivo experiment. Each of the mice received two excisional wounds of 6 mm on their back. Wounds were treated with Gel 8 loaded with hFGF1 and just Gel 8 as a control. Wound sizes for days 1, 3, 5, 7, and 10 after wounding were computed in relation to the original wound size. Wound closure data showed that FGF1 treatment significantly diminished the average wound size ($p = 0.0047$) over the whole data set (**Figure 7**). The FGF1-treated wounds were significantly smaller than the untreated control group on days 3 ($p = 0.0297$) and 5 ($p = 0.015$), which indicate that the effects of FGF1 were most obvious during the intermediate time points during the proliferative phases of healing (**Figure 7**). This study confirmed the sustained release of hFGF1 during the entire wound healing process studied over a period of 10 data. In addition, the significant difference in wound closure is an indication of preserved bioactivity of released hFGF1 that we observed *in vitro*. The hydrogel was able to prolong the therapeutic effect of loaded hFGF1 to enhance wound healing process compared to control.

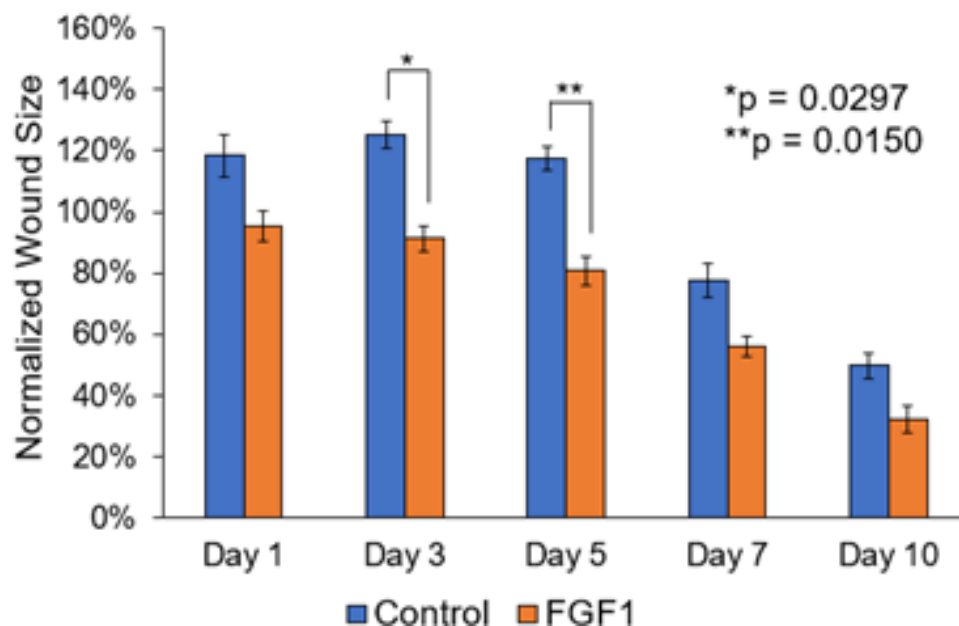


Figure 7: In vivo study showing normalized wound sizes for wound treated with just gel 8 (blue) as a control and Gel 8 loaded with hFGF1 (Orange) across the study for 10 days.

2.5 Conclusions

In this chapter, an injectable anionic biocompatible hydrogel system based on P(OEGA-AA-NIPAM) was prepared using a simple radical polymerization reaction. AA was added to the hydrogel to introduce negative charges in the hydrogel and NIPAM was used to space out the negative charges within the copolymer to control the release rate of positively charged proteins. Different formulations of the hydrogels were prepared by tuning the molar ratios of the three monomers to evaluate the effect of the monomers on different properties of the hydrogel and its capability for controlled release of positively charged proteins. Spectroscopic methods were used to chemical structure analysis and proved incorporation of all the monomers in the hydrogel. The thermal stability studies revealed that increasing the concentration of AA or decreasing concentration of NIPAM in the hydrogel increases their thermal stability as result of increased

hydrogen bonding in the hydrogel. Biocompatibility of the hydrogel was confirmed by cytotoxicity assay of the copolymer on fibroblast cells.

In addition, copolymers with high NIPAM content faster rate of water evaporation and greater weight loss which can be explained by phase change of PNIPAM upon change in temperature. P(OEGA-AA-NIPAM) hydrogel showed the capacity for a sustained release of hFGF1 with preserved bioactivity in physiological conditions. The sustained release was based on electrostatic interactions that hold the proteins in hydrogel and sustain its bioactivity overtime. Incorporating NIPAM in P(OEGA-AA) hydrogel enhanced release rate of hFGF1 by six folds. The enhanced controlled release rate is associated with more dispersed charge distribution because of NIPAM. PNIPAM thermo-responsive properties also enhanced release profile at 37 °C compared to 25 °C because of change in hydrogel structure can repel loaded protein upon increase in temperature above PNIPAM's LCST. As a control, BSA's controlled release showed much faster burst release from P(OEGA-AA-NIPAM) hydrogel because of charge repulsion between BSA's negative net charge and similarly charged hydrogel, thus faster release rate. This emphasized on the importance of electrostatic interactions on a sustained release of the proteins. Lastly, in vivo studies revealed enhanced wound closure when treated with P(OEGA-AA-NIPAM) hydrogel loaded with hFGF1 compared to control. Preserved bioactivity of FGF1 was key to its obvious effect on wound healing especially during proliferation phase. The results obtained from this study suggest that FGF1 remain active after encapsulation, that the rate of sustained delivery of FGFs can be tuned during hydrogel synthesis, and that this hydrogel can be used as a potential delivery vehicle for positively charged proteins like FGFs in wound healing applications.

2.6. References

1. E. M. Ahmed, *Journal of Advanced Research* **2015**, *6*, 105-121 10.1016/j.jare.2013.07.006.
2. M. B. Thurmer, C. E. Diehl, F. J. B. Brum, L. A. dos Santos, *Materials Research-Ibero-American Journal of Materials* **2014**, *17*, 109-113 10.1590/1516-1439.223613.
3. S. Atta, S. Khaliq, A. Islam, I. Javeria, T. Jamil, M. M. Athar, M. I. Shafiq, A. Ghaffar, *International Journal of Biological Macromolecules* **2015**, *80*, 240-245 10.1016/j.ijbiomac.2015.06.044.
4. P. Bertsch, L. Schneider, G. Bovone, M. W. Tibbitt, P. Fischer, S. Gstohl, *Acs Applied Materials & Interfaces* **2019**, *11*, 38578-38585 10.1021/acsami.9b15896.
5. E. Bakaic, N. M. B. Smeets, M. Badv, M. Dodd, O. Barrigar, E. Siebers, M. Lawlor, H. Sheardown, T. Hoare, *Acs Biomaterials Science & Engineering* **2018**, *4*, 3713-3725 10.1021/acsbiomaterials.7b00397.
6. L. R. Boles, J. D. Bumgardner, T. Fujiwara, W. O. Haggard, F. D. Guerra, J. A. Jennings, *International Journal of Biological Macromolecules* **2019**, *133*, 372-381 10.1016/j.ijbiomac.2019.04.075.
7. A. Dabbaghi, A. Ramazani, N. Farshchi, A. Rezaei, A. Bodaghi, S. Rezayati, *Journal of Industrial and Engineering Chemistry* **2021**, *101*, 307-323 10.1016/j.jiec.2021.05.051.
8. A. P. Mathew, S. Uthaman, K. H. Cho, C. S. Cho, I. K. Park, *International Journal of Biological Macromolecules* **2018**, *110*, 17-29 10.1016/j.ijbiomac.2017.11.113.
9. J. Qu, X. Zhao, Y. P. Liang, Y. M. Xu, P. X. Ma, B. L. Guo, *Chemical Engineering Journal* **2019**, *362*, 548-560 10.1016/j.cej.2019.01.028.
10. Y. P. Fu, Y. Ding, L. T. Zhang, Y. M. Zhang, J. Liu, P. Yu, *European Journal of Medicinal Chemistry* **2021**, *217*, 21 10.1016/j.ejmech.2021.113372.
11. C. C. Lin, K. S. Anseth, *Pharm Res* **2009**, *26*, 631-43 10.1007/s11095-008-9801-2.
12. B. Ozcelik, K. K. K. Ho, V. Glattauer, M. Willcox, N. Kumar, H. Thissen, *Acs Biomaterials Science & Engineering* **2017**, *3*, 78-87
13. P. Krsko, M. Libera, *Materials Today* **2005**, *8*, 36-44
14. A. Berdichevski, Y. Shachaf, R. Wechsler, D. Seliktar, *Biomaterials* **2015**, *42*, 1-10 10.1016/j.biomaterials.2014.11.015.
15. N. A. Peppas, K. B. Keys, M. Torres-Lugo, A. M. Lowman, *Journal of Controlled Release* **1999**, *62*, 81-87

16. S. Selvam, M. V. Pithapuram, S. P. Victor, J. Muthu, *Colloids and Surfaces B-Biointerfaces* **2015**, *126*, 35-43 10.1016/j.colsurfb.2014.11.043.
17. S. P. Zustiak, J. B. Leach, *Biomacromolecules* **2010**, *11*, 1348-1357 10.1021/bm100137q.
18. Y. Wu, J. Liang, F. Horkay, M. Libera, *Journal of Polymer Science Part B: Polymer Physics* **2016**, *54*, 64-72
19. D. Myung, W. Koh, A. Bakri, F. Zhang, A. Marshall, J. Ko, J. Noolandi, M. Carrasco, J. R. Cochran, C. W. Frank, C. N. Ta, *Biomedical Microdevices* **2007**, *9*, 911-922 10.1007/s10544-006-9040-4.
20. M. K. Nguyen, D. S. Lee, *Macromolecular Research* **2010**, *18*, 284-288 10.1007/s13233-010-0315-5.
21. D. J. Waters, K. Engberg, R. Parke-Houben, C. N. Ta, A. J. Jackson, M. F. Toney, C. W. Frank, *Macromolecules* **2011**, *44*, 5776-5787 10.1021/ma200693e.
22. D. Myung, W. Koh, J. Ko, Y. Hu, M. Carrasco, J. Noolandi, C. N. Ta, C. W. Frank, *Polymer* **2007**, *48*, 5376-5387
23. Y. M. Mohan, P. S. K. Murthy, J. Sreeramulu, K. M. Raju, *Journal of Applied Polymer Science* **2005**, *98*, 302-314
24. D. Myung, D. Waters, M. Wiseman, P.-E. Duhamel, J. Noolandi, C. N. Ta, C. W. Frank, *Polymers for Advanced Technologies* **2008**, *19*, 647-657
25. W. Tanan, J. Panichpakdee, S. Saengsuwan, *European Polymer Journal* **2019**, *112*, 678-687
26. T. Wang, J. D. Jones, I. I. Niyonshuti, S. Agrawal, R. K. Gundampati, T. K. S. Kumar, K. P. Quinn, J. Chen, *Advanced Therapeutics* **2019**, *2*,
27. R. A. Scott, N. A. Peppas, *Macromolecules* **1999**, *32*, 6149-6158
28. G. M. Fan, Q. Han, X. Q. Xiong, *Progress in Chemistry* **2014**, *26*, 1223-1232
29. M. A. Haq, Y. L. Su, D. J. Wang, *Materials Science & Engineering C-Materials for Biological Applications* **2017**, *70*, 842-855
30. S.Ohya, S. Kidoaki, T. Matsuda, *Biomaterials* **2005**, *26*, 3105-11 10.1016/j.biomaterials.2004.08.006.
31. D. S. Jones, C. P. Lorimer, C. P. McCoy, S. P. Gorman, *J Biomed Mater Res B Appl Biomater* **2008**, *85*, 417-26 10.1002/jbm.b.30960.

32. Y. Okuyama, R. Yoshida, K. Sakai, T. Okano, Y. Sakurai, *J Biomater Sci Polym Ed* **1993**, *4*, 545-56 10.1163/156856293x00195.
33. Y. Okuyama, R. Yoshida, K. Sakai, T. Okano, Y. Sakurai, *Journal of Biomaterials Science, Polymer Edition* **1993**, *4*, 545-556 10.1163/156856293X00195.
34. S. Salmaso, A. Sernenzato, S. Bersani, P. Matricardi, F. Rossi, P. Caliceti, *International Journal of Pharmaceutics* **2007**, *345*, 42-50 10.1016/j.ijpharm.2007.05.035.
35. A. K. Bajpai, S. K. Shukla, S. Bhanu, S. Kankane, *Progress in Polymer Science* **2008**, *33*, 1088-1118
36. K. Huang, H. Y. Wu, F. Jiang, G. Z. Shen, L. Wang, *Polymer Degradation and Stability* **2018**, *156*, 228-233 10.1016/j.polymdegradstab.2018.09.009.
37. K. H. Son, J. W. Lee, *Materials* **2016**, *9*, 13 10.3390/ma9100854.
38. D. Schmaljohann, *Advanced Drug Delivery Reviews* **2006**, *58*, 1655-1670
39. A. Serres, M. Baudyš, S. W. Kim, *Pharmaceutical Research* **1996**, *13*, 196-201 10.1023/A:1016026711364.
40. C. Ramkissoon-Ganorkar, F. Liu, M. Baudys, S. W. Kim, *J Biomater Sci Polym Ed* **1999**, *10*, 1149-61 10.1163/156856299x00739.
41. J. Akimoto, M. Nakayama, K. Sakai, T. Okano, *Biomacromolecules* **2009**, *10*, 1331-1336 10.1021/bm900032r.
42. R. Raju, S. Bandyopadhyay, A. Sharma, S. V. Gonzalez, P. H. Carlsen, O. R. Gautun, W. R. Glomm, *Polymers* **2018**, *10*, 14 10.3390/polym10030309.
43. X.-Z. Zhang, R.-X. Zhuo, *European Polymer Journal* **2000**, *36*, 2301-2303
44. F. Rizzo, N. S. Kehr, *Advanced Healthcare Materials* **2021**, *10*, 26 10.1002/adhm.202001341.
45. L.-W. Xia, R. Xie, X.-J. Ju, W. Wang, Q. Chen, L.-Y. Chu, *Nature Communications* **2013**, *4*, 2226 10.1038/ncomms3226.
46. S. B. Lee, E. K. Park, Y. M. Lim, S. K. Cho, S. Y. Kim, Y. M. Lee, Y. C. Nho, *Journal of Applied Polymer Science* **2006**, *100*, 4439-4446
47. J. Djonlagić, Z. S. Petrović, *Journal of Polymer Science Part B: Polymer Physics* **2004**, *42*, 3987-3999

48. Z. Li, J. Shen, H. Ma, X. Lu, M. Shi, N. Li, M. Ye, *Mater Sci Eng C Mater Biol Appl* **2013**, *33*, 1951-7 10.1016/j.msec.2013.01.004.
49. A. Okada, A. Usuki, *Macromolecular Materials and Engineering* **2006**, *291*, 1449-1476
50. K. Haraguchi, T. Takehisa, *Advanced Materials* **2002**, *14*, 1120-1124
51. K. Ito, *Polymer Journal* **2007**, *39*, 489-499 10.1295/polymj.PJ2006239.
52. R. Narayanaswamy, V. P. Torchilin, *Molecules* **2019**, *24*, 18 10.3390/molecules24030603.
53. L. L. Wang, J. J. Chung, E. C. Li, S. Uman, P. Atluri, J. A. Burdick, *Journal of Controlled Release* **2018**, *285*, 152-161 10.1016/j.jconrel.2018.07.004.
54. F. Ganji, E. Vasheghani-Farahani, *Iranian Polymer Journal* **2009**, *18*, 63-88.
55. Q. M. Nunes, Y. Li, C. Sun, T. K. Kinnunen, D. G. Fernig, *PeerJ* **2016**, *4*, e1535-e1535 10.7717/peerj.1535.
56. E. Tassi, K. McDonnell, K. A. Gibby, J. U. Tilan, S. E. Kim, D. P. Kodack, M. O. Schmidt, G. M. Sharif, C. S. Wilcox, W. J. Welch, G. I. Gallicano, M. D. Johnson, A. T. Riegel, A. Wellstein, *The American Journal of Pathology* **2011**, *179*, 2220-2232
57. S. Ashraf, H.-K. Park, H. Park, S.-H. Lee, *Macromolecular Research* **2016**, *24*, 297-304 10.1007/s13233-016-4052-2.
58. M. A. Cooperstein, H. E. Canavan, *Biointerphases* **2013**, *8*, 12 10.1186/1559-4106-8-19.
59. J. M. Yang, S. J. Yang, H. T. Lin, T. H. Wu, H. J. Chen, *Materials Science & Engineering C- Biomimetic and Supramolecular Systems* **2008**, *28*, 150-156 10.1016/j.msec.2007.01.011.
60. J. D. Jones, H. E. Ramser, A. E. Woessner, A. Veves, K. P. Quinn, *Advances in wound care* **2020**, *9*, 90-102 10.1089/wound.2019.1030.
61. A. W. Martinez, J. M. Caves, S. Ravi, W. Li, E. L. Chaikof, *Acta Biomaterialia* **2014**, *10*, 26-33
62. J. Ostroha, M. Pong, A. Lowman, N. Dan, *Biomaterials* **2004**, *25*, 4345-53
63. D. S. Achilias, I. S. Tsagkalias, *Journal of Thermal Analysis and Calorimetry* **2018**, *134*, 1307-1315
64. M. U. Minhas, M. Ahmad, L. Ali, M. Sohail, *Daru-Journal of Pharmaceutical Sciences* **2013**, *21*, 9

65. S. Shekhar, M. Mukherjee, A. K. Sen, *Polymer Bulletin* **2016**, *73*, 125-145 10.1007/s00289-015-1476-3.

66. K. Y. Lee, K. H. Bouhadir, D. J. Mooney, *Biomaterials* **2004**, *25*, 2461-2466
10.1016/j.biomaterials.2003.09.030.

67. M. Suneetha, K. M. Rao, S. S. Han, *Acs Omega* **2019**, *4*, 12647-12656
10.1021/acsomega.9b01302.

2.7. Appendix A: Supplemental information

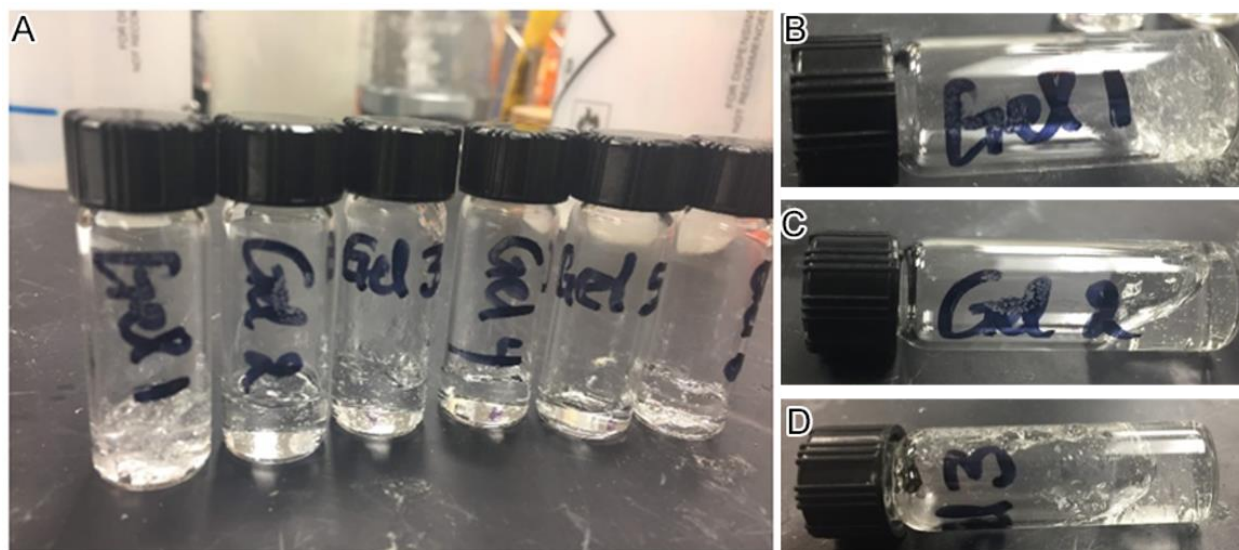


Figure S1: Photograph of injectable hydrogels with different formulations. (A) from left to right: Gel 1 to Gel 6. (B) Gel 1 (C) Gel 2 and (D) Gel 3.

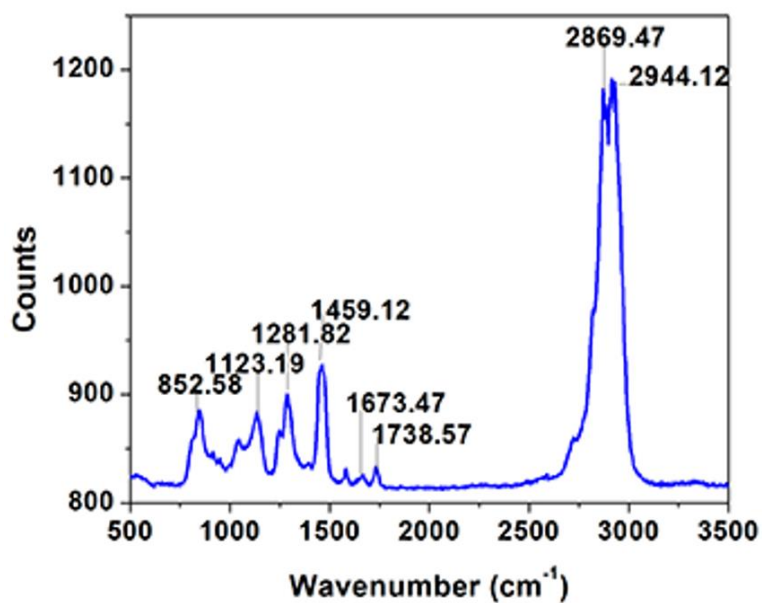


Figure S2: Raman spectrum of P(OEGA-AA-NIPAM) injectable hydrogel, Gel 8.

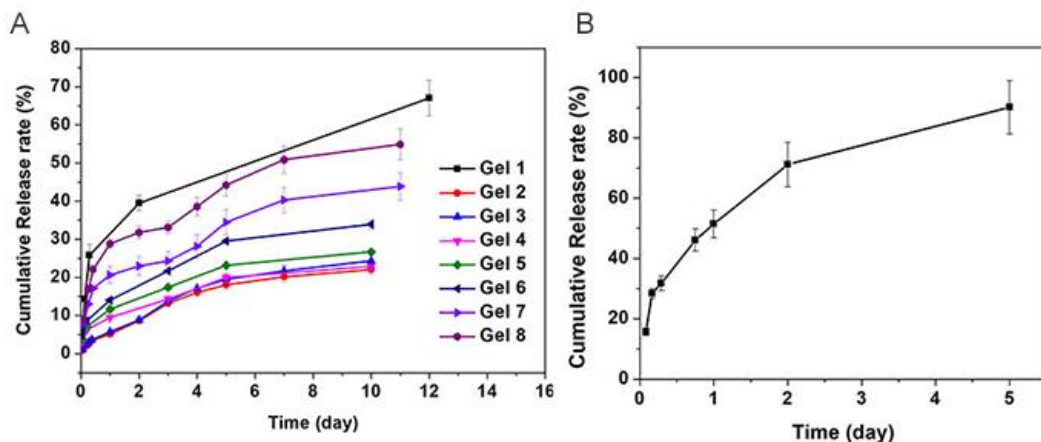


Figure S3: (A) Release profile of hFGF1 from different formulations of P(OEGA-AA-NIPAM) hydrogels at 37 °C at pH=7.4. (B) BSA release profile from Gel 8 as a function of time. Fluorescence spectra were recorded at λ_{exc} of 280 nm and 295 nm for hFGF1 and BSA, respectively. Each data was measured in triplicate (n=3). Error bars represent standard deviation.

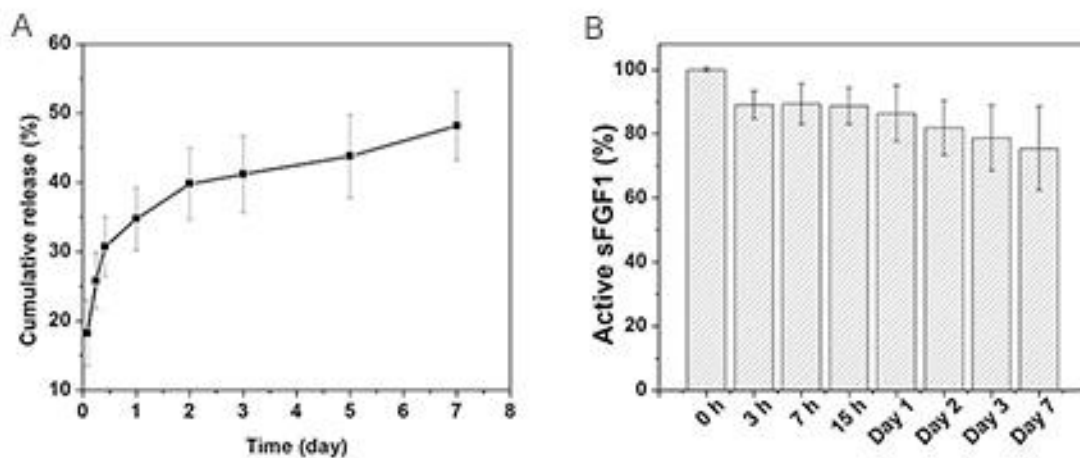


Figure S4: Release profiles of sFGF from Gel 8 in physiological conditions. (A) Fluorescence spectra of sFGF released from Gel8. (B) Bioactivity of released sFGF1 from (A). Data are presented as means (N=3). Error bars represent standard deviation.

Table S1: Hydrodynamic diameter and Zeta Potential of POEGA-based hydrogels.

Hydrogel formulation	Zeta potential (mV)	Hydrodynamic diameter (nm)
P(OEGA-co-AA)	-6.44±0.89	122.6
P(OEGA-AA-NIPAM)	-2.37±0.26	136.7

2.8. Appendix B: Controlled release of positively charged proteins from injectable

P(OEGA-*co*-AA) hydrogel*

*Published: Wang, T.; Jones, J.D.; Niyonshuti, I.I.; Agrawal, S.; Gundampati, R.K.; Kumar, T.K.S.; Quinn, K.P.; Chen, J. Biocompatible, Injectable Anionic Hydrogels based on Poly (oligo ethylene glycol monoacrylate-*co*-acrylic acid) for Protein Delivery, *Advanced Therapeutics* **2019**.

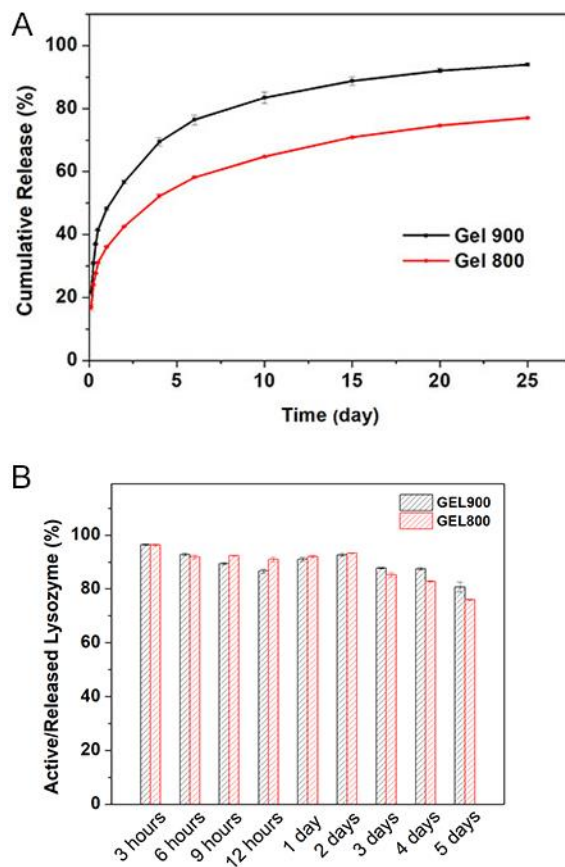


Figure S5: Controlled-release of lysozyme from P (OEGA-*co*-AA) injectable anionic hydrogel. **A.** fluorescence spectrophotometry data of released lysozyme calculated using a standard calibration curve of lysozyme. **B.** Lysozyme activity as a function of time for Gel 900 and Gel 800. Each data point was measured in triplicate (n=3). Error bars represent standard deviation.

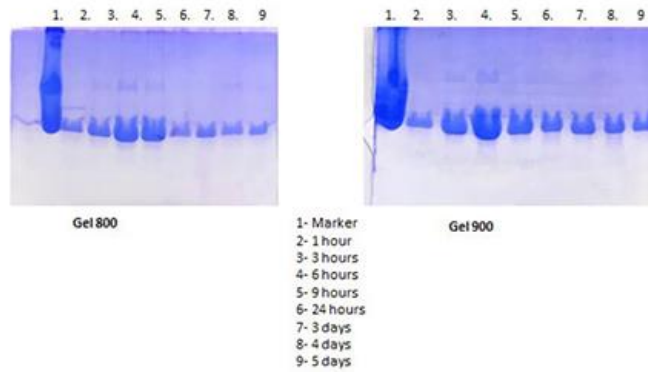


Figure S6: SDS-PAGE of released lysozyme from injectable P(OEGA-*co*-AA) hydrogel, Gel 800 and Gel 900.

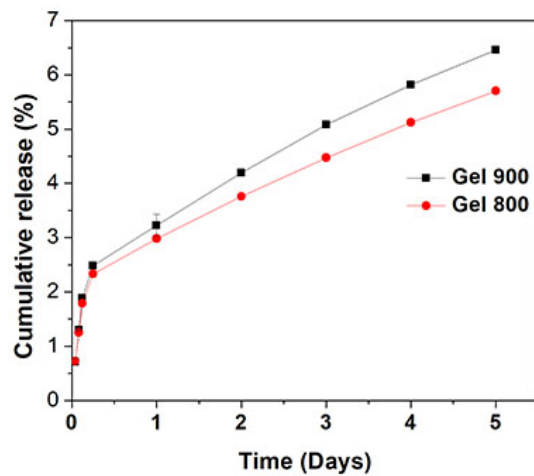


Figure S7: Controlled-release of hFGF1 from P(OEGA-*co*-AA) injectable anionic hydrogel in physiological conditions. Each data point was measured in triplicate (n=3). Error bars represent standard deviation.

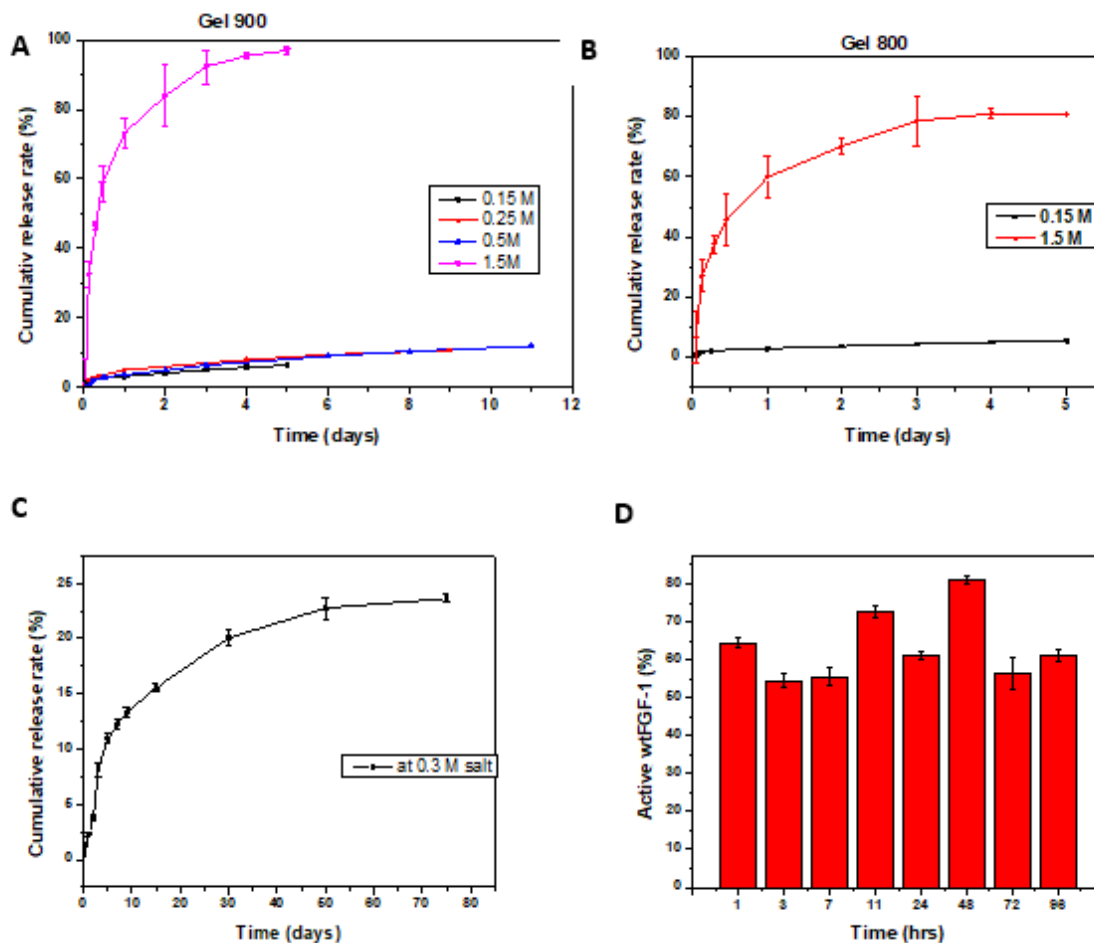


Figure S8: A) Release profile of hFGF1 from Gel 800 and B) from Gel 900 at different salt concentrations obtained using fluorescence spectroscopy. C) Fluorescence data for hFGF1 released from Gel 900 in 0.3M NaCl. D) hFGF1 activity as a function of time of release from Gel 900 for C). Data are presented as means (N=3).

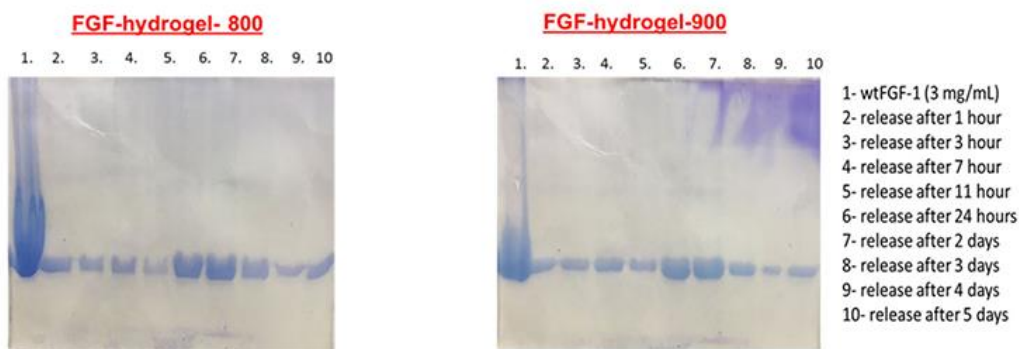


Figure S9: SDS-PAGE of hFGF1 released from P(OEGA-co-AA), Gel 800 and Gel 900 injectable hydrogels at different time points.

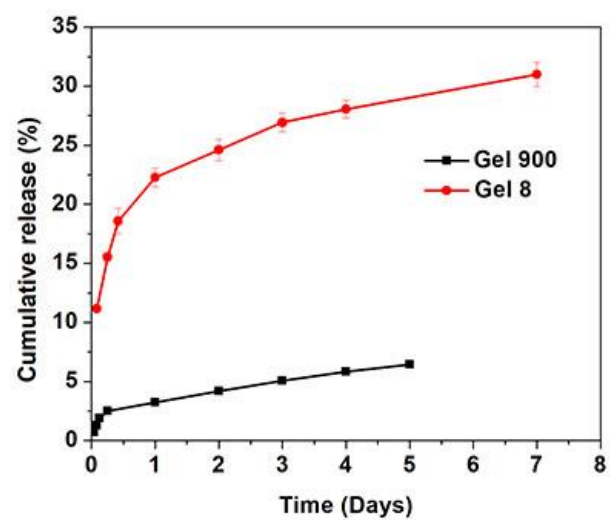


Figure S10: Release profiles of hFGF1 from Gel 900 and Gel 8 obtained using fluorescence spectroscopy in physiological conditions. Each data was measured in triplicate (n=3). Error bars represent standard deviation.

Chapter III. Polydopamine Surface Coating Synergizes the Antimicrobial Activity of Silver Nanoparticles*

3.1. Abstract

Metal nanoparticles, especially silver nanoparticles (AgNPs), have drawn increasing attention for antimicrobial applications. Most studies have emphasized on the correlations between the antibacterial potency of AgNPs and the kinetics of metallic to ionic Ag conversion, while other antimicrobial mechanisms have been underestimated. In this work, we focused on the surface effects of polydopamine (PDA) coating on the antimicrobial activity of AgNPs. A method of fast deposition of PDA was used to synthesize the PDA-AgNPs with controllable coating thickness ranging from 3 to 25 nm. The antimicrobial activities of the PDA-AgNPs were analyzed by fluorescence-based growth curve assays on *Escherichia coli*. The results indicated that the PDA-AgNPs exhibited significantly higher antibacterial activities than poly(vinylpyrrolidone)-passivated AgNPs (PVP-AgNPs) and PDA themselves. It was found that the PDA coating synergized with the AgNPs to prominently enhance the potency of the PDA-AgNPs against bacteria. The analysis of X-ray photoelectron spectroscopy and Fourier transform infrared spectroscopy elucidated that the synergistic effects could be originated from the interaction/coordination between Ag and catechol group on the PDA coating. The synergistic effects led to increased generation of reactive oxygen species and the consequent bacterial damage. These findings demonstrated the importance of the surface effects on the antimicrobial properties of AgNPs. The underlying molecular mechanisms have shined light on the future development of more potent metal nanoparticle-based antimicrobial agents.

***Published:** Niyonshuti, I. I.; Krishnamurthi, V. R.; Okyere, D.; Song, L.; Benamara, M.; Tong, X.; Wang, Y.; Chen, J. Polydopamine Surface Coating Synergizes the Antimicrobial Activity of Silver Nanoparticles. *ACS Appl. Mater. Interfaces* **2020**, 12 (36), 40067–40077

3.2. Introduction

Silver (Ag) has been extensively used as a therapeutic agent in medicine back in ancient history, especially for bacterial infections, much earlier than the clinical introduction of antibiotics in the 1940s and even earlier than the observation of microorganisms during the late 1700s.¹ Different forms of metallic Ag and Ag compounds including solutions, foils, vessels, and colloids have been demonstrated to be beneficial in various scenarios from preventing microbial growth in water to combating bacterial infections in surgery. Despite the risk of argyria particularly due to chronic Ag exposure,²⁻⁴ metallic Ag and Ag compounds continue to be widely used in medical devices and health-care products in the modern era because the benefit of their antimicrobial effects predominates over the non-life-threatening risk.^{1, 5, 6} Colloidal Ag nanoparticles (AgNPs) are of particular interest as an active disinfectant that has been incorporated into various matrixes for potential use in different applications.⁷⁻¹⁰ For example, the incorporation of AgNPs in different textile materials brings to the fabrics not only antimicrobial functions but also beautiful colors due to the optical properties of AgNPs.^{8, 11} Embedding AgNPs to the wound dressing can disinfect the wound site and promote tissue repair.^{9, 12, 13} AgNPs are more active against microbes compared to Ag⁺ due to nanoparticle interactions with membrane, protein, and DNA of microorganisms that lead to their exceptional toxicity to the bacterial cells.¹⁴ The size, shape, and surface ligand of AgNPs can influence the antimicrobial activity of the AgNPs,^{15, 16} and therefore, it is possible to design AgNPs with enhanced antimicrobial properties against infections. Previous studies have mainly emphasized the effects of size, shape, and surface ligand on the antimicrobial activity of AgNPs from the oxidation point of view and correlated their antimicrobial activity with the

kinetics of $\text{Ag}(0) \rightarrow \text{Ag}(\text{I})$ oxidation or $\text{Ag}(\text{I})$ ion release.¹⁷⁻²⁰ However, other mechanisms of AgNPs such as the generation of reactive oxygen species and the disruption of the biomolecular functions also play significant roles in the antimicrobial actions.^{14, 15, 21} Some studies showed that nanoparticles with positively charged surfaces were strong antimicrobial agents.²²⁻²⁴ In this case, the bacterial response of AgNPs could undergo different pathways highly dependent on their surface characteristics that highlighted the difference in toxicity mechanisms of AgNPs from that of ionic Ag.²² More recently, we have directly observed that AgNPs increased the fraction of histone-like nucleoid structuring (H-NS) proteins that form clusters and were able to attach to the bacterial cell membrane and undergo a Brownian diffusion.²⁵ The surfaces of AgNPs passivated by poly(vinylpyrrolidone) (PVP-AgNPs) versus polyethyleneimine (PEI-AgNPs) exhibited different reorganization rates of H-NS proteins. The faster kinetics of H-NS reorganization for PEI-AgNPs appears to be one plausible mechanism responsible for the previously reported higher antimicrobial activity of PEI-AgNPs compared to that of PVP-AgNPs.²²

In this work, we expanded our investigation to the effects of polydopamine (PDA) surface coating on the antimicrobial activity of AgNPs to further our understanding of the role of nanoparticle surface. We chose PDA as the surface coating due to its strong adhesive properties, rich chemical functionalities, and biocompatibility suited for biological applications.^{26, 27} Numerous reports have shown that deposition/incorporation of AgNPs onto PDA coating could introduce antibacterial properties to the coating on different substrates;²⁸⁻⁵⁴ however, it is unclear whether a PDA surface can synergize the antimicrobial activity of AgNPs and the mechanisms. This study systematically investigated the effects of the degree of dopamine self-polymerization on their antimicrobial activity and correlated them with the physicochemical properties of functionalized AgNPs. The different degree of self-polymerization dopamine was controlled using

our previously established method through the PDA coating time.⁵⁵ The morphology and surface properties of the PDA-coated AgNPs (PDA-AgNPs) were characterized by transmission electron microscopy (TEM), ultraviolet–visible (UV–vis) spectroscopy, X-ray photoelectron spectroscopy (XPS), and Fourier transform infrared spectroscopy (FTIR). The antimicrobial activity was evaluated by the bacterial growth curves obtained from our newly developed method based on fluorescence/optical density assays using a microplate reader.⁵⁶ The related biological responses were studied by fluorescence imaging. We observed synergistic effects between the PDA coating and AgNPs and correlated them with the chemical and biological properties of the PDA-AgNPs to provide a better understanding of nanoparticle surface effects on the antimicrobial activity of AgNPs.

3.3. Experimental Methods

Chemicals and Materials. Silver trifluoroacetate (AgTFA), sodium hydrogen sulfide (NaHS), hydrochloric acid (HCl, 99.999%), and nitric acid (HNO₃, 99.999%) were purchased from Alfa Aesar. Poly(vinylpyrrolidone) (PVP, MW = 55 000), Tris-(hydroxymethyl) aminomethane (Trizma base, >99.0%), and dopamine hydrochloride (DA, 99%) were purchased from Sigma-Aldrich. Ethylene glycol (EG) was purchased from J. T. Baker. Acetone was purchased from EMD. Unless specified, chemicals were used as received and experiments were performed using 18 MΩ H₂O.

3.3.1 Synthesis of PVP-AgNPs

PVP-AgNPs were synthesized by the polyol method.⁵⁷ Briefly, 50 mL EG was added to a 250 mL round bottom flask equipped with a stirring bar and placed in an oil bath at 150 °C. After the temperature equilibrated (30–45 min), EG solutions of 0.6 mL of 3 mM NaHS, 5 mL of 3 mM HCl, 12.5 mL of 0.25 g PVP, and 4 mL of 282 mM AgTFA were sequentially added to the reaction

flask. The reaction proceeded for an additional 75 min. The product was collected by adding acetone to the reaction solution at a ratio of 5:1 and centrifuging at 6000 rpm for 10 min. The resulting pellet was purified twice with H₂O, collected by centrifugation at 14 000 rpm for 10 min, and resuspended in H₂O for future use.

3.3.2. Synthesis of PDA-coated Ag Nanoparticles (PDA-AgNPs).

PDA-AgNPs were prepared through self-polymerization of DA on the surface of AgNPs under basic conditions exposed to atmosphere.⁵⁵ The reaction was carried out in a 400 mL beaker with a disperser (IKA T 18 digital ULTRA-TURRAX) equipped with a dispersing element (IKA S 18 N-10 G). Initially, 200 mL of water was heated to 50 °C while dispersed at a speed of 2800 rpm. Trizma base (2 mmol, 0.242 g) was then added to the beaker and allowed to dissolve for 5 min, followed by adding 2 mL of 4.8 nM PVP-AgNP aqueous suspension into the beaker. After another 5 min, dopamine hydrochloride (5.8 mM, 0.220 g or 1.2 mM, 0.046 g) was added to the beaker to initiate the reaction. The reaction was then allowed to proceed for 5, 15, or 30 min at the dispersing speed of 2800 rpm. In the end, the reaction was quenched by adding 2 mL of 1 vol % acetic acid and the product was collected by centrifugation at 8000 rpm for 15 min, purified with water twice, recollected by centrifugation at 14 000 rpm for 10 min at 4 °C, redispersed in water, and stored at 4°C for future use. For the control experiments, PDA was prepared the same fashion as PDA-AgNPs but in the absence of AgNPs. For comparison, dopamine-capped Ag nanoparticles (DA-AgNPs) were prepared by mixing 2 mL of 10 nM (6.0×10^{12} particles/mL) PVP-AgNPs with 20 mL of 1 mM DA solution. The mixture was sonicated for 5 min and then incubated for 24 h at room temperature under magnetic stirring. After incubation, the product was purified with water thrice and collected by centrifugation at 6500 rpm for 15 min. The nanoparticles were resuspended in H₂O.

3.3.3. Material Characterization.

TEM images were captured using a transmission electron microscope (JEOL JEM-1011) with an accelerating voltage of 100 kV. The hydrodynamic diameters and ζ -potentials of the products were measured using a dynamic light scattering (DLS) instrument (Brookhaven ZetaPALS). The concentration of Ag was determined using an inductively coupled plasma mass spectrometer (Thermo Scientific iCAP Q ICP-MS). UV-vis spectra were taken on a UV-vis spectrophotometer (Agilent Cary50). XPS experiments were carried out in an ultrahigh vacuum (UHV) system with base pressures $<5 \times 10^{-9}$ Torr equipped with a hemispherical electron energy analyzer (SPECS, PHOIBOS 100) and twin anode X-ray source (SPECS, XR50). Al K α (1486.6 eV) radiation was used at 15 kV and 20 mA. The angle between the analyzer and X-ray source is 45°, and photoelectrons were collected along the sample surface normal. The XPS spectra were analyzed using CasaXPS. The FTIR spectra were obtained on an FTIR spectrometer (Shimadzu IRAffinity-1S) using a KBr pellet method.

3.3.4. Antimicrobial Evaluation.

An *Escherichia coli* (*E. coli*) K-12 strain (MG1655) transformed with a plasmid encoding enhanced green fluorescent proteins (EGFPs) and ampicillin resistance was used in this study. The bacteria were grown at 37 °C overnight in 6 mL of Luria broth (LB) medium supplemented with ampicillin in a shaking incubator with orbital rotation at 250 rpm. On the second day, the overnight culture was diluted in 40 mL of fresh LB medium to reach OD₆₀₀ = 0.05. Nanoparticle suspensions were added to the fresh culture aliquots (1 mL) to reach final concentrations of 0 (negative control; without nanoparticles), 20, 40, 60, and 80 $\mu\text{g/mL}$. For the growth curve assay with a microplate reader, 96-well clear bottom microplates were sterilized by incubating the wells with 200 proof ethanol for 5 min and then exposing the empty wells to UV light at 254 nm for 15

min. To avoid water condensation on the microplate lids during the measurements, the lids were coated with Triton X-100.⁵⁸ Briefly, 4 mL of 0.05% Triton X-100 in 20% ethanol was added to each microplate lid and incubated at room temperature for 15 s, followed by pouring off the Triton solution. The microplates were then air-dried before use. To measure the growth of bacteria, 200 μ L of the bacterial cultures (with or without nanoparticles) was transferred to the microplate wells. The microplates were covered with the preprocessed lids and placed in a microplate reader (BioTek Synergy H1 Hybrid) to monitor both the fluorescence (excitation = 488 nm; emission = 525nm) and the optical density (OD) at 600 nm of the bacteria in the wells. Wells with 200 μ L LB medium supplemented with ampicillin were used as blanks. The plates were maintained at 37 °C and rotated at 355 rpm. The fluorescence and OD readings were acquired every 10 min for 48 h. Each sample was measured with 4–6 replicates. The time series of the fluorescence-based growth curves for each sample was obtained by subtracting the mean of the fluorescence of the blanks at each time point from the mean of the fluorescence of the sample. In contrast, the time series of the OD-based growth curves for each sample was obtained by subtracting both the mean of the OD of the blanks at each time point and the initial OD (i.e., at time $t = 0$) from the mean of the OD values, to partly remove the contribution of AgNPs to the OD values.⁵⁹ The fluorescence-based growth curves were analyzed using our recently developed method based on time derivatives.⁵⁶ Briefly, the fluorescence-based growth curves were first smoothed (with a Hann window with a size of 15), followed by calculating the derivatives numerically $\dagger \Delta F / \Delta t \dagger |_{-i} = (F_{-(i+1)} - F_{-i}) / \Delta t$ and $\dagger (\Delta^2 F) / (\Delta t^2) \dagger |_{-i} = (\dagger \Delta F / \Delta t \dagger |_{-(i+1)} - \dagger \Delta F / \Delta t \dagger |_{-i}) / \Delta t$, where F is the fluorescence intensity and $\Delta t = 0.167$ h is the time interval between adjacent fluorescence readings. From the peaks in the second-order time derivatives, $\Delta^2 F / \Delta t^2$, we determined the peak locations (τ_{-p}^f) and peak heights (η_{-p}^f).

3.3.5. CellROX Staining and Quantification.

The bacteria were grown at 37 °C overnight in 7 mL of LB medium in a shaking incubator with orbital rotation at 250 rpm. On the second day, the overnight culture was diluted in 7 mL of fresh LB medium so that OD600 = 0.05. The fresh culture was regrown at 37 °C with orbital rotation at 250 rpm to reach OD600 = 0.3. The culture was aliquoted to 1 mL aliquots, followed by the addition of PDA15-AgNPs, PDA15, or PVP-AgNPs to reach a final concentration of 60 µg/mL. Untreated bacteria were used as a negative control. After incubating the samples at 37 °C and 250 rpm for 2 h, CellROX Orange Reagent (Thermo Fisher Scientific, Waltham, MA) was added to the untreated and treated bacteria at a final concentration of 5 µM and incubated at 37 °C with orbital shaking at 250 rpm for 30 min. The bacteria were harvested by centrifugation at 1000g for 10 min, followed by resuspension in 1 mL of 1× phosphate-buffered saline (PBS). The collected bacteria were further washed by centrifugation and resuspension in 1× PBS for five times to remove media and dyes. The stained bacteria were transferred to 5 × 5 mm² agarose pads (3% in 1× PBS). The agarose pad with the stained bacteria was flipped onto a clean coverslip (cleaned with sonication in detergent, 1 M NaOH, 100% ethanol, and ultrapure water sequentially). The chambers were then constructed by sandwiching rubber O-rings between the coverslips and clean microscope slides. The chambers were sealed using epoxy glue and then mounted on a microscope (with a 100× objective) for fluorescence imaging (excitation at 532 nm) and brightfield imaging. The fluorescence intensities of 100 bacteria for each sample were quantified using ImageJ.^{60, 61}

3.3.6. MitoTracker Staining and Quantification.

Bacterial samples (1 mL each) were prepared using a similar procedure as that for the CellROX staining experiments. Instead of the CellROX staining reagent, MitoTracker Green FM dye (Thermo Fisher Scientific, Waltham, MA) was added to the untreated and treated bacteria at

a final concentration of 300 nM and incubated at room temperature with orbital shaking at 250 rpm for 30 min. The stained bacteria were transferred to agarose pads, followed by fluorescence imaging (excitation at 488 nm) and brightfield imaging. The fluorescence intensities of 140 bacteria for each sample were quantified using ImageJ.^{60, 61}

3.3.7. Propidium Iodide (PI) Staining and Quantification.

Bacterial samples (1 mL each) were prepared similarly to those in the MitoTracker staining experiments except that the bacteria were fixed with 3.8% formaldehyde (Sigma-Aldrich, St. Louis, MO) before adding PI staining dyes (G-Biosciences, St. Louis, MO). After incubating the samples at room temperature with light shielded for 20 min, the bacteria were mounted on agarose pads, followed by phase contrast imaging and fluorescence imaging (excitation at 532 nm, with a 40× objective). The percentage of PI-stained bacterial cells was quantified using ImageJ.^{60, 61}

3.3.8. Scanning Electron Microscopy (SEM) and Fluorescence Imaging of Nanoparticle-Treated Bacteria.

The nanoparticle treated and fixed bacterial samples (1 mL each) were prepared similarly to those in the PI staining experiments. For SEM imaging, the bacteria were harvested by centrifugation at 1000g for 10 min, followed by resuspension in 1 mL autoclaved water. The collected bacteria were further washed by centrifugation and resuspension in water three times to remove salts from the samples. The prepared bacteria in water (1 mL) were dropped on silicon substrates and dried at room temperature for SEM imaging on an FEI Nova Nanolab 200 using a 15 kV acceleration voltage and a 5 mm working distance. For fluorescent imaging, the bacteria were harvested by centrifugation at 1000g for 10 min, followed by resuspension in 1 mL PBS. The

prepared bacteria were mounted on agarose pads, followed by fluorescence imaging (excitation at 532 nm, with a 100× objective).

3.4. Results and Discussion

To test the hypothesis of synergistic antimicrobial effects, we deposited the PDA coating on the surface of PVP-AgNPs with different lengths of coating time that was indicated in the abbreviations, PDA5-AgNPs, PDA15-AgNPs, and PDA30-AgNPs, for 5, 15, and 30 min, respectively, as illustrated in Figure 1A. **Figure 1B–E** shows the TEM images of the PVP-AgNPs and PDA-AgNPs with different coating times. After the PDA coating process, the average size of the nanoparticles measured from TEM images increased from 32 nm for PVP-AgNPs to 36, 43, and 54 nm for PDA5-AgNPs, PDA15-AgNPs, and PDA30-AgNPs, respectively. By taking the difference between PDA-AgNPs and PVP-AgNPs, the PDA coating thickness was estimated to be 4 to 11 and 22 nm and increased with the deposition time from 5 to 15 and 30 min. The deposition rate and coating thickness were consistent with our previously established reaction kinetics of the PDA coating process.⁵⁵ The coating kinetics was drastically slowed down when the reaction was performed in water overnight as dopamine-functionalized AgNPs (DA-AgNPs). The coating thickness was estimated to be 4 nm from the TEM image in Figure S1A. The hydrodynamic diameters and ζ -potentials of different nanoparticles are listed in **Table S1**. The hydrodynamic diameters of PDA15-AgNPs and PDA30-AgNPs are on the order of 200 nm, larger than those of PVP-AgNPs, PDA5-AgNPs, and DA-AgNPs, which are on the order of 100nm. The ζ -potentials of AgNPs surface-coated with PDA, PVP, or DA in PBS at pH 7.4 are all negative values, on the order of -10 mV, indicating that these AgNPs are negatively charged. For comparison, the PDA samples: PDA5, PDA15, and PDA30 were also synthesized under the same reaction conditions

but in the absence of AgNPs. They appeared to be spherical nanoparticles in the TEM images with sizes of 29,38, and 45 nm for PDA5, PDA15, and PDA30, respectively, as shown in **Figure S1B–D**.

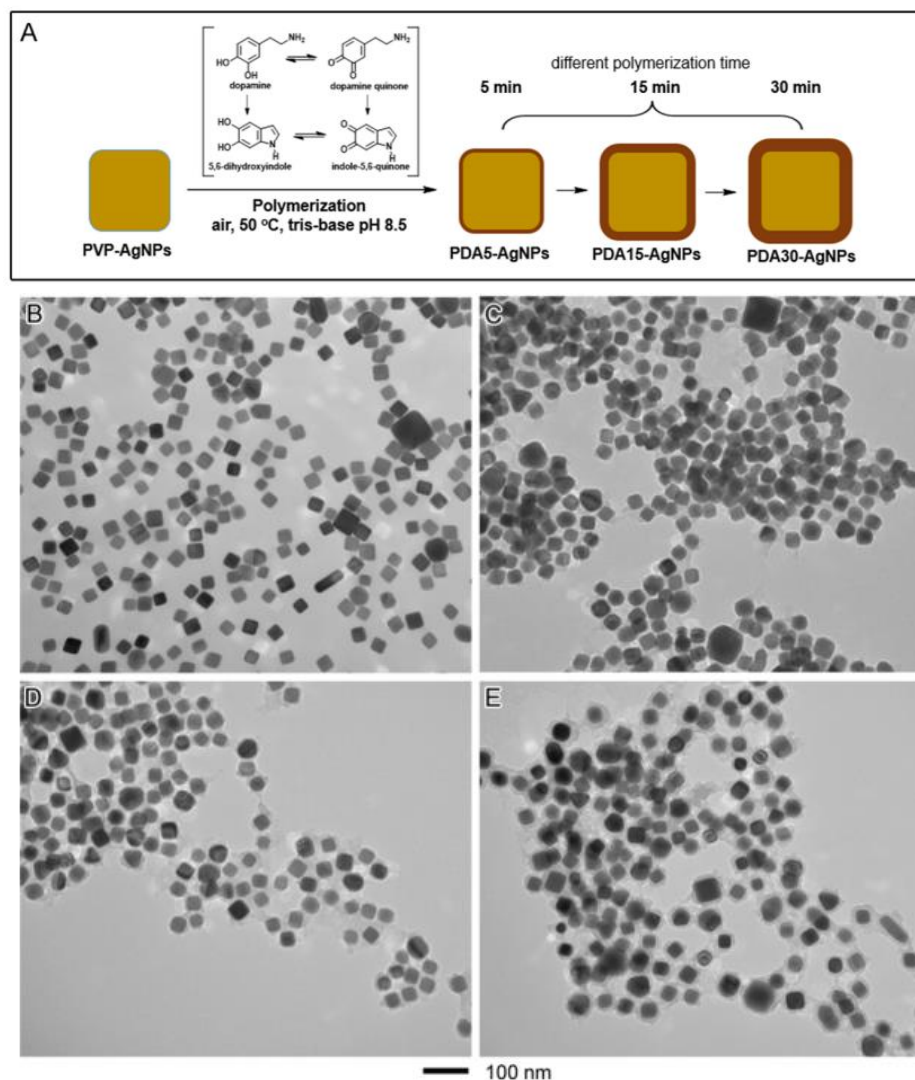


Figure 1. (A) Schematic illustration of the PDA deposition on PVP-AgNPs to form PDA-AgNPs at different time points. (B–E) TEM characterization of AgNPs: (B) PVP-AgNPs; (C–E) PDA-AgNPs obtained at different lengths of PDA coating times, 5, 15, and 30 min, respectively, denoted as PDA5-AgNPs (C), PDA15-AgNPs (D), and PDA30-AgNPs (E).

The increase of the coating thickness as a function of time was also verified by the UV–vis and XPS spectroscopy. **Figure 2A** displays the normalized UV–vis spectra obtained from the

aqueous suspensions of PVP-AgNPs, PDA5-AgNPs, PDA15-AgNPs, and PDA30-AgNPs. The zoom-in spectra indicated that the localized surface plasmon resonance (LSPR) of AgNPs shifted to the longer wavelength as the coating thickness increased (**Figure 2B**). The LSPR peak shifted from 420 nm for PVP-AgNPs to 435, 442, and 450 nm for PDA5-AgNPs, PDA15-AgNPs, and PDA30-AgNPs, respectively, following the same trend as our previously established relationship between the LSPR shift and PDA coating thickness.⁵⁵ Similarly, the LSPR peak became broader due to the inhomogeneity of the coating thickness as it can be seen in the TEM images. The increase of the PDA coating thickness was also confirmed by the quantitative analysis of the N-to-Ag ratio from XPS, as shown in **Figure 2C**. Since the experimental conditions were the same for all the sample measurements, we can assume that the analysis depth is the same across different samples. The typical probing depth of XPS is less than 10 nm from the surface, well below the size of the nanoparticle, and thus the analysis indeed reflects the composition of the nanoparticle surface. Because the repeating units of PVP (N-vinylpyrrolidone) and PDA (dopamine) contain only one N atom, the increase of the N-to-Ag ratio from 0.40 for PVP-AgNPs to 1.59, 2.90, and 7.57 for PDA5-AgNPs, PDA15-AgNPs, and PDA30-AgNPs suggests that the PDA coating became thicker with the increased PDA deposition time. We then evaluated the antimicrobial activities of these PDA-AgNPs with different coating times (PDA5-AgNPs, PDA15-AgNPs, and PDA30-AgNPs) against *E. coli* and compared the results with that of the control PVP-AgNPs. In this study, an *E. coli* K-12 strain (MG1655) transformed with a plasmid encoding EGFPs and ampicillin resistance was used. We incubated the same concentration of bacterial suspension that had an OD600 reading of 0.05 with different concentrations of nanoparticles from 0 to 20, 40, 60, and 80 $\mu\text{g/mL}$ (referred to as the concentration of Ag) and monitored the fluorescence of the bacteria (excitation = 488 nm; emission = 525 nm) using a microplate reader. Note that the

commonly used OD measurements were not chosen in this study due to interferences of the AgNPs' contribution to the OD600 value.

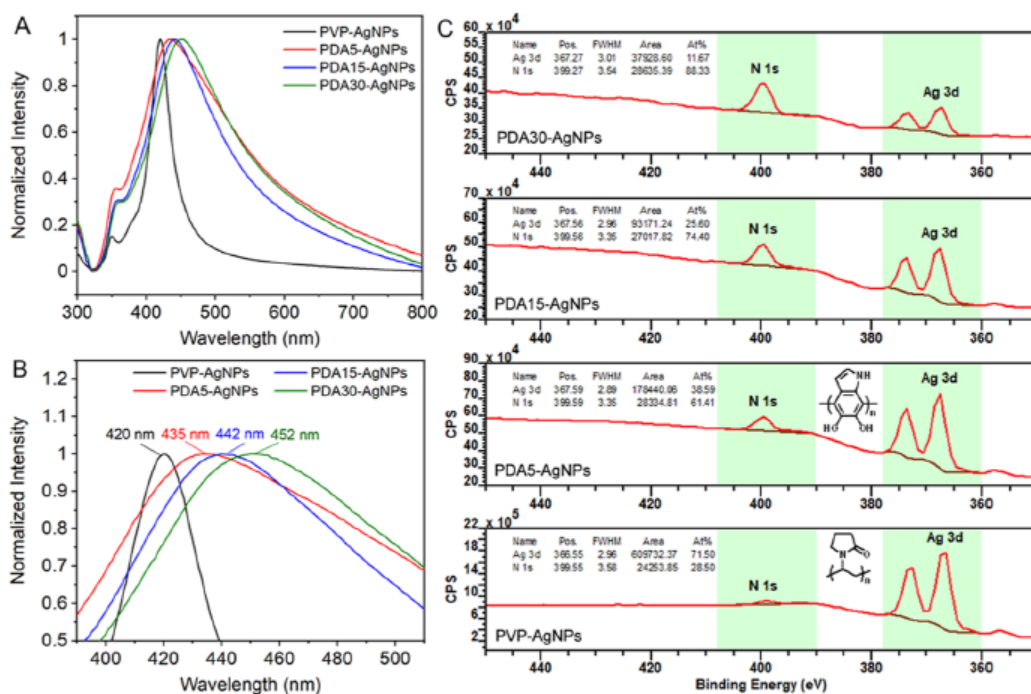


Figure 2. (A) UV-vis spectra of AgNPs before and after PDA coating process: PVP-AgNPs (black), PDA5-AgNPs (red), PDA15-AgNPs (blue), and PDA30-AgNPs (green); (B) zoom-in view of the spectra in (A) to identify the peak positions of each the samples; and (C) XPS spectra of Ag 3d and N 1s for the corresponding dry samples in (A). The baseline was corrected by the Shirley and linear method for Ag 3d and N 1s, respectively. The insets are the repeating units of PVP and PDA, illustrating that each repeating unit contains one N atom.

The fluorescence-based bacterial growth curves are shown as functions of time in **Figure 3**. Compared to the PVP-AgNPs (**Figure 3A**), the PDA coating significantly improved the antimicrobial effects of AgNPs (**Figure 3B–D**). At the concentration of 60 $\mu\text{g}/\text{mL}$ and above, the PDA-AgNPs completely suppressed bacterial growth. The increased antimicrobial activity follows the order of PDA15-AgNPs \approx PDA30-AgNPs > PDA5-AgNPs > PVP-AgNPs.

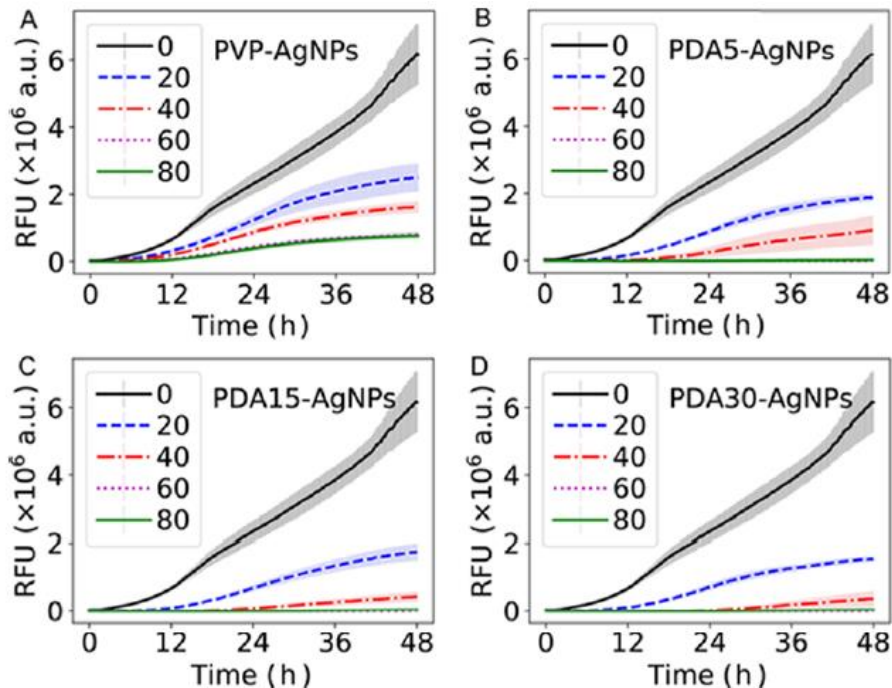


Figure 3. Fluorescence-based growth curves of the bacteria treated with AgNPs with different coatings: (A) PVP-AgNPs, (B) PDA5-AgNPs, (C) PDA15-AgNPs, and (D) PDA30-AgNPs. The fluorescence intensities of bacterial culture in microplate wells were shown as functions of time at various concentrations of 0 (untreated, negative control; black solid line), 20 (blue dashed lines), 40 (red dot dashed lines), 60 (magenta dotted lines), and 80 (green solid lines) $\mu\text{g/mL}$. The lines indicate the means of at least four replicates. Error bars (lighter areas) represent the standard errors of the means.

To investigate the role of the PDA coating to the antimicrobial effects of the AgNPs, we evaluated the antimicrobial activities of PDA themselves synthesized at the same conditions as the coating process but in the absence of AgNPs. **Figure 4** shows the bacterial growth plots of DA monomer, PDA5, PDA15, and PDA30. As can be seen, all of them display some degrees of bacterial inhibition effects, but none of them can completely suppress the bacteria after a 48 h incubation up to 80 $\mu\text{g/mL}$. PDA15 and PDA30 overall show a better bacterial inhibition agent than DA and PDA5. This observation appears to correlate well with that observed for the PDA-AgNPs, that is, PDA15-AgNPs and PDA30-AgNPs having better antimicrobial properties than

PDA5-AgNPs. In other words, PDA coating plays a significant role in enhancing the antimicrobial properties of AgNPs.

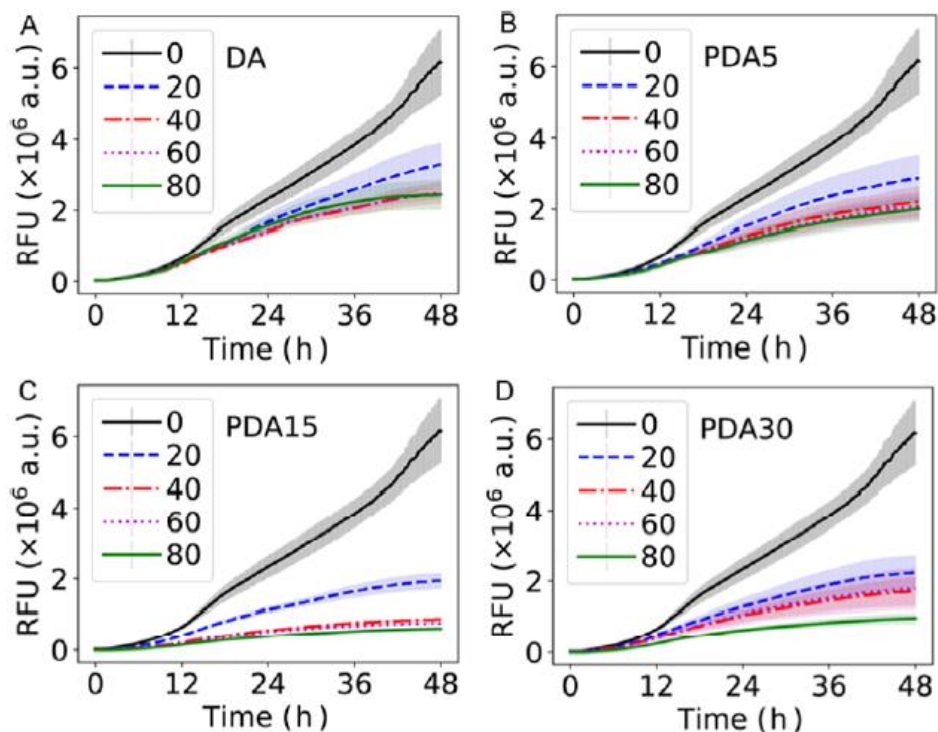


Figure 4. Fluorescence-based growth curves of bacteria treated with PDA synthesized at the same conditions as the coating process but in the absence of AgNPs: (A) 0 min (DA monomer), (B) 5 min (PDA5), (C) 15 min (PDA15), and (D) 30 min (PDA30). The fluorescence intensities of bacterial culture in microplate wells as functions of time at various concentrations of 0 (untreated, negative control; black solid line), 20 (blue dashed lines), 40 (red dot-dashed lines), 60 (magenta dotted lines), and 80 (green solid lines) $\mu\text{g/mL}$. The lines indicate the means of at least four replicates. Error bars (lighter areas) represent the standard errors of the means.

We further determine whether such enhancement from the PDA coating is simply an additive effect or a more interesting synergetic effect to the antimicrobial properties of AgNPs, by the new method that we developed recently.⁵⁶ In this method, the second-order time derivative of the fluorescence growth curve (F) is taken ($\Delta^2F/\Delta t^2$), showing a bell-shaped peak. The peak location (τ_{p^f}) and height (η_{p^f}) are related to the lag time and growth rate of the bacteria, as well as the expression rate, maturation rate, and degradation rate of GFP proteins; therefore,

changes in the peak location and height can report the changes in the growth behavior of the bacteria. **Figure 5** plots the peak location and height extracted from the fluorescence growth curves in **Figures 3** and **4**. We observed that all the samples decreased the peak height (η_{p^f} ; **Figure 5A**). PDA15-AgNPs and PDA30-AgNPs exhibited the strongest effects, while DA showed the least, consistent with the qualitative observations from the fluorescence growth curves (**Figures 3** and **4**). Note that if the fluorescence growth curves were too shallow (e.g., curves for PDA15-AgNPs and PDA30-AgNPs at $\geq 40 \mu\text{g/mL}$; **Figure 3C, D**), peaks were not identified reliably and thus the peak heights (or locations) were not shown. Interestingly, we observed that DA and PDA did not change the peak location (τ_{p^f}) of the time derivative of fluorescence growth curves ($\Delta^2F/\Delta t^2$), while τ_{p^f} increased significantly (i.e., the peak shifted to longer times) as the concentration of PVP-AgNPs or PDA-AgNPs increased. Furthermore, the changes of τ_{p^f} in the presence of the PDA-AgNPs were larger than those due to PVP-AgNPs. This observation is significant because it suggests that the PDA coating synergizes the antimicrobial activity of AgNPs, which could be seen from the changes in the peak locations.

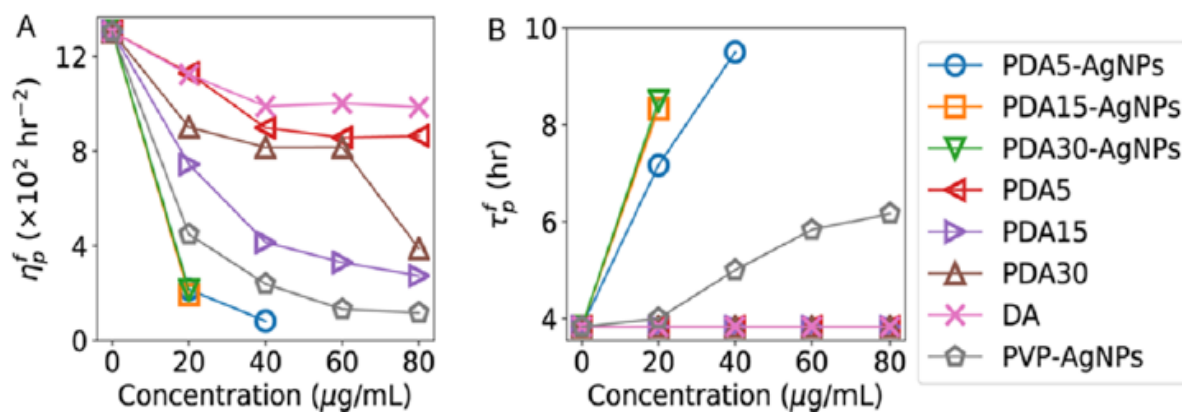


Figure 5. Dependence of the heights (A, η_{p^f}) and locations (B, τ_{p^f}) of the peaks, observed in the second-order time derivatives of the fluorescence growth curves, on the concentration of PDA, PDA-AgNPs, DA, and PVP-AgNPs.

We take the concentration of 20 $\mu\text{g}/\text{mL}$ as an example to further elucidate the synergistic effects observed from the PDA-AgNPs. Compared to the control (i.e., 0 $\mu\text{g}/\text{mL}$), the changes of the peak location due to PDA at 20 $\mu\text{g}/\text{mL}$ (i.e., PDA5, PDA15, and PDA30) were $\delta\tau_{\text{PDA}} = 0$, while those for AgNPs without PDA (i.e., PVP-AgNPs) at the same concentration were $\delta\tau_{\text{AgNP}} \approx 0.2$ h. However, the changes due to PDA-AgNPs at the same concentration, $\delta\tau_{\text{PDA-AgNP}}$, ranging from 3.3 h (PDA5-AgNPs) to 4.7 h (PDA30-AgNPs), showed that $\delta\tau_{\text{PDA-AgNP}} \gg \delta\tau_{\text{PDA}} + \delta\tau_{\text{AgNP}}$. In other words, in terms of the shift of peak locations of the time derivatives of the fluorescence growth curves, the effect of PDA-AgNPs was much larger than the sum of the effects from PDA and AgNPs. Therefore, the enhancement in the antimicrobial activities of AgNPs due to the PDA coating is not additive but synergetic. To further confirm the synergistic effects of the PDA coating and AgNPs, we also examined the OD growth curves of the same samples (**Figure S2**), which suffered from multiple scattering⁶² at high OD values and interference from the contributions of the AgNPs to the OD₆₀₀ value. The first problem of multiple scattering could be partly avoided by focusing on low OD values (e.g., <1.0), while the second problem was much more complicated. Nonetheless, it was possible to compare qualitatively among the different samples if we vertically shifted the growth curves by subtracting the initial OD value from each growth curve, $\text{OD}_{600}(t) = \text{OD}_{600 \text{ raw}}(t) - \text{OD}_{600 \text{ raw}}(0)$.⁵⁹ We observed that the growth curves of the bacteria treated with PDA5, PDA15, or PDA30 overlapped with the untreated control, indicating that PDA alone did not change the growth behavior of the bacteria. PVP-AgNPs shifted the growth curve to the right by several hours, indicating an elongation of the lag time and consistent with our previous observations qualitatively.⁵⁹ It is noted that the OD measurements using the microplate reader showed a peak around 1–2 h for the bacteria treated with PVP-AgNPs, which was also present, but much less dominant in cuvette-based growth curve measurements, presumably due to the

interactions of the AgNPs with the medium (e.g., precipitation and re-dissolution of AgNPs in Cl⁻-rich solutions) and/or the bacteria (e.g., adsorption of AgNPs to the bacterial surfaces). In contrast, PDA-AgNPs suppressed the growth of bacteria for at least 24 hours. The elongation of the lag time in the presence of PDA-AgNPs was again much longer than the sum of those due to PDA or AgNPs alone, providing evidence to support the conclusion that PDA coating synergizes the antimicrobial activity of AgNPs.

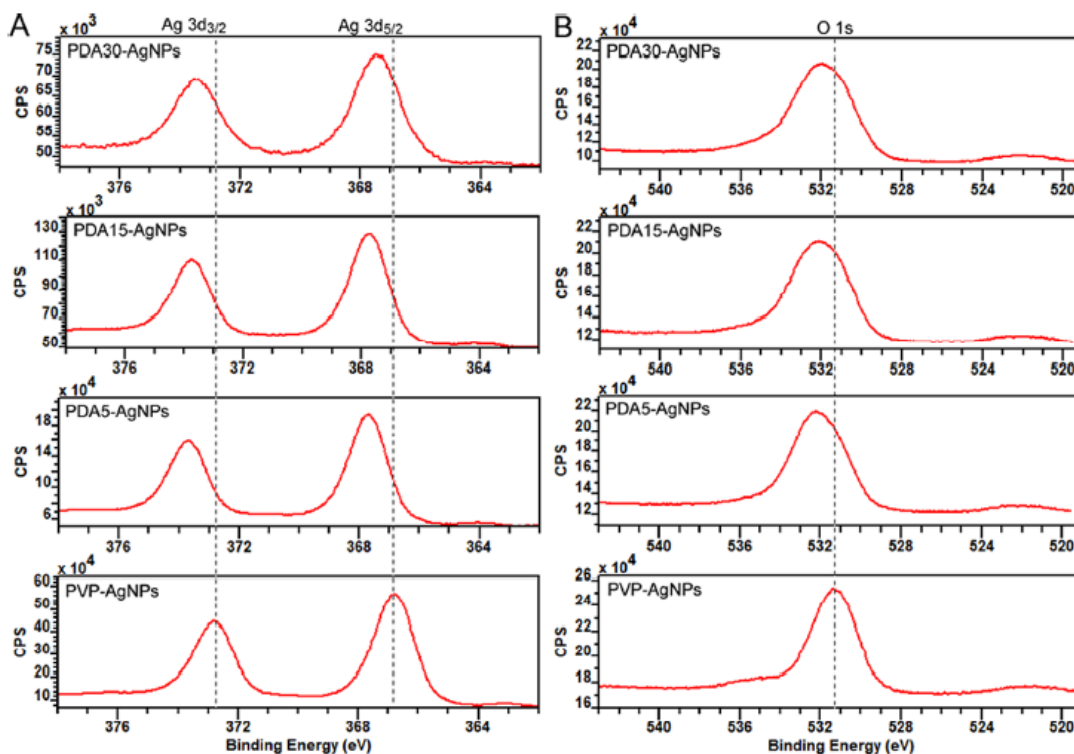


Figure 6. XPS of Ag 3d (A) and O 1s (B). Samples from bottom to top are corresponding to PVP-AgNPs, PDA5-AgNPs, PDA15-AgNPs, and PDA30-AgNPs.

To understand the synergistic effects between the PDA coating and AgNPs, we investigated the chemical properties of the PDA-AgNPs. **Figure 6A** displays the XPS spectra of Ag 3d of the PDA-AgNPs with the comparison of PVP-AgNPs with a 6 eV energy splitting between Ag 3d_{5/2} and Ag 3d_{3/2}. The binding energy (BE) of Ag 3d_{5/2} shifted from 366.8 eV for

PVP-AgNPs to 367.7, 367.8, and 367.4 eV for PDA5-AgNPs, PDA15-AgNPs, and PDA30-AgNPs, respectively. The approximately 1 eV upward shift of Ag 3d on the surface of AgNPs with the PDA coating suggests that compared to PVP-AgNPs, PDA-AgNPs could be attributed to a decrease of the initial state effect due to the chemical environment change or a loss of electrons from Ag. From the valence point of view, the higher valence/oxidation state could increase the antimicrobial potency of Ag;⁶³ however, the coordination between Ag and PDA through mainly the catechol group may play an important role in governing the antimicrobial activity of the PDA-AgNPs.⁶⁴ The presence of the catechol group/partially oxidized catechol group was evidenced by the XPS analysis of oxygen. From the O 1s spectra in **Figure 6B**, an approximately 0.5 eV upward shift of the O 1s BE was observed from 531.4 eV for PVP-AgNPs to 532.1, 532.1, and 531.9 eV for PDA5-AgNPs, PDA15-AgNPs, and PDA30-AgNPs, respectively. The typical BE of O 1s for organic compounds can be assigned as follows: from 531.3 to 532.0 eV for N–C=O and from 532.7 to 533.1 eV for C–OH (aliphatic), as well as 532.2 for C=O (aromatic) and 533.6 eV for C–OH (aromatic).⁶⁵ The deconvoluted spectra of O 1s in **Figure S3** indicate the increase of the hydroxyl percentage from ~10 to ~25% before and after PDA coating.

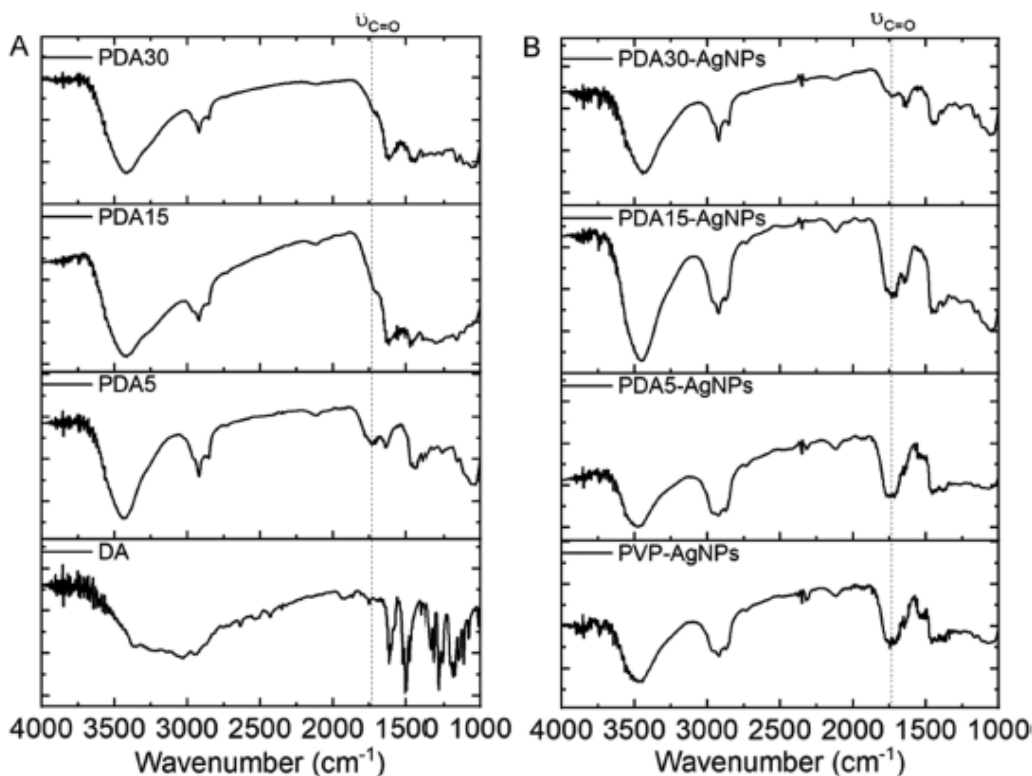


Figure 7. FTIR spectra of samples without or with AgNPs: (A) from bottom to top corresponding to DA, PDA5, PDA15, and PDA30; and (B) from bottom to top corresponding to PVP-AgNPs, PDA5-AgNPs, PDA15-AgNPs, and PDA30-AgNPs.

The increased hydroxyl context after PDA coating was also confirmed by the evidence from the analysis of FTIR spectra of DA, PDA, and PDA-AgNPs, as shown in **Figure 7**. The FTIR spectrum of monomer DA exhibited a number of characteristic peaks that can be assigned to the N–H stretching (3370 cm^{-1}) and bending (1614 cm^{-1}) vibrations of the primary amine, the intermolecular hydrogen-bonded O–H stretching (3250 cm^{-1}) of the catechol, the aromatic ring stretch (1600 , 1496 , and 1469 cm^{-1}), and the aromatic C–H stretch (3036 cm^{-1}) and methyl C–H stretch (2041 cm^{-1}).^{66,67} Exposure of DA to air under basic conditions (Tris-base, pH 8.5) leads to the oxidation of DA to dopamine quinone and cyclic reaction to 5,6-dihydroxyindole and its oxidized form indole-5,6-quinone (**Figure 1A**). These cyclic and oxidized monomers further react to form PDA with increased structural complexity. All of the PDA spectra exhibited a board band

at $\sim 3420\text{ cm}^{-1}$ that can be assigned to intermolecular hydrogen-bonded O–H stretch with the N–H stretch of secondary amine buried underneath and a set of distinguishable bands at 1632, 1455, and 1160 cm^{-1} that can be attributed to the aromatic ring stretching vibrations of the polyindole structures.⁶⁸ Additionally, the band at 1730 cm^{-1} corresponding to C=O stretching vibration^{66, 67} appeared at the PDA spectra; however, the relative intensity of C=O stretch to the polyindole ring stretch decreases with increased reaction time. A similar trend was observed on the PDA-AgNPs, meaning that the ratio of 5,6-dihydroxyindole to indole-5,6-quinone increased as the PDA coating became thicker. This observation suggests that the polymerization of the monomers can lead to the conversion of quinone back to catechol agreed with the theoretical predictions;⁶⁹ however, the further extension of the exposure of PDA to O_2 would eventually convert catechol to quinone. Although the FTIR is a bulk technique, it only probes the polymer structures. Since the polymer is the coating layer on the nanoparticles with its thickness increasing from 4 for PDA5-AgNP to 11 and 22 nm for PDA15-AgNP and PDA30-Ag, respectively, XPS and FTIR, in this case, probe mostly the surface (i.e., coating layer) of the nanoparticles. From the quantitative analysis of XPS, we observed that the Ag-to polymer ratio decreased with increasing coating thickness (**Figure 2C**). The observed Ag signals in the thicker polymer coating ($>10\text{ nm}$), well above the probing depth of XPS, suggest that Ag is present in the polymer coating. The FTIR results indicate the presence of a catechol group in the polymer coating of the PDA-AgNP nanoparticles (**Figure 7B**), which agree with the XPS findings (**Figure S3**). The interaction between the Ag in the polymer coating and the O of the catechol group can be seen based on the shifts of Ag 3d and O 1s in the XPS spectra (**Figure 6**) that the O donates electrons to the Ag, suggesting the plausible coordination between Ag and the catechol group of the PDA coating. Such metal–catechol coordination can lead to the synergistic effect of the PDA-AgNPs as a potent antimicrobial agent because heavy

metals such as the Ag^0/Ag ions from the AgNPs can catalyze the redox cycling of the catechol group in the PDA coating.⁶⁴ As a result, an electron from the catechol–quinone redox cycle can convert molecular oxygen (O_2) to superoxide (O_2^-), which can be further reduced to hydrogen peroxide (H_2O_2) and hydroxyl radicals ($\cdot\text{OH}$) in the presence of heavy metals such as Ag.

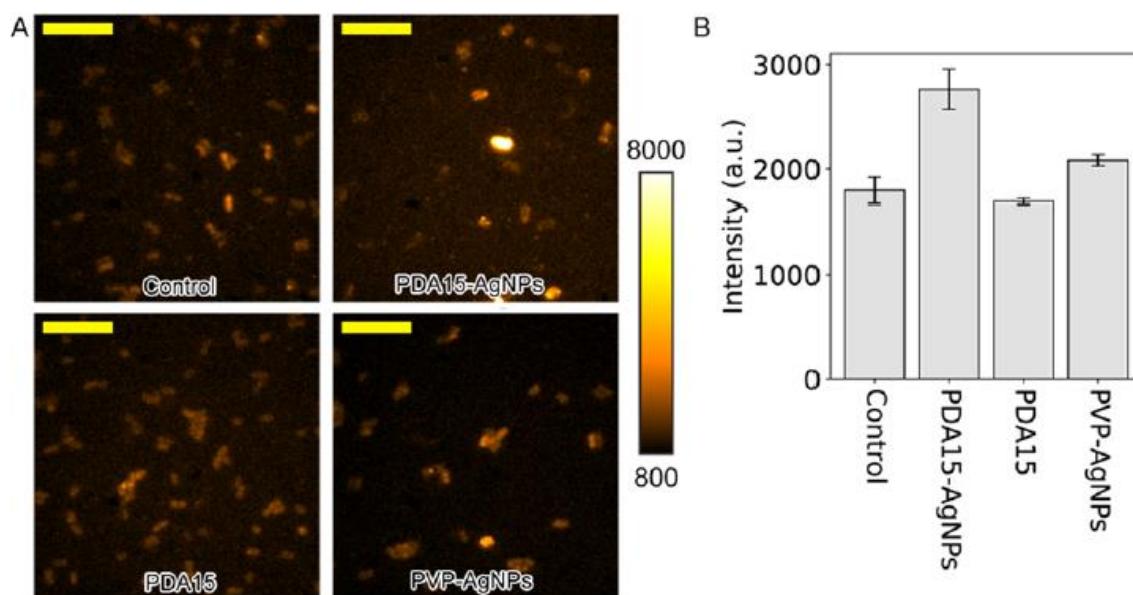


Figure 8. Promoted generation of ROS by PDA-AgNPs. (A) Representative fluorescent images of bacteria stained by CellROX Orange Reagent. Scale bar = 10 μm . (B) Mean fluorescence intensities of the stained bacteria. Error bars represent the standard error of the mean.

We used CellROX Orange Reagent to quantify the ROS of PDA15-AgNP-treated cells and compared the results to those of the control (cells with no treatment), PDA15-treated cells, and PVP-AgNP-treated cells (**Figure 8A**, with a treatment time of 2 h). Despite large cell-to-cell variations, quantitative analysis of fluorescence signals indicates a 50% enhancement, on average, in the intensities of the PDA15-AgNP-treated cells compared to the others (**Figure 8B**). It is known that ROS can cause oxidative damages to cell membranes.⁷⁰ The biological effects of PDA-AgNPs to the bacterial cell membrane were examined by MitoTracker Green FM dye and PI dye after treating the bacterial cells with PDA15-AgNPs, PDA15, and PVP-AgNPs for 2 h. The attachment

of the nanoparticles on the bacteria was investigated by both fluorescent imaging and SEM imaging. The fluorescent images of nanoparticles showed that more aggregated PDA-AgNPs were around and/or attached to the bacteria than PDA and PVP-AgNPs (**Figure S4A**), which agreed with the SEM results (**Figure S4B**).

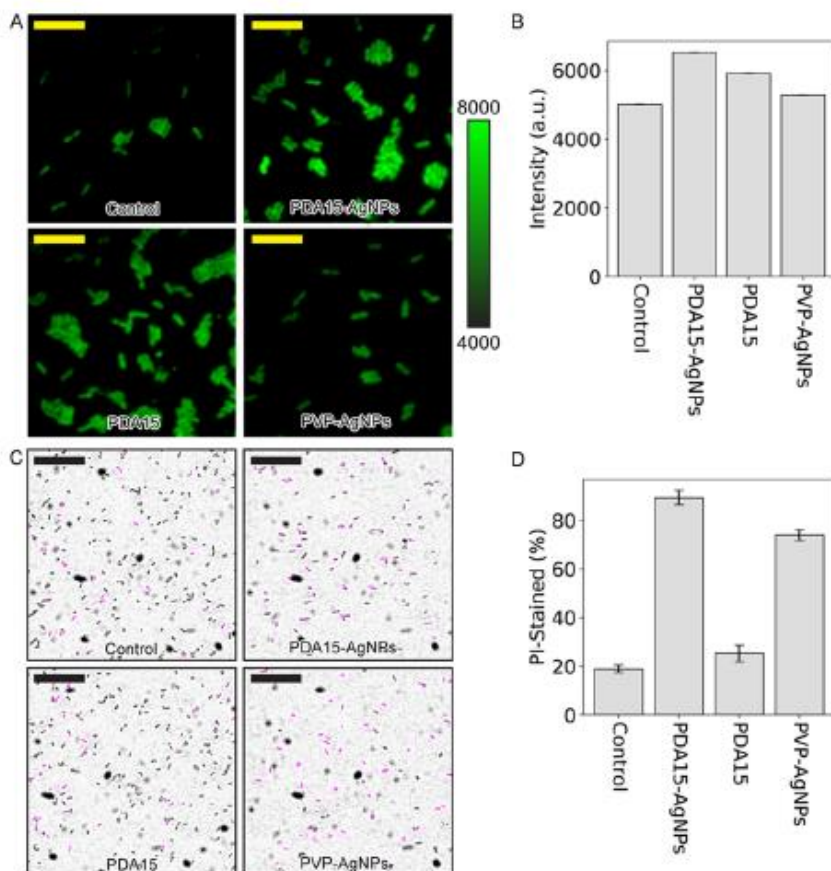


Figure 9. Higher membrane damage caused by PDA-AgNPs. (A) Representative fluorescent images of bacteria stained by MitoTracker Green FM dye. Scale bar = 10 μ m. (B) Mean fluorescence intensities of the MitoTracker stained bacteria. Error bars represent the standard error of the mean. (C) Representative fluorescent images of bacteria stained by PI (purple) on top of the corresponding phase contrast images (grayscale). Scale bar = 25 μ m. (D) Mean percentage of the PI-stained bacteria. Error bars represent the standard error of the mean.

By staining the bacterial membrane using MitoTracker Green FM dye, we observed that the bacterial membrane became brighter after subjecting the bacteria to PDA15-AgNPs (**Figure 9A**), indicating the change of bacterial membrane potential. To quantify this effect, we estimated

the mean intensities of 140 bacteria for each sample (i.e., untreated control, treated with PDA15-AgNP, PDA15, and PVP-AgNP) and observed that, although increased brightness was observed for all the treated bacteria, those treated with PDA15-AgNPs showed the highest intensity increase (**Figure 9B**). In addition, to assess the significance of membrane damage caused by the nanoparticle, we stained the bacterial DNA with PI. The rationale is that if PI molecules could enter the bacteria to stain DNA, the membrane damage is significant enough to allow the influx of ions and other small organic molecules. Representative images of untreated and treated bacteria are shown in **Figure 9C**, where the fluorescent images from PI staining (purple) are superposed on the phase contrast images (grayscale). It was observed that, compared to the control, more than fourfold of the bacteria treated with PDA15-AgNPs were stained by PI (**Figure 9D**), suggesting that PDA-AgNPs caused more membrane damage compared to PVP-AgNPs. In contrast, the bacteria treated by PDA15 alone showed a much lower percentage of PI-stained bacteria (slightly higher than the control though), indicating that PDA alone did not cause significant membrane damage. These results confirmed that the synergistic effects of PDA-AgNPs led to greater antimicrobial activity than the simple addition of PDA and AgNPs.

3.5. Conclusion

We have synthesized the PDA-AgNPs with controllable PDA coating thickness to study the surface effects on the antimicrobial activity of AgNPs. The thickness of the PDA coating on the AgNPs increased with the PDA deposition time from 3.5 to 11.4 and 22.1 nm for the reaction time of 5, 15, and 30 min, respectively. The antimicrobial activities of the PDA-AgNPs were evaluated by the fluorescence-based growth curve assays on *E. coli*, indicating that PDA-AgNPs were better antimicrobial agents than PVP-AgNPs and PDA themselves. More importantly, the

synergistic effects between the PDA coating and the AgNPs were found to significantly increase the potency of AgNPs against *E. coli*. XPS and FTIR analysis unveiled the coordination between Ag and catechol group on the PDA coating that could be responsible for the synergistic effects. The PDA-Ag interaction of PDA-AgNPs increased the ROS generation and caused significant damage to the bacterial membrane. The result indicated that catechol-rich PDA coating exhibited more pronounced synergistic effects on the antimicrobial AgNPs. Our findings also elucidated the molecular mechanism for the previous studies, which illustrated the importance of the choice of fabrication methods in yielding a PDA surface with strong antimicrobial properties.^{71,72} This study not only demonstrated the importance of the surface effects on the antimicrobial properties of AgNPs, but also laid out guiding principles for the future development of metal nanoparticle-based antimicrobial agents.

3.5.1. Supporting Information

Table of hydrodynamic diameter and ζ -potential measurements of surface-modified AgNPs; TEM images of the PDA samples; bacterial growth curves using OD measurement; XPS deconvoluted spectra of O 1s of the PDA-AgNP samples; and fluorescence and SEM images of bacteria treated with different conditions.

3.5.2. Acknowledgement

This work was supported in part by the grant from the National Science Foundation NSF CBET 1826642, pilot grants from Arkansas Bioscience Institute, and by the Center for Advanced Surface Engineering (NSF EPSCoR OIA 1457888). ICP-MS measurements were carried out at the Arkansas Mass Spectrometry facility, which is supported by the Arkansas Biosciences Institute. XPS measurements were performed at the Center for Functional Nanomaterials (CFN), which is a U.S. DOE Office of Science Facility, at BNL under Contract No. DE-SC0012704.

3.6. References

1. Alexander, J. W., History of the Medical Use of Silver. *Surgical Infections* **2009**, *10* (3), 289-292.
2. Makowski, M.; Silva, I. C.; do Amaral, C. P.; Goncalves, S.; Santos, N. C., Advances in Lipid and Metal Nanoparticles for Antimicrobial Peptide Delivery. *Pharmaceutics* **2019**, *11* (11), 33.
3. Bracey, N. A.; Zipursky, J. S.; Juurlink, D. N., Argyria caused by chronic ingestion of silver. *Canadian Medical Association Journal* **2018**, *190* (5), E139-E139.
4. Ferrara, G.; Filosa, A.; Mariani, M. P.; Fasanella, L., Occupational Argyria of the Nasal Mucosa. *Head & Neck Pathology* **2018**, *12* (2), 252-254.
5. Lansdown, A. B., Silver in Health Care: Antimicrobial Effects and Safety in Use. In *Biofunctional Textiles and the Skin*. Karger Publishers: 2006; Vol. 33, p 17–34.
6. Marambio-Jones, C.; Hoek, E. M. V., A review of the antibacterial effects of silver nanomaterials and potential implications for human health and the environment. *Journal of Nanoparticle Research* **2010**, *12* (5), 1531-1551.
7. Rai, M.; Yadav, A.; Gade, A., Silver nanoparticles as a new generation of antimicrobials. *Biotechnology Advances* **2009**, *27* (1), 76-83.
8. Shahid ul, I.; Butola, B. S.; Mohammad, F., Silver nanomaterials as future colorants and potential antimicrobial agents for natural and synthetic textile materials. *Rsc Advances* **2016**, *6* (50), 44232-44247.
9. Kalantari, K.; Mostafavi, E.; Afifi, A. M.; Izadiyan, Z.; Jahangirian, H.; Rafiee-Moghaddam, R.; Webster, T. J., Wound dressings functionalized with silver nanoparticles: promises and pitfalls. *Nanoscale* **2020**, *12* (4), 2268-2291.
10. Deshmukh, S. P.; Patil, S. M.; Mullani, S. B.; Delekar, S. D., Silver nanoparticles as an effective disinfectant: A review. *Materials Science & Engineering C-Materials for Biological Applications* **2019**, *97*, 954-965.
11. Simoncic, B.; Klemencic, D., Preparation and performance of silver as an antimicrobial agent for textiles: A review. *Textile Research Journal* **2016**, *86* (2), 210-223.
12. Haidari, H.; Garg, S.; Vasilev, K.; Kopecki, Z.; Cowin, A. J., Silver-based wound dressings: current issues and future developments for treating bacterial infections. *Wound Practice and Research* **2020**, *28* (4), 173-180.
13. Ogunsona, E. O.; Muthuraj, R.; Ojogbo, E.; Valerio, O.; Mekonnen, T. H., Engineered nanomaterials for antimicrobial applications: A review. *Applied Materials Today* **2020**, *18*, 32.

14. Duran, N.; Duran, M.; de Jesus, M. B.; Seabra, A. B.; Favaro, W. J.; Nakazato, G., Silver nanoparticles: A new view on mechanistic aspects on antimicrobial activity. *Nanomedicine-Nanotechnology Biology and Medicine* **2016**, *12* (3), 789-799.
15. Stabryla, L. M.; Johnston, K. A.; Millstone, J. E.; Gilbertson, L. M., Emerging investigator series: it's not all about the ion: support for particle-specific contributions to silver nanoparticle antimicrobial activity. *Environmental Science-Nano* **2018**, *5* (9), 2047-2068.
16. Gharpure, S.; Akash, A.; Ankamwar, B., A Review on Antimicrobial Properties of Metal Nanoparticles. *Journal of Nanoscience and Nanotechnology* **2020**, *20* (6), 3303-3339.
17. Stabryla, L. M.; Johnston, K. A.; Millstone, J. E.; Gilbertson, L. M., Emerging investigator series: it's not all about the ion: support for particle-specific contributions to silver nanoparticle antimicrobial activity. *Environmental Science: Nano* **2018**, *5* (9), 2047-2068.
18. Helmlinger, J.; Sengstock, C.; Gross-Heitfeld, C.; Mayer, C.; Schildhauer, T. A.; Koller, M.; Epple, M., Silver nanoparticles with different size and shape: equal cytotoxicity, but different antibacterial effects. *Rsc Advances* **2016**, *6* (22), 18490-18501.
19. Ertem, E.; Gutt, B.; Zuber, F.; Allegri, S.; Le Ouay, B.; Mefti, S.; Formentin, K.; Stellacci, F.; Ren, Q., Core-Shell Silver Nanoparticles in Endodontic Disinfection Solutions Enable Long-Term Antimicrobial Effect on Oral Biofilms. *Acs Applied Materials & Interfaces* **2017**, *9* (40), 34762-34772.
20. Kubo, A. L.; Capjak, I.; Vrcek, I. V.; Bondarenko, O. M.; Kurvet, I.; Vija, H.; Ivask, A.; Kasemets, K.; Kahru, A., Antimicrobial potency of differently coated 10 and 50 nm silver nanoparticles against clinically relevant bacteria *Escherichia coli* and *Staphylococcus aureus*. *Colloids and Surfaces B-Biointerfaces* **2018**, *170*, 401-410.
21. Liu, H.; Qu, X.; Kim, E.; Lei, M.; Dai, K.; Tan, X. L.; Xu, M.; Li, J. Y.; Liu, Y. P.; Shi, X. W.; Li, P.; Payne, G. F.; Liu, C. S., Bio-inspired redox-cycling antimicrobial film for sustained generation of reactive oxygen species. *Biomaterials* **2018**, *162*, 109-122.
22. Ivask, A.; ElBadawy, A.; Kaweeterawat, C.; Boren, D.; Fischer, H.; Ji, Z. X.; Chang, C. H.; Liu, R.; Tolaymat, T.; Telesca, D.; Zink, J. I.; Cohen, Y.; Holden, P. A.; Godwin, H. A., Toxicity Mechanisms in *Escherichia coli* Vary for Silver Nanoparticles and Differ from Ionic Silver. *Acs Nano* **2014**, *8* (1), 374-386.
23. Chang, T. Y.; Chen, C. C.; Cheng, K. M.; Chin, C. Y.; Chen, Y. H.; Chen, X. A.; Sun, J. R.; Young, J. J.; Chiueh, T. S., Trimethyl chitosan-capped silver nanoparticles with positive surface charge: Their catalytic activity and antibacterial spectrum including multidrug-resistant strains of *Acinetobacter baumannii*. *Colloids and Surfaces B-Biointerfaces* **2017**, *155*, 61-70.

24. Qiao, Z. Z.; Yao, Y.; Song, S. M.; Yin, M. H.; Luo, J. B., Silver nanoparticles with pH induced surface charge switchable properties for antibacterial and antibiofilm applications. *Journal of Materials Chemistry B* **2019**, *7* (5), 830-840.
25. Alqahtany, M.; Khadka, P.; Niyonshuti, I.; Krishnamurthi, V. R.; Sadoon, A. A.; Challapalli, S. D.; Chen, J. Y.; Wang, Y., Nanoscale reorganizations of histone-like nucleoid structuring proteins in Escherichia coli are caused by silver nanoparticles. *Nanotechnology* **2019**, *30* (38), 14.
26. Ryu, J. H.; Messersmith, P. B.; Lee, H., Polydopamine Surface Chemistry: A Decade of Discovery. *Acs Applied Materials & Interfaces* **2018**, *10* (9), 7523-7540.
27. Liu, Y. L.; Ai, K. L.; Lu, L. H., Polydopamine and Its Derivative Materials: Synthesis and Promising Applications in Energy, Environmental, and Biomedical Fields. *Chemical Reviews* **2014**, *114* (9), 5057-5115.
28. Liao, Y. A.; Wang, Y. Q.; Feng, X. X.; Wang, W. C.; Xu, F. J.; Zhang, L. Q., Antibacterial surfaces through dopamine functionalization and silver nanoparticle immobilization. *Materials Chemistry and Physics* **2010**, *121* (3), 534-540.
29. Sileika, T. S.; Kim, H. D.; Maniak, P.; Messersmith, P. B., Antibacterial Performance of Polydopamine-Modified Polymer Surfaces Containing Passive and Active Components. *Acs Applied Materials & Interfaces* **2011**, *3* (12), 4602-4610.
30. Zhang, Z.; Zhang, J.; Zhang, B. L.; Tang, J. L., Mussel-inspired functionalization of graphene for synthesizing Ag-polydopamine-graphene nanosheets as antibacterial materials. *Nanoscale* **2013**, *5* (1), 118-123.
31. Jiang, J. H.; Zhu, L. P.; Zhu, L. J.; Zhang, H. T.; Zhu, B. K.; Xu, Y. Y., Antifouling and Antimicrobial Polymer Membranes Based on Bioinspired Polydopamine and Strong Hydrogen-Bonded Poly(N-vinyl pyrrolidone). *Acs Applied Materials & Interfaces* **2013**, *5* (24), 12895-12904.
32. Son, H. Y.; Ryu, J. H.; Lee, H.; Nam, Y. S., Silver-Polydopamine Hybrid Coatings of Electrospun Poly(vinyl alcohol) Nanofibers. *Macromolecular Materials and Engineering* **2013**, *298* (5), 547-554.
33. Fu, Y.; Li, G. F.; Tian, M.; Wang, X.; Zhang, L. Q.; Wang, W. C., Preparation of Silver Nanoparticle Immobilized Fibrillar Silicate by Poly(dopamine) Surface Functionalization. *Journal of Applied Polymer Science* **2014**, *131* (3), 7.
34. Xie, Y. J.; Yan, B.; Xu, H. L.; Chen, J.; Liu, Q. X.; Deng, Y. H.; Zeng, H. B., Highly Regenerable Mussel-Inspired Fe₃O₄@Polydopamine-Ag Core-Shell Microspheres as Catalyst and Adsorbent for Methylene Blue Removal. *Acs Applied Materials & Interfaces* **2014**, *6* (11), 8845-8852.

35. Lu, Z. S.; Xiao, J.; Wang, Y.; Meng, M., In situ synthesis of silver nanoparticles uniformly distributed on polydopamine-coated silk fibers for antibacterial application. *Journal of Colloid and Interface Science* **2015**, *452*, 8-14.
36. Wang, Z. L.; Ou, J. F.; Wang, Y.; Xue, M. S.; Wang, F. J.; Pan, B.; Li, C. Q.; Li, W., Anti-bacterial superhydrophobic silver on diverse substrates based on the mussel-inspired polydopamine. *Surface & Coatings Technology* **2015**, *280*, 378-383.
37. Tang, L.; Livi, K. J. T.; Chen, K. L., Polysulfone Membranes Modified with Bioinspired Polydopamine and Silver Nanoparticles Formed in Situ To Mitigate Biofouling. *Environmental Science & Technology Letters* **2015**, *2* (3), 59-65.
38. GhavamiNejad, A.; Aguilar, L. E.; Ambade, R. B.; Lee, S. H.; Park, C. H.; Kim, C. S., Immobilization of silver nanoparticles on electropolymerized polydopamine films for metal implant applications. *Colloid and Interface Science Communications* **2015**, *6*, 5-8.
39. Yang, Z.; Wu, Y. C.; Wang, J. Q.; Cap, B.; Tang, C. Y. Y., In Situ Reduction of Silver by Polydopamine: A Novel Antimicrobial Modification of a Thin-Film Composite Polyamide Membrane. *Environmental Science & Technology* **2016**, *50* (17), 9543-9550.
40. Yang, E.; Chae, K. J.; Alayande, A. B.; Kim, K. Y.; Kim, I. S., Concurrent performance improvement and biofouling mitigation in osmotic microbial fuel cells using a silver nanoparticle-polydopamine coated forward osmosis membrane. *Journal of Membrane Science* **2016**, *513*, 217-225.
41. Raza, Z. A.; Rehman, A.; Anwar, F.; Usman, A., Development and antibacterial performance of silver nanoparticles incorporated polydopamine-polyester-knitted fabric. *Bulletin of Materials Science* **2016**, *39* (2), 391-396.
42. Huang, L. C.; Zhao, S.; Wang, Z.; Wu, J. H.; Wang, J. X.; Wang, S. C., In situ immobilization of silver nanoparticles for improving permeability, antifouling and anti-bacterial properties of ultrafiltration membrane. *Journal of Membrane Science* **2016**, *499*, 269-281.
43. Jia, Z. J.; Xiu, P.; Li, M.; Xu, X. C.; Shi, Y. Y.; Cheng, Y.; Wei, S. C.; Zheng, Y. F.; Xi, T. F.; Cai, H.; Liu, Z. J., Bioinspired anchoring AgNPs onto micro-nanoporous TiO₂ orthopedic coatings: Trap-killing of bacteria, surface-regulated osteoblast functions and host responses. *Biomaterials* **2016**, *75*, 203-222.
44. Cai, R.; Tao, G.; He, H. W.; Song, K.; Zuo, H.; Jiang, W. C.; Wang, Y. J., One-Step Synthesis of Silver Nanoparticles on Polydopamine-Coated Sericin/Polyvinyl Alcohol Composite Films for Potential Antimicrobial Applications. *Molecules* **2017**, *22* (5), 14.
45. Gao, C. C.; Wang, Y.; Han, F. X.; Yuan, Z. Q.; Li, Q.; Shi, C.; Cao, W. W.; Zhou, P. H.; Xing, X. D.; Li, B., Antibacterial activity and osseointegration of silver-coated poly(ether ether ketone) prepared using the polydopamine-assisted deposition technique. *Journal of Materials Chemistry B* **2017**, *5* (47), 9326-9336.

46. Wu, J. J.; Yu, C.; Li, Q. L., Novel regenerable antimicrobial nanocomposite membranes: Effect of silver loading and valence state. *Journal of Membrane Science* **2017**, *531*, 68-76.
47. Wang, J. Q.; Wu, Y. C.; Yang, Z.; Guo, H.; Cao, B.; Tang, C. Y. Y., A novel gravity-driven nanofibrous membrane for point-of-use water disinfection: polydopamine-induced in situ silver incorporation. *Scientific Reports* **2017**, *7*, 8.
48. Song, Y. Y.; Jiang, H. J.; Wang, B. B.; Kong, Y.; Chen, J., Silver-Incorporated Mussel-Inspired Polydopamine Coatings on Mesoporous Silica as an Efficient Nanocatalyst and Antimicrobial Agent. *Acs Applied Materials & Interfaces* **2018**, *10* (2), 1792-1801.
49. Li, Y. Z.; Wang, B. J.; Sui, X. F.; Xie, R. Y.; Xu, H.; Zhang, L. P.; Zhong, Y.; Mao, Z. P., Durable flame retardant and antibacterial finishing on cotton fabrics with cyclotriphosphazene/polydopamine/silver nanoparticles hybrid coatings. *Applied Surface Science* **2018**, *435*, 1337-1343.
50. Liu, L. Y.; Cai, R.; Wang, Y. J.; Tao, G.; Ai, L. S.; Wang, P.; Yang, M. R.; Zuo, H.; Zhao, P.; He, H. W., Polydopamine-Assisted Silver Nanoparticle Self-Assembly on Sericin/Agar Film for Potential Wound Dressing Application. *International Journal of Molecular Sciences* **2018**, *19* (10), 16.
51. Yang, E.; Alayande, A. B.; Kim, C. M.; Song, J. H.; Kim, I. S., Laminar reduced graphene oxide membrane modified with silver nanoparticle-polydopamine for water/ion separation and biofouling resistance enhancement. *Desalination* **2018**, *426*, 21-31.
52. Cordes, A. L.; Merkel, D. R.; Patel, V. J.; Courtney, C.; McBride, M.; Yakacki, C. M.; Frick, C. P., Mechanical characterization of polydopamine-assisted silver deposition on thiol-ene polymer substrates. *Surface & Coatings Technology* **2019**, *358*, 136-143.
53. Guan, M.; Chen, Y. M. F.; Wei, Y.; Song, H.; Gao, C. H.; Cheng, H.; Li, Y.; Huo, K. F.; Fu, J. J.; Xiong, W., Long-lasting bactericidal activity through selective physical puncture and controlled ions release of polydopamine and silver nanoparticles-loaded TiO₂ nanorods in vitro and in vivo. *International Journal of Nanomedicine* **2019**, *14*, 2903-2914.
54. Shang, B.; Xu, M.; Zhi, Z. L.; Xi, Y. W.; Wang, Y. B.; Peng, B.; Li, P.; Deng, Z. W., Synthesis of sandwich-structured silver@polydopamine@silver shells with enhanced antibacterial activities. *Journal of Colloid and Interface Science* **2020**, *558*, 47-54.
55. Orishchin, N.; Crane, C. C.; Brownell, M.; Wang, T. J.; Jenkins, S.; Zou, M.; Nair, A.; Chen, J. Y., Rapid Deposition of Uniform Polydopamine Coatings on Nanoparticle Surfaces with Controllable Thickness. *Langmuir* **2017**, *33* (24), 6046-6053.
56. Krishnamurthi, V. R.; Rogers, A.; Peifer, J.; Niyonshuti, II; Chen, J. Y.; Wang, Y., Microampere Electric Current Causes Bacterial Membrane Damage and Two-Way Leakage in a Short Period of Time. *Applied and Environmental Microbiology* **2020**, *86* (16), 10.

57. Zhang, Q. A.; Li, W. Y.; Wen, L. P.; Chen, J. Y.; Xia, Y. N., Facile Synthesis of Ag Nanocubes of 30 to 70 nm in Edge Length with CF₃COOAg as a Precursor. *Chemistry-a European Journal* **2010**, *16* (33), 10234-10239.
58. Brewster, J. D., A simple micro-growth assay for enumerating bacteria. *Journal of Microbiological Methods* **2003**, *53* (1), 77-86.
59. Haque, M. A.; Imamura, R.; Brown, G. A.; Krishnamurthi, V. R.; Niyonshuti, II; Marcelle, T.; Mathurin, L. E.; Chen, J. Y.; Wang, Y., An experiment-based model quantifying antimicrobial activity of silver nanoparticles on Escherichia coli. *Rsc Advances* **2017**, *7* (89), 56173-56182.
60. Schneider, C. A.; Rasband, W. S.; Eliceiri, K. W., NIH Image to ImageJ: 25 years of image analysis. *Nature Methods* **2012**, *9* (7), 671-675.
61. Schindelin, J.; Arganda-Carreras, I.; Frise, E.; Kaynig, V.; Longair, M.; Pietzsch, T.; Preibisch, S.; Rueden, C.; Saalfeld, S.; Schmid, B.; Tinevez, J. Y.; White, D. J.; Hartenstein, V.; Eliceiri, K.; Tomancak, P.; Cardona, A., Fiji: an open-source platform for biological-image analysis. *Nature Methods* **2012**, *9* (7), 676-682.
62. Stevenson, K.; McVey, A. F.; Clark, I. B. N.; Swain, P. S.; Pilizota, T., General calibration of microbial growth in microplate readers. *Scientific Reports* **2016**, *6*, 7.
63. Lemire, J. A.; Kalan, L.; Bradu, A.; Turner, R. J., Silver Oxynitrate, an Unexplored Silver Compound with Antimicrobial and Antibiofilm Activity. *Antimicrobial Agents and Chemotherapy* **2015**, *59* (7), 4031-4039.
64. Schweigert, N.; Zehnder, A. J. B.; Eggen, R. I. L., Chemical properties of catechols and their molecular modes of toxic action in cells, from microorganisms to mammals. *Environmental Microbiology* **2001**, *3* (2), 81-91.
65. Beamson, G.; Briggs, D., high-resolution monochromated x-ray photoelectron-spectroscopy of organic polymers - a comparison between solid-state data for organic polymers and gas-phase data for small molecules. *Molecular Physics* **1992**, *76* (4), 919-936.
66. An, T.; Lee, N.; Cho, H. J.; Kim, S.; Shin, D. S.; Lee, S. M., Ultra-selective detection of Fe²⁺ ion by redox mechanism based on fluorescent polymerized dopamine derivatives. *Rsc Advances* **2017**, *7* (49), 30582-30587.
67. Silverstein, R. M., Spectrometric Identification of Organic Compounds. 7th ed. ed.; Webster, F. X., Ed. Wiley, 2005.
68. Talbi, H.; Maarouf, E. B.; Humbert, B.; Alnot, M.; Ehrhardt, J. J.; Ghanbaja, J.; Billaud, D., Spectroscopic studies of electrochemically doped polyindole. *Journal of Physics and Chemistry of Solids* **1996**, *57* (6-8), 1145-1151.

69. Okuda, H.; Wakamatsu, K.; Ito, S.; Sota, T., Possible Oxidative Polymerization Mechanism of 5,6-Dihydroxyindole from A Initio Calculations. *Journal of Physical Chemistry A* **2008**, *112* (44), 11213-11222.
70. Stark, G., Functional consequences of oxidative membrane damage. *Journal of Membrane Biology* **2005**, *205* (1), 1-16.
71. Su, L.; Yu, Y.; Zhao, Y. S.; Liang, F.; Zhang, X. J., Strong Antibacterial Polydopamine Coatings Prepared by a Shaking-assisted Method. *Scientific Reports* **2016**, *6*, 8.
72. Forooshani, P. K.; Polega, E.; Thomson, K.; Bhuiyan, M. S. A.; Pinnaratip, R.; Trought, M.; Kendrick, C.; Gao, Y. S.; Perrine, K. A.; Pan, L.; Lee, B. P., Antibacterial Properties of Mussel-Inspired Polydopamine Coatings Prepared by a Simple Two-Step Shaking-Assisted Method. *Frontiers in Chemistry* **2019**, *7*, 15.

3.7. Appendix A: Supporting Information

Table S1. Hydrodynamic diameter and ζ -potential measurements of surface-modified AgNPs.

Surface-modified AgNPs	Hydrodynamic diameter (nm) in water	ζ -potential (mV) in PBS pH = 7.4
PVP-AgNPs	121.7 \pm 4.0	-8.74 \pm 1.08
PDA5-AgNPs	119.6 \pm 2.4	-14.70 \pm 2.67
PDA15-AgNPs	186.3 \pm 2.0	-10.26 \pm 0.89
PDA30-AgNPs	209.3 \pm 4.7	-9.52 \pm 0.22
DA-AgNPs	113.1 \pm 1.9	-12.14 \pm 1.97

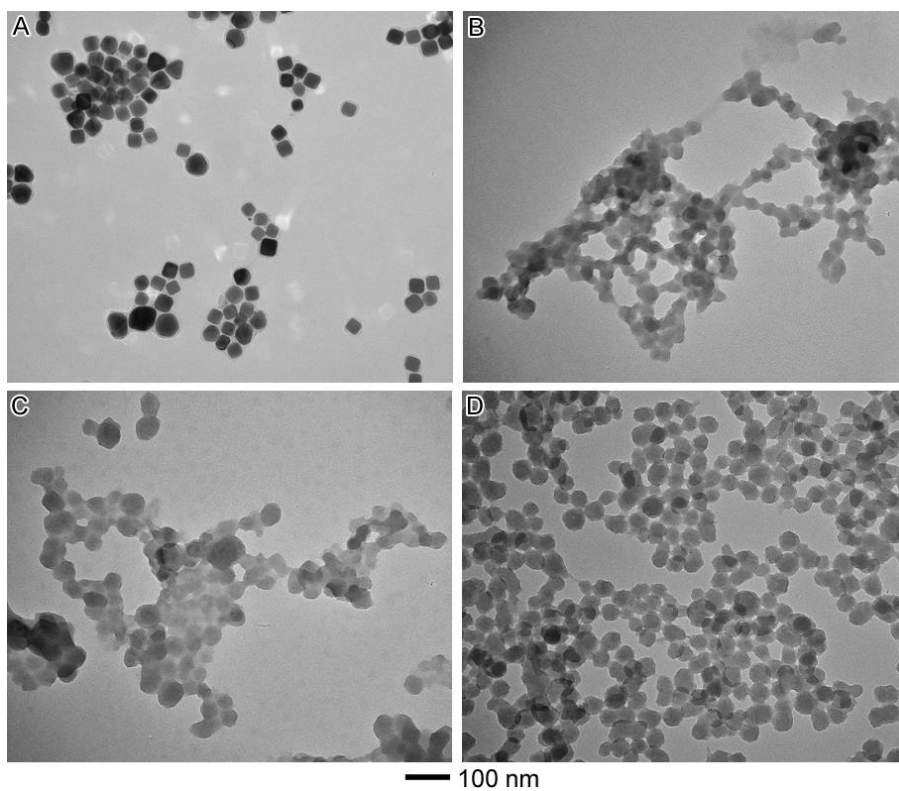


Figure S1. TEM characterization of DA-AgNPs (A) and PDA nanoparticles obtained at different reaction times, 5, 15, and 30 min, respectively, denoted as PDA5 (B), PDA (C), and PDA30 (D).

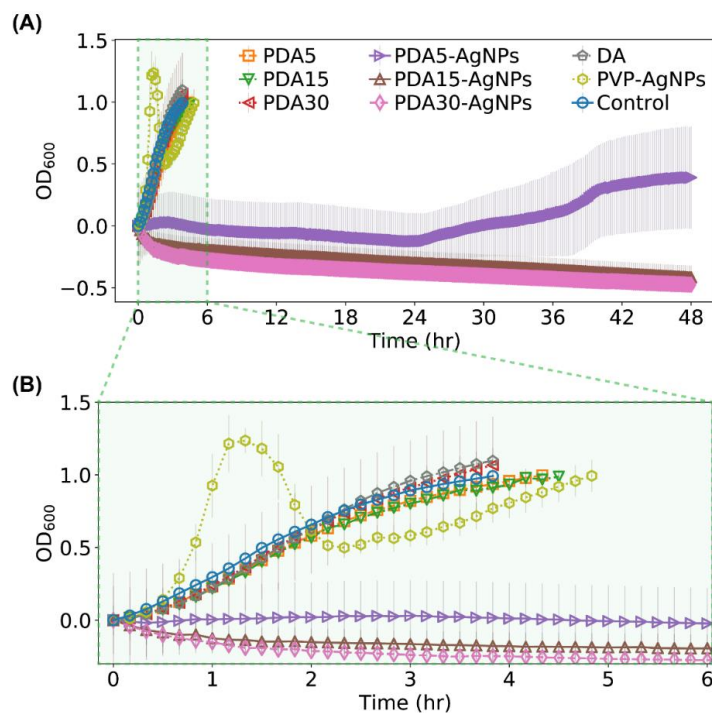


Figure S2. Truncated and vertically shifted OD growth curves for bacteria treated with PDA, PDA-AgNPs, DA and PVP-AgNPs: (A) full region of 48 h incubation; and (B) zoom-in region of 0-6 h incubation.

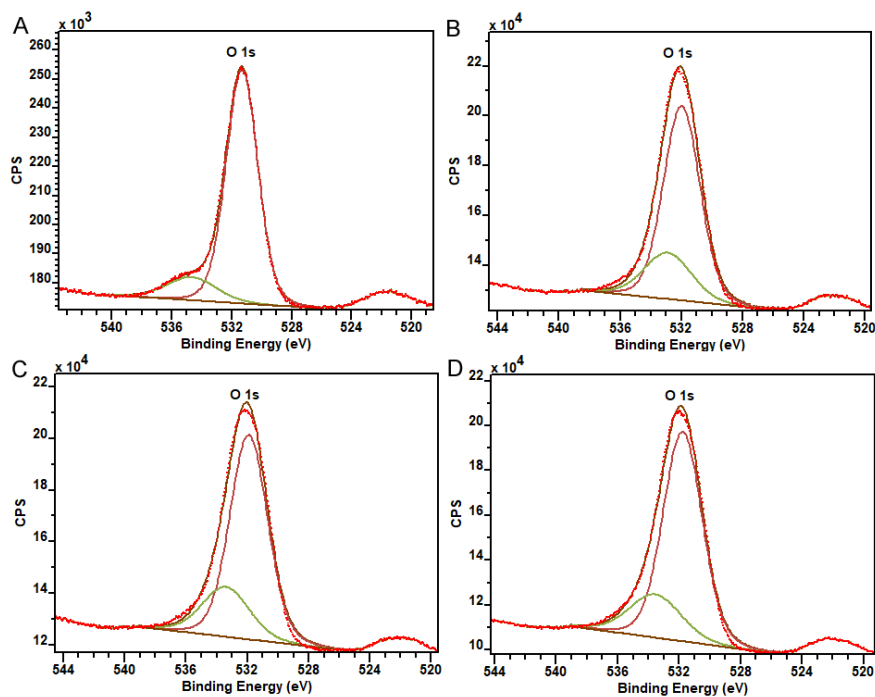


Figure S3. XPS deconvoluted spectra of O 1s for different samples: (A) PVP-AgNPs; (B) PDA5-AgNPs; (C) PDA15-AgNPs; and (D) PDA30-AgNPs. The dotted lines (red) are the experimental data while the solid lines (dark brown) are the fitting sum after the linear background subtraction.

The solid lines in light brown and light green are the fitting C=O and C-OH components, respectively.

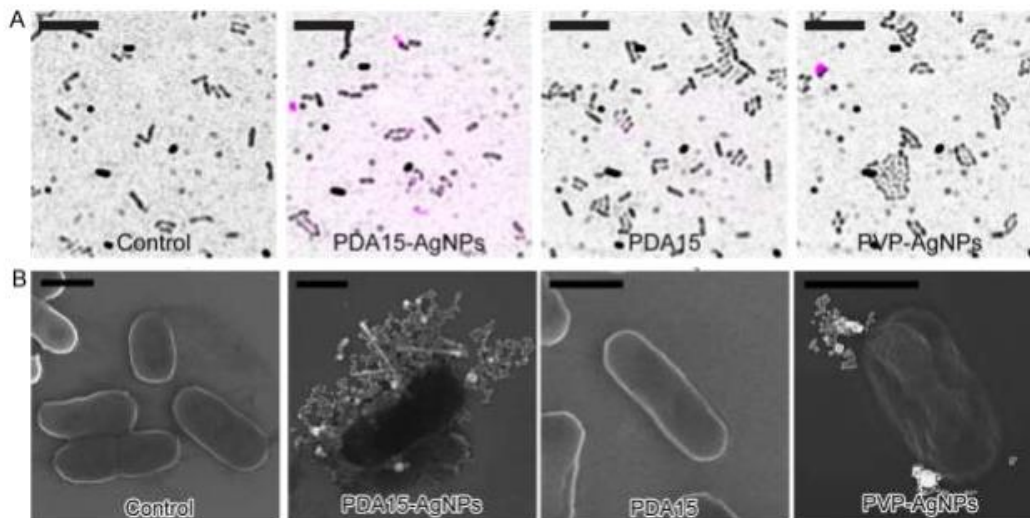


Figure S4. (A) Representative fluorescent images of nanoparticles (purple) on top of the bright images of bacteria (grayscale) treated with different conditions. Scale bar = 10 μm . (B) Representative SEM images of the bacteria treated with different conditions. Scale bar = 1 μm .

3.8. Appendix B: Surface Modification of AgNPs with different polymeric ligands for antimicrobial applications

3.8.1. Overview

In this study, AgNPs are surface modified with different polymer ligands through the ligand-exchange process to evaluate the effect of different ligands on stability and antimicrobial effectiveness of AgNPs against a gram-negative bacterium, *Escherichia Coli*. AgNPs capped with polyvinylpyrrolidone (PVP-AgNPs) are used as a template for ligand exchange process to other polymers. The impact of PVP, polyethyleneimine (PEI) and thiol-polyethylene glycol (PEG) as surface ligands on AgNPs stability was evaluated. Stability studies aimed to characterize the changes in chemical and physical properties of the AgNPs over time and assess how these

properties are changed regarding their surface ligands. Measurements of surface charges of the nanoparticles was accomplished using zeta potential to verify the success of ligand-exchange process. Modification of the surface of AgNPs is targeted to increase surface interaction of silver with other molecules such as cells, which will open more opportunity for application of AgNPs in biomedicine.

3.8.2. Introduction

Different methods of modifying AgNPs surface have been studied to enhance their antimicrobial properties. For instance, bioinspired morphology controlled AgNPs were fabricated using phytochemicals of *Elaeagnus umbellate* extract used as reducing and capping agents for shape and size control that make monodisperse spherical NPs with better antimicrobial property.¹ Polymers such as PEG, when they replace the conventional ligand, PVP the nanoparticles physicochemical properties are changed, thus their functions to meet desired applications. Polymeric ligands can give the nanoparticles the ability to stick to the surface of the cell. AgNPs interaction with the cells or surface of the targeted molecule, NP-target interaction can be enhanced by attaching cell-specific ligand on NPs, such as PEI to enhance cell binding and uptake of NPs via different mechanisms.^{2,3} Morphological control of the AgNPs which often involves the use of surface ligands has contributed to more understanding of their antimicrobial behaviors.⁴ In this study we evaluated the changes in properties of AgNPs of three ligands, namely, PVP, PEG and branched PEI using UV-Vis spectroscopy and TEM in water and PBS buffer media. The storage condition of these capped AgNPs were evaluated using UV/Vis.

3.8.3. Experimental methods, ligand exchange methods for surface modification of AgNPs with different polymeric ligands

3.7.3A. Surface modification of Ag nanoparticles with Polyethyleneimine (PEI-AgNPs)

PEI-AgNPs were prepared using a ligand exchange process illustrated in **Figure S5**. Typically, 1.5 mL of 5 nM (3.0×10^{12} particles/mL) PVP-AgNPs prepared using the procedure described in section 3.3.1 were added to 5 mL of water containing 2.7 mg of PEI ($M_w \sim 1,800$) solution at 1:300,000 molar ratio of AgNP-PVP to PEI. The reaction mixture was incubated for about 1 h at room temperature under magnetic stirring. After incubation, the product was purified with water 3 times to remove excess PEI and collected by centrifugation at 14,000 rpm for 30 minutes. The nanoparticles were then dispersed in water for further characterization and future use. The same protocol was used to modify the surface of Ag nanoplates that was produced with a modified protocol described in chapter 4 of this text.

3.7.3B. Synthesis of AgNPs coated with Polyethylene glycol thiol (PEG-AgNPs)

In a typical ligand-exchange reaction, 7.5 mg of PEG ($MW=5,000$ g/mol) was mixed with 1.5 mL of pre-prepared PVP-AgNPs (5 nM, 3.0×10^{12} particles/mL) in a 5 mL total volume. The reaction was incubated for 2 h at room temperature under magnetic stirring. The obtained nanoparticles were collected via centrifugation at 6500 rpm for 15 min, and then washed three times with deionized water to remove excess dopamine. The final product was re-dispersed in water and stored. The molar ratios between AgNPs and PEG was kept to 1:300,000 for all the nanoparticles.

3.8.4. Part 1: Results and Discussion

3.8.4.1. Surface modification of Ag nanoparticles with different surface ligands

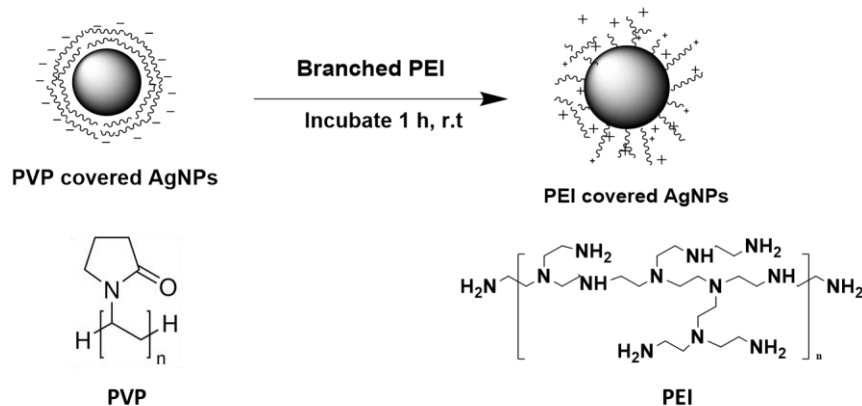


Figure S5: Schematic representation of ligand-exchange process to make PEI-AgNPs.

The PVP-AgNPs were synthesized through the established polyol method as described in 3.3.1, while the PEI-AgNPs were prepared by a ligand-exchange process as described and illustrated in **Figure S5**. The UV-vis spectra recorded before and after the ligand exchange process shows a 13 nm blue shift in the localized surface plasmon resonance (LSPR) peak of AgNPs from 423 nm for the PVP-AgNPs to 410 nm for the PEI-AgNPs (**Figure S6A**). PEG-AgNP peak does not shift compared to PVP-AgNP. The size of the PVP-AgNPs was measured based on the TEM image in **Figure S6A**, having an average edge length of 37.6 ± 4.0 nm. After the ligand exchange process, the resultant PEI-AgNPs were found to slightly decrease in size (35.2 ± 3.1 nm) while PEG-AgNPs is 45.3 ± 2.4 nm. The morphological change agrees with the observed LSPR blue shift of the PEI-AgNPs compared to PVP-AgNPs because truncated particles could shift the LSPR to shorter wavelength compared to their counterparts with sharp corners. The hydrodynamic diameter of the PVP-AgNPs was measured to be 126.2 nm. The PVP-AgNPs were negatively charged with zeta potential of -39.4 ± 1.37 mV (**Table S2**). The hydrodynamic diameter of the

PEI-AgNPs slightly increased to 169.2 nm with a higher PDI of 0.23, perhaps due to the presence of particle aggregation. The zeta potential of PEI-AgNPs was measured to be $+15.68 \pm 1.80$ mV at pH=7, indicative of a positively charged surface, and thus confirming a successful surface ligand exchange from PVP to PEI (**Table S2**). PEG-AgNP show negative charge of -16.94 ± 1.05 mV indicative of the negative charge from thiol. Ag nanoplates of different surface ligands showed the same trend (**Figure S7**).

The ligand exchange reaction to make different surface of both Ag nanocubes and Ag nanoplates were successful as suggested by characterization techniques. It was hard to distinguish between different surfaces using TEM to know if ligand-exchange was successful for PEG, PEI and PVP-AgNPs (**Figures S6 and S7**), so zeta potential was used to measure surface charges. As expected, PVP, PEG and PDA nanoparticles are negatively charged while PEI coated nanoparticles are positively charged. Zeta potential of the PVP-AgNP is negative, which agrees with the literature because PVP,⁵ used a capping agent is negatively charged. DLS and zeta potential results suggest a successful ligand exchange for three ligands and PDA deposition was obviously achieved from TEM images (**Figure 1C-E**).

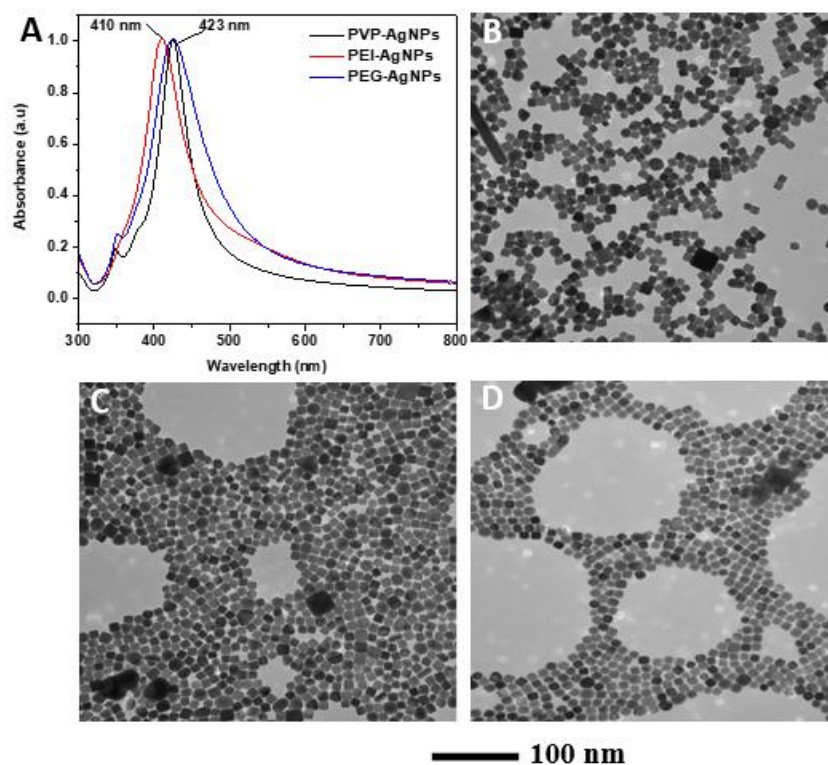


Figure S6: (A) UV/Visible spectra of AgNPs with different ligands (PEG, PEI and PVP). (B) TEM images of PVP-AgNPs. (C) TEM image representation of PEI-AgNPs and (D) TEM image representation of SH-PEG-AgNPs.

Table S2: Hydrodynamic diameter and Zeta Potential of Ag nanocubes with different ligands.

AgNPs of different surface ligands	Hydrodynamic diameter (nm)	Zeta potential (mV)
PVP-AgNPs	126.0 ± 3.3	-39.4 ± 1.37
PEI-AgNPs	169.2 ± 2.6	$+15.68 \pm 1.80$
PEG-AgNPs	174.5 ± 1.8	-16.94 ± 1.05

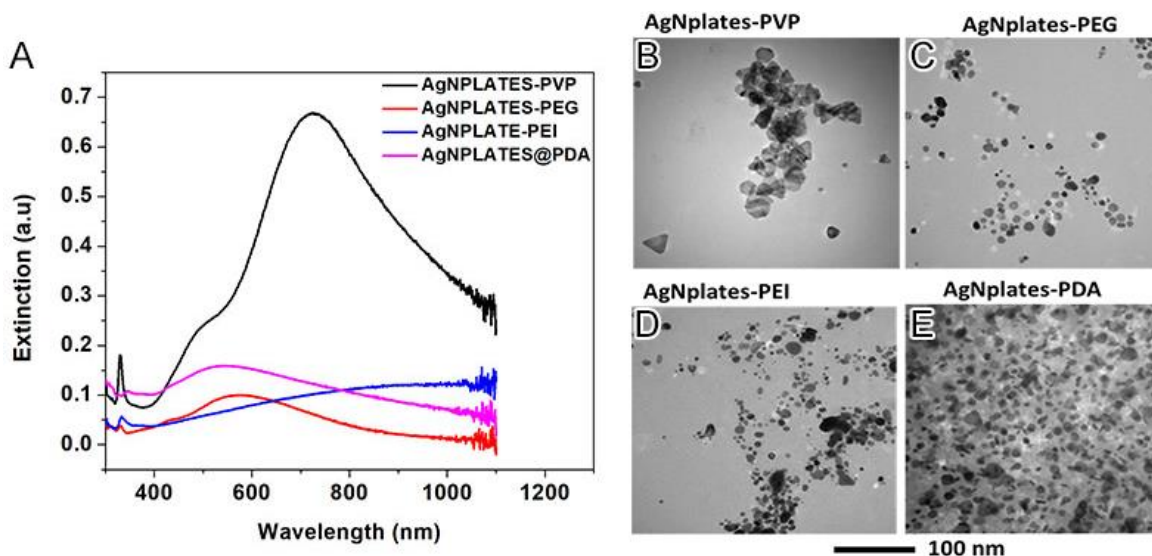


Figure S7: Silver nanoplates of different surfaces. A. UV-Vis spectra, B-E TEM images of Ag nanoplates of different polymeric surface ligands.

Table S3: Hydrodynamic diameter and Zeta potential measurements of Ag nanoplates of different surfaces.

Ag Nanoplates	Hydrodynamic diameter (nm)	Zeta Potential (mV)
PVP-Ag Nanoplates	60.3	-28.12 ± 1.26
PEG-Ag Nanoplates	58.9	-10.16 ± 2.32
PEI-Ag Nanoplates	254.0	+10.81 ± 1.07
PDA-Ag Nanoplates	264.1	-38.05 ± 2.17

3.8.4.2. Antimicrobial evaluation of PEI-AgNPs and PVP-AgNPs*

*Published: Alqahtany, M.; Khadka, P.; Niyonshuti, I.; Krishnamurthi, V. R.; Sadoon, A. A.; Challapalli, S. D.; Chen, J. Y.; Wang, Y., Nanoscale reorganizations of histone-like nucleoid structuring proteins in *Escherichia coli* are caused by silver nanoparticles. *Nanotechnology* **2019**, *30* (38), 14.

Ligand exchange was used to successfully produce AgNP and PEI-AgNPs that was used to test the effect on surface charge on antimicrobial activity of AgNPs. Super-resolution fluorescence

microscopy reveals that Histone-like nucleoid structuring (H-NS) proteins reorganize in *E. coli* bacteria in presence of AgNPs (**Figure S2 in reference 25**).⁶

3.9. Conclusion

Methods of surface modification were developed, and four polymer ligands were used to modify the surface of Ag nanocubes and Ag nanoplates. Ligand-exchange process was monitored by zeta potential measurements to see the changes on the AgNPs surface charge. PEI-AgNPs and PEG-AgNPs were used to evaluate the antimicrobial activity against *E. coli* and results are reported in Meead et al 2019.⁶ The results from this paper showed particle-specific effect of AgNPs as PEI-AgNPs showed more effect leading to larger reorganization of H-NS proteins. The super resolution fluorescence microscopy revealed the particle-specific effect of AgNPs. ⁶

3.10. References

1. H. Liu, X. Qu, E. Kim, M. Lei, K. Dai, X. L. Tan, M. Xu, J. Y. Li, Y. P. Liu, X. W. Shi, P. Li, G. F. Payne, and C. S. Liu, *Biomaterials*, 2018, **162**, 109-122.
2. B. J. Yuan, M. H. Sui, J. Qin, J. Y. Wang, and H. T. Lu, *Journal of Colloid and Interface Science*, 2019, **539**, 297-305.
3. Y. M. Long, L. G. Hu, X. T. Yan, X. C. Zhao, Q. F. Zhou, Y. Cai, and G. B. Jiang, *International Journal of Nanomedicine*, 2017, **12**, 3193-3206.
4. X. F. Tian, Y. P. Li, S. K. Wan, Z. Q. Wu, and Z. W. Wang, *Journal of Nanomaterials*, 2017, **2017**, 9.
5. M. Baalousha, *Nanoimpact*, 2017, **6**, 55-68.
6. M. Alqahtany, P. Khadka, I. Niyonshuti, V. R. Krishnamurthi, A. A. Sadoon, S. D. Challapalli, J. Y. Chen, and Y. Wang, *Nanotechnology*, 2019, **30**(38), 14.

3.11. Appendix C. Effects on stability of AgNPs with different polymeric ligands

3.11.1. Overview

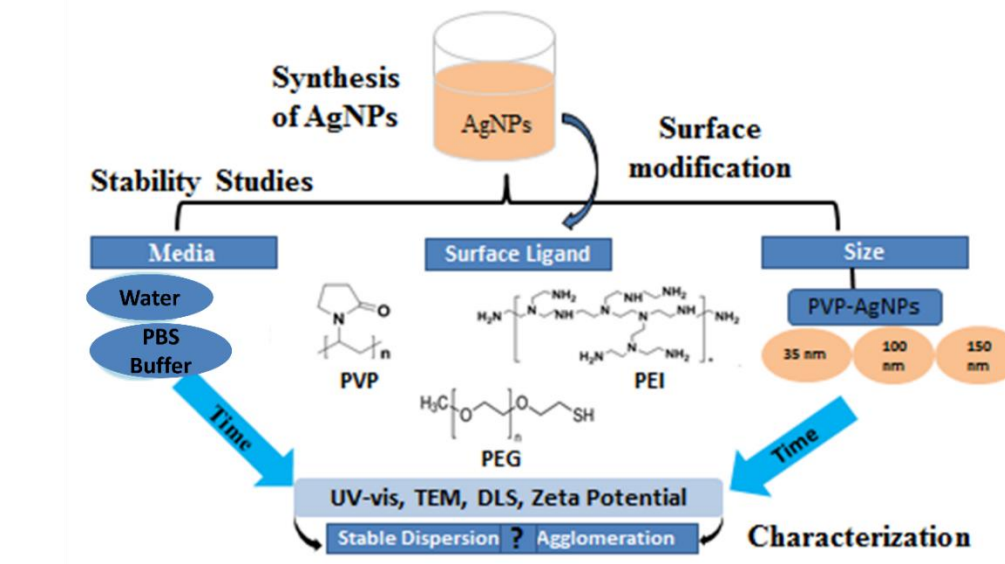


Figure S8: Experimental setup for stability evaluation of differently coated AgNPs in different media. Size effect is also evaluated for PVP-coated AgNPs using UV-Vis spectrophotometer, TEM, and DLS.

3.11.2. Introduction

Metal nanoparticles tend to aggregate in aqueous solution especially in the biological medium due to their high reactivity with biomolecules. Stability of AgNPs depends on inter-particle behaviors from intermolecular and surface forces and these behaviors can be affected by surface chemistry, storage conditions, and type of solvent.¹⁻¹¹ Antibacterial capacity of Ag-NP depends on the surface oxidation, since the NPs act as carriers of Ag^+ chemisorbed that cause the antimicrobial activity.¹² A little research has been done on understanding the effects on the colloidal stability of AgNPs that is known to depend on medium composition, size of the nanoparticles and presence of capping agents. Therefore, there is still a need to understand how these factors contribute to the stability of AgNPs. Besides controlling size and stability of AgNPs,

functional groups on polymeric ligands provide control over surface chemistry. The traditional surfactant, PVP is replaced by other ligands to prevent toxicity and other polymeric ligands such as PEG with various side chains and PEI can be used to meet desired functions of the nanoparticles. A cytotoxicity assay showed that PEI-AgNCs exhibit relatively lower cytotoxicity compared to other studied ligands.^{2, 10, 13, 14} Thus, they are exchanged with PVP to meet applications for cellular interactions.

3.11.3. Experimental Methods

3.10.3A. Effect on storage conditions on stability of AgNPs

Storage conditions are important key for stability of the nanoparticles are they predict how they interact with the media. Lyophilization effect was evaluated on the nanoparticles' stability. AgNPs capped with different ligands were lyophilized and dissolved in water. Then, UV/Vis spectrophotometer was used to track the changes in nanoparticles properties. The hypothesis was that lyophilization might help nanoparticles to stay intact and so there is less changes in chemical properties overtime which could ensures their stability.

3.10.3B. Effect of surface ligands on stability of AgNPs

Physiochemical properties of media determine kinetics of aggregation of the nanoparticles in solution. PBS buffer was used to see how the nanoparticles behaves in physiological conditions (pH 7.4) at room temperature which is relevant for nanoparticles intended applications as antibacterial agents. For instance, buffer concentration is one of the factors that guides aggregation.⁹ The nanoparticles of different ligands were incubated in PBS for 3 days and their LSPR peaks were monitored using UV/vis spectrometry overtime. TEM images of the AgNPs were taken before incubating the nanoparticles in buffer and after incubation for 3 days.

3.10.3C. Effect of size of AgNPs on their stability in PBS

Different sizes of Ag nanocubes ranging from 30 to 150 nm were studied. Since the size has an impact on nanoparticles chemical stability and dispersion stability in the media. Three different edge lengths (35nm, 105 nm, and 150 nm PVP-AgNPs) were evaluated for stability in physiological conditions.

3.12. Part 2: Results and Discussion

Effect of surface ligand on stability

UV-vis spectrophotometry and DLS were used to measure the change in optical properties and size distribution. PVP-capped AgNPs were most stable followed by PEG-AgNPs over 15 days compared to PEI-AgNPs under physiologically appropriate conditions (pH 7). In addition, hydrodynamic diameter and PDI values decreased overtime for PVP-AgNP and PEI-AgNPs suggesting etching of these particles in PBS overtime (**Figures S9 and S10**). In addition, PEI-AgNC showed an increase in baseline overtime and very high decrease in hydrodynamic diameter indicating dissolution of Ag⁺ ions from the suspension and etching (**Table S5**).¹⁵ For PEG-AgNPs there was no significant change in PDI and hydrodynamic diameter values (**Table S6**). Hydrodynamic diameters of these nanoparticles suggest no aggregation. Taking the results all together suggested that PVP-AgNPs are stable for with slight decrease in size as shown by UV-vis spectra. PEI-AgNPs may experience more dissolution of Ag⁺ ion in PBS over 15 days making them the least stable compared to PEG and PVP capped AgNPs. Stability of nanoparticles capped with polymeric ligands have been related to the steric repulsion effects of the ligands adsorbed on the surface of the particles.² Further understanding of the effects on the stability of AgNPs will not

only give insights on how to enhance the AgNPs performance in biomedicine, but also address the concern that is posed by these materials to environmental and human communities.

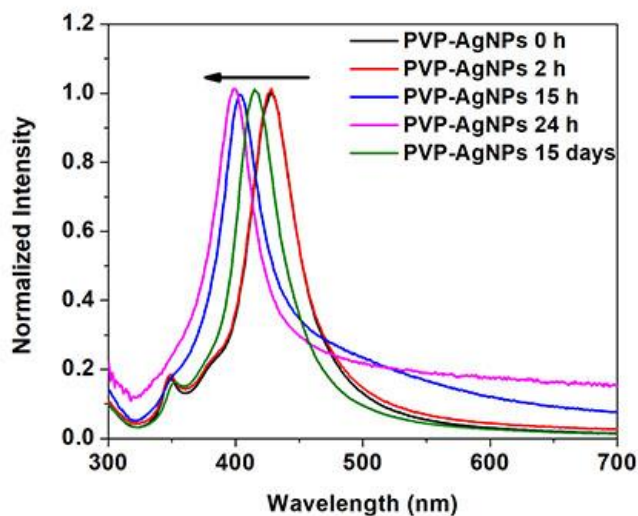


Figure S9: UV/Vis spectra of PVP-AgNPs taken at different storage times in PBS at pH 7.4.

Table S4: Hydrodynamic and Zeta potential measurements of PVP-AgNPs at different incubation time points.

AgNP-PVP in PBS at different incubation time points (hr)	Hydrodynamic Diameter (nm)	PDI
2	198.6 ± 2.6	0.204
15	192.8 ± 1.4	0.199
24	195.2 ± 1.8	0.216
360	182.4 ± 2.4	0.245

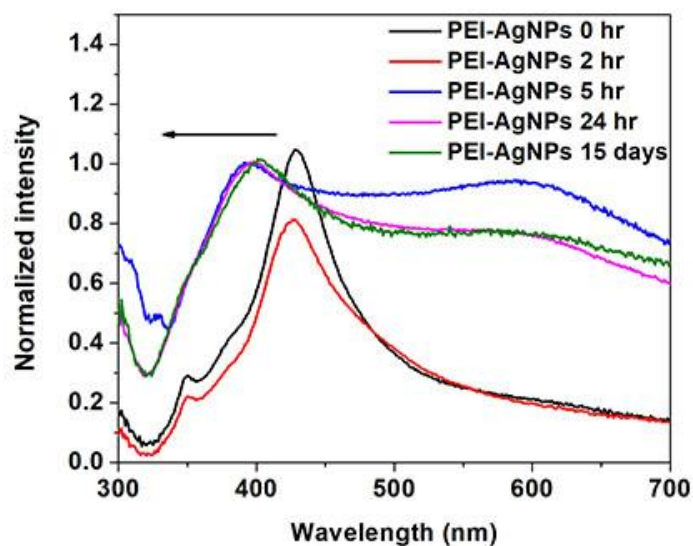


Figure S10: UV-Vis spectra of PEI-AgNPs taken at different storage times in PBS at pH 7.4.

Table S5: PEI-AgNPs at different incubation time points showing DLS and Zeta potential measurements.

PEI-AgNPs in PBS at different incubation time points (hr)	Hydrodynamic Diameter (nm)	PDI
2	777.1 ± 30.8	0.337
5	604.3 ± 9.1	0.329
24	559.0 ± 12.6	0.290
360	301.4 ± 30.4	0.393

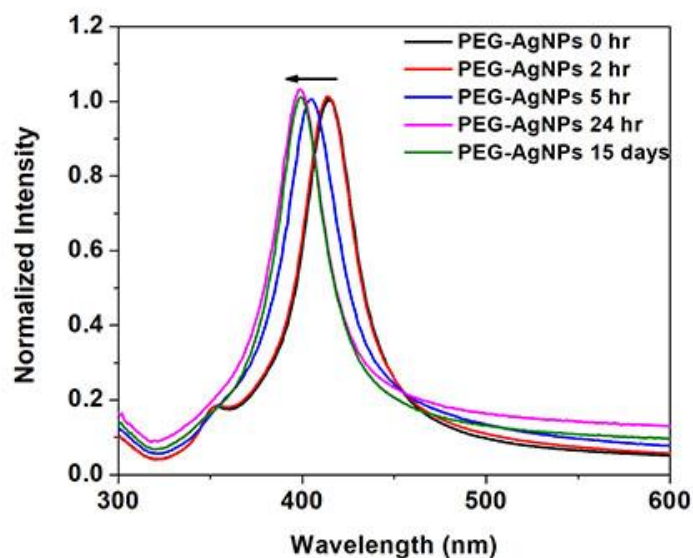


Figure S11: UV/Vis spectra of PEG-AgNPs taken at different storage times in PBS at pH 7.4.

Table S6: PEI-AgNPs at different incubation time points showing DLS and Zeta potential measurements.

AgNP-PEG in PBS at different incubation time points (hr)	Hydrodynamic Diameter (nm)	PDI
2	201.1 ± 1.3	0.218
5	211.3 ± 1.5	0.194
24	190.4 ± 0.8	0.244
360	201.4 ± 6.3	0.231

Effect of storage condition on stability of AgNPs with different surface ligands

We seek to better understand the stability and effect of storage conditions on AgNPs. The nanoparticles were stored in aqueous medium and in powder form after being lyophilized. Lyophilization did not a significant effect on peak symmetry of PVP-AgNP, however PEI-AgNPs and PEG-AgNPs showed broader peaks after lyophilization compared to before lyophilization.

The peak broadening observed for some particles after lyophilization suggests some aggregation. The aggregation and loss of efficacy observed when AgNPs were subjected to freeze-drying has also been observed by Rebecca L.R et al.¹⁶

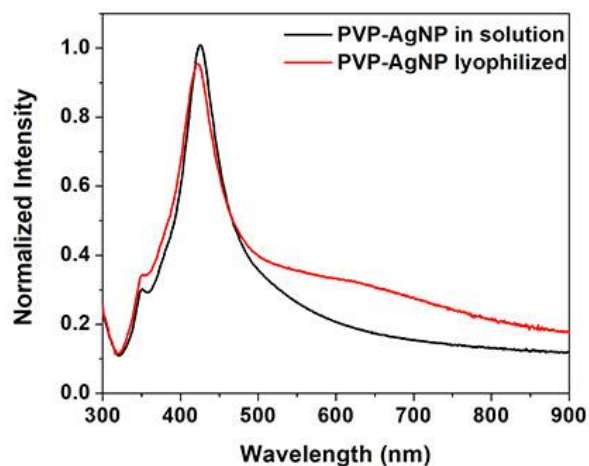


Figure S12: UV/Vis spectra of PVP-AgNPs stored in solution and in powder form.

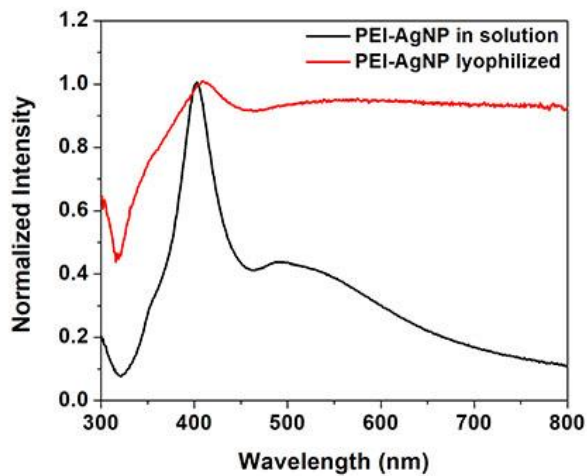


Figure S13: UV/Vis spectra of PEI-AgNPs stored in solution and in powder form.

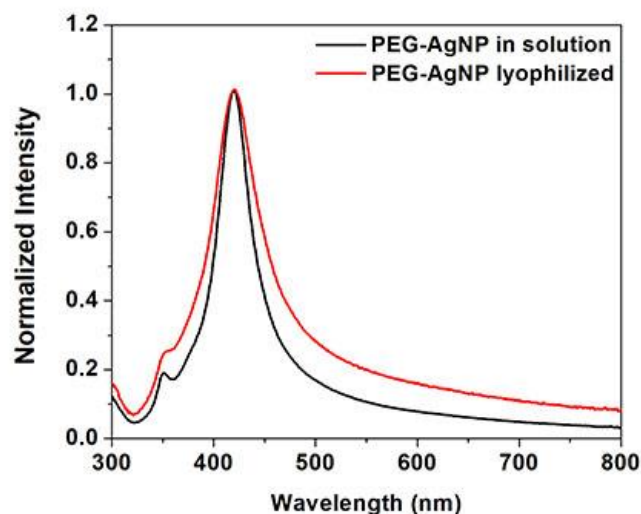


Figure S14: UV/Vis spectra of PEG-AgNPs stored in solution and in powder form.

Effect of size on stability of PVP-AgNPs

Stability of AgNPs of three different sizes was evaluated in PBS for 72 hours. The UV-vis spectra show blue shifts for all AgNPs which was confirmed by TEM. The sizes of the nanoparticles decreased to 33.9 nm, 91.1 nm, and 108 nm for 35 nm AgNPs, 105 nm and 150 nm AgNPs, respectively (**Figure S15 C, F, I**). The 150 nm AgNPs showed much reduced size in phosphate buffer compared to smaller AgNPs. UV-Vis and TEM data suggest etching of the PVP-AgNPs in PBS buffer and size dependency of these nanoparticles' behaviors.

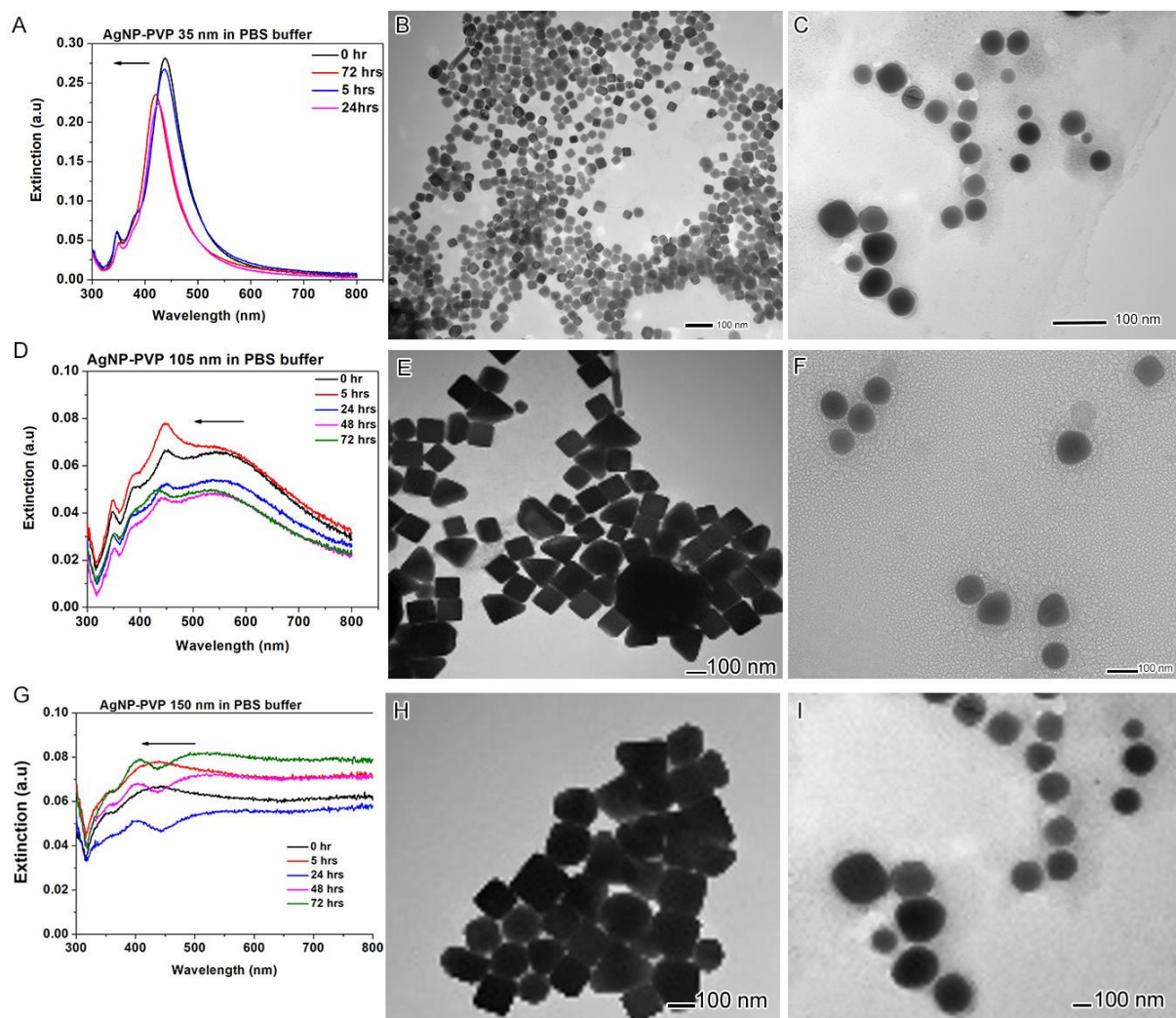


Figure S15: Size dependent stability of PVP-coated AgNP (AgNP-PVP) of different sizes. A) UV/vis spectra of AgNP-PVP with edge length of 35 nm in PBS over 3 days. TEM image of 35 nm AgNPs B) in water and C) after incubated in PBS for 3 days. D. UV/vis spectra of AgNP-PVP with edge length of 105 nm in PBS over 3 days. TEM image of 105 nm AgNPs E) in water and F) after incubated in PBS for 3 days. G) UV/vis spectra of AgNP-PVP with edge length of 150 nm in PBS over 3 days. TEM image of 150 nm AgNPs H) in water and I) after incubated in PBS for 3 days.

3.12. References

1. A. V. Plyushchenko, K. A. Mitusova, L. N. Borovikova, A. I. Kipper and O. A. Pisarev, *Optics and Spectroscopy*, 2018, **125**, 243-248.
2. K. Afshinnia, M. Sikder, B. Cai and M. Baalousha, *Journal of Colloid and Interface Science*, 2017, **487**, 192-200.
3. K. Afshinnia and M. Baalousha, *Science of the Total Environment*, 2017, **581**, 268-276.
4. M. Baalousha, *Nanoimpact*, 2017, **6**, 55-68.
5. O. A. Baranova, S. D. Khizhnyak and P. M. Pakhomov, *Journal of Structural Chemistry*, 2016, **57**, 1203-1208.
6. I. Capjak, M. Z. Avdicevic, M. D. Sikiric, D. D. Jurasin, A. Hozic, D. Pajic, S. Dobrovic, W. Goessler and I. V. Vrcek, *Environmental Science-Water Research & Technology*, 2018, **4**, 2146-2159.
7. I. Fernando and Y. Zhou, *Chemosphere*, 2019, **216**, 297-305.
8. M. H. Jang, S. J. Bae, S. K. Lee, Y. J. Lee and Y. S. Hwang, *Journal of Nanoscience and Nanotechnology*, 2014, **14**, 9665-9669.
9. S. V. Kapranov and V. I. Ryabushko, *Journal of Nanoparticle Research*, 2018, **20**, 15.
10. M. Tejamaya, I. Romer, R. C. Merrifield and J. R. Lead, *Environmental Science & Technology*, 2012, **46**, 7011-7017.
11. Y. N. Yang, S. M. Xu, G. M. Xu, R. Liu, A. Xu, S. P. Chen and L. J. Wu, *Science of the Total Environment*, 2019, **647**, 1088-1096.
12. L. E. Valenti and C. E. Giacomelli, *Journal of Nanoparticle Research*, 2017, **19**, 9.
13. S. H. Lin, Y. W. Cheng, J. Liu and M. R. Wiesner, *Langmuir*, 2012, **28**, 4178-4186.
14. G. K. Wang, C. L. Yan, S. Y. Gao and Y. F. Liu, *Materials Science & Engineering C-Materials for Biological Applications*, 2019, **103**, 11.
15. Y. J. Xiong, M. Brunson, J. Huh, A. R. Huang, A. Coster, K. Wendt, J. Fay and D. Qin, *Small*, 2013, **9**, 2628-2638.
16. R. L. Ball, P. Bajaj and K. A. Whitehead, *International Journal of Nanomedicine*, 2017, **12**, 305-315.

Chapter IV: Towards understanding the antimicrobial properties of silver/gold alloy nanocages against *Escherichia coli**

4.1. Abstract

Silver nanoparticles are known for their great antimicrobial properties. Part of their antimicrobial activity comes from the leach of silver ions; however, the leached silver ions can complex with organic species causing cytotoxic effects above threshold concentration. Controlling the release of Ag^+ ions can enhance the selective eradication of bacteria but alleviate the cytotoxicity of leached silver ion due to the presence of organic species in biological environment. In this work, we studied Ag-Au nanocages (Ag-AuNCs) of different molar ratios to understand the effect of molar composition on the antimicrobial properties of Ag-AuNCs compared to pure AgNPs. The antimicrobial activity of the Ag-AuNCs of different molar ratios were evaluated on *Escherichia coli* (*E. coli*) using fluorescence-based growth curves. The antimicrobial data revealed that Ag-AuNCs 600 nm (75 at % Ag and 25 at% Au) and Ag-AuNCs 700 nm (46 at % Ag and 53 at% Au) exhibited higher antimicrobial activity than pure AgNPs and Ag-AuNCs of lower and higher Ag/Au molar ratios. This can be explained by the structural properties of these nanocages that allow more interactions of Ag atom with the bacteria or more release of Ag^+ ions. The mechanisms of greater antimicrobial activity of Ag-AuNCs are being investigated with more in-depth studies on the nanoparticles' properties and their interactions with the bacteria at the molecular level. Findings from this study will provide insights of compositional and morphological effects on Ag-AuNPs' antimicrobial activity.

***To be submitted:** Isabelle I. Niyonshuti, Ariel Rogers, Sebastian Boysen, Yong Wang, and Jingyi Chen

4.2. Introduction

Silver nanoparticles (AgNPs) are long known for their antimicrobial activity that is often associated with their ability to release Ag^+ ions and destroy the intracellular mechanisms of the bacteria that eventually lead to cell death.^{1, 2} The role AgNPs in antimicrobial mechanisms was also studied and linked to the binding and destruction of the cell wall of the bacteria. Despite their excellent antimicrobial activity against a big range of bacteria, AgNPs and released Ag^+ ions from AgNPs have presented toxicity to some mammalian cells.³⁻⁷ The cytotoxicity of the AgNPs on human cells, is still controversial. Kaiser et al. elaborated on importance of media composition and chloride concentration on cytotoxicity observed on some human cells.⁸ Ag^+ ions released in presence of oxidative agents can form complex with organic component in the media that sediment and agglomerate in the media. Binding of highly reactive Ag^+ ions to electron donor groups such as amine groups of proteins are therefore transformed into Ag complexes with different bioavailability and toxicity. The cytotoxicity of Ag complexes that is mostly related to adverse effect on immune system and disturbance of gene expression pathways of the mammals cells can restrict their applications as antimicrobial agents.⁹⁻¹¹ Recently, different approaches have been taken to take advantage of AgNPs' excellent antimicrobial efficacy and widen its antimicrobial applications by controlling the release of Ag^+ ions. Adding gold (Au) core and shell to the AgNPs has proven to increase antimicrobial effect while reducing toxicity of related Ag-complexes.¹²⁻¹⁵ More commonly, Au and Ag alloy nanocages (Ag-AuNCs) have been used in antimicrobial applications both as delivery of antibiotics via photothermal therapy or activating as antimicrobial agents.¹⁶⁻²¹ Ag-AuNCs are synthesized through a simple galvanic replacement reaction that is driven by the electrochemical potential difference between Ag atoms and Au ions from Au precursor. During galvanic replacement reaction, Au is reduced and deposit on the surface of Ag

nanocubes (AgNCs) that are used as a template.²² Au deposits on the surface of AgNCs to make a thin shell as Ag get oxidized and diffuse making hollow structure of Ag-Au nanoshell. As more Au precursor is added, the nanobox structure is formed and more Ag dealloying from the walls in (111) facets makes nanocages.²²⁻²⁴ The excellent optical properties of Ag and chemical stability of Au give the Ag-AuNCs a lot of advantages over solid nanoparticles.²⁵ For instance, their LSPR peak can be tuned by controlling the thickness and porosity of the walls, which can be done by controlling molar ratio of Ag nanocubes and Au precursor.^{26, 27} The hollow interior and porous walls of the Ag-AuNCs give them unique properties and more advantage for different applications compared to just Ag nanoparticles or Au nanoparticles. In addition, increased biocompatibility with biomolecules, easy preparation, larger scattering and absorption, good mechanical flexibility, and stability as well as tunable optical properties associated with these alloy nanoparticles have made them favorable in diagnostics and therapeutic fields.^{23, 24, 28}

Most studies have focused on synthesis of Ag-AuNCs for delivery of antibiotic which is mostly due to photothermal effect.^{20, 29, 30, 31, 32} The application of Ag-AuNCs as antimicrobial agents has only been considered recently. Few studies have explored the antimicrobial activity of Ag-Au alloy nanostructures with limited knowledge on mechanisms used by these nanostructures at the molecular level.^{3, 33, 34} Wang et al. studied antimicrobial properties and mechanism of Au/Ag alloy nanocages where the right molar composition of the Ag/Au that give high antimicrobial effect was brought about. They suggested that high antimicrobial activity of nanocages could be associated with electronic effects of Ag when Au is present³⁵, possibility of more reactive Ag atoms as a result of electron withdrawal from less electronegative Ag atoms to Au atoms when Au is depositing on the surface creating Ag atoms with high free energy during galvanic replacement¹³, and the highly active Ag atoms on the surface of Ag-AuNCs after Ag is replaced

by Au as result of charge transfer created³, thus more interaction with bacteria. The mechanisms leading the antimicrobial properties of Ag-AuNCs were reactive oxygen species (ROS) generation, cell membrane disruption, and induction of cell apoptosis.³ Besides this study there is no other studies that has been able to decipher details on the mechanisms behind the great antimicrobial properties of Ag-AuNCs that seem to be dependent on Ag to Au ratio. In addition, it was recently found that Au and Ag exhibit synergistic effect on antimicrobial activity against *E. coli* with reduced cytotoxicity to human dermal fibroblast cells.³⁶ Adding Ag to AuNPs increased their antimicrobial activity that was based on ROS generation that was found to be higher for Ag-Au alloy nanostructures compared to pure AgNPs.³⁶⁻³⁸ There is a great need for studies that can explain the mechanisms leading to enhanced antimicrobial activity of Ag-AuNCs. Therefore, this work aims to explore the effect of molar ratio of Ag to Au in the Ag-AuNCs on their antimicrobial activity using a super-resolution fluorescence imaging. From the best of our knowledge this is the first study that focused on the effect of the molar composition of Ag and Au in the alloy nanocages to understand the mechanisms governing their antimicrobial activity.

4.3. Experimental methods

Chemicals and Materials: Silver trifluoroacetate (AgTFA), sodium hydrogen sulfide (NaHS), hydrochloric acid (HCl, 99.999%), Hydrogen tetrachloroaurate (III) trihydrate (HAuCl₄.3H₂O), diethylene glycol (DEG), sodium hydrogen sulfide (NaHS), Poly(vinylpyrrolidone) (PVP, MW = 55 000), silver tri-fluoroacetate (AgTFA.), and nitric acid (HNO₃, 99.999%) were purchased from Alfa Aesar. Poly(vinylpyrrolidone) (PVP, MW = 55 000) was purchased form Sigma-Aldrich. Ethylene glycol (EG) was purchased from J. T. Baker. Acetone was purchased from EMD. Ascorbic acid and sodium borohydride (NaBH₄) were

purchased from Sigma. Hexadecyltrimethylammonium chloride (CTAC) was purchased from TCI. 18 MΩ H₂O was used to carry out all the experiments. The chemicals were used as received.

4.3.1. Synthesis of Ag-Au alloy nanocages

Ag-AuNCs were synthesized using a modified protocol of galvanic replacement protocol that our lab previously established with modifications.²² First, Ag Nanocubes (AgNCs, edge length of 35 nm) were synthesized using a polyol method described earlier by Zhang et al.³⁹ During the protocol, 50 mL of EG was heated to 150 °C in a 250 mL round bottom flask while stirring at 300 rpm in an oil bath. When the temperature reached 150 °C, 0.6 mL of 3 mM NaHS in EG was added to the flask followed by 5 mL of 3 mM HCl in EG. After 2 minutes, 12.5 mL of 0.25 g PVP in EG was added to the flask then finally 4 mL of 282 mM AgTFA in EG was added to the reaction flask. The reaction was left to run for an additional 75 min. The reaction was quenched by putting the flask on ice bath immediately. Then, the product was collected by adding acetone to the reaction mix (5:1) and centrifugation at 6000 rpm for 10 min, followed by with water at 14000 rpm for 15 minutes. The resulting pellet was resuspended in 10 ml of H₂O for future use. The pre-synthesized AgNC was used as a template for galvanic replacement reaction. During galvanic replacement, 500 ul of pre-synthesized PVP-passivated AgNCs (2 mg/ml, 3nM) was added to 10 ml of boiling water. Then specific volume of 1 mM HAuCl₄ was titrated at the rate of 0.5 ml/min to the solution. UV-Vis spectrophotometer was used to monitor the LSPR peak of Ag-AuNCs. Once desired wavelength was reached, the Ag-AuNCs were put on ice bath for few minutes to stop the reaction. The reaction was decanted to remove precipitated AgCl at the bottom of the flask. Then reaction mix was transferred to 50 mL centrifuge tube and saturated by NaCl. After 15-20 minutes, the nanoparticles were collected by centrifugation at 11,000 rpm for 25 minutes, then purified with

water by three series of centrifugation at 14,000 rpm for 15 minutes. The Ag-AuNCs were stored at 4 °C for further characterization and use.

4.3.2 Material characterization

TEM images were taken using a transmission electron microscope (JEOL JEM-1011) with an accelerating voltage of 100 kV. The hydrodynamic diameters and ζ -potentials of the products were measured using a dynamic light scattering (DLS) instrument (Brookhaven ZetaPALS). The concentrations of Ag and Au were determined using an inductively coupled plasma mass spectrometer (Thermo Scientific iCAP Q ICP-MS). UV-vis spectra were taken on a UV-vis spectrophotometer (Agilent Cary50).

4.3.3 Antimicrobial evaluation of Ag-AuNCs

The antimicrobial activities of Ag-AuNCs of different molar ratios were investigated using an *E. coli* K-12 strain (MG1655) transformed with a plasmid encoding enhanced green fluorescent proteins (EGFPs) and ampicillin resistance. Overnight growth of the bacteria at 37 °C in 6 mL of Luria broth (LB) medium supplemented with ampicillin was done in a shaking incubator at 250 rpm. After the culture was diluted in 40 mL of fresh LB medium to reach OD₆₀₀ = 0.05. Ag-AuNCs suspensions were added to the fresh culture aliquots (1 mL) to reach final concentrations of 0 (negative control; without nanoparticles), 20, 40, 60, and 80 $\mu\text{g}/\text{mL}$. 96-well clear bottom microplates were used for growth curve assay where they were first sterilized by incubating the wells with 200 proof ethanol for 5 min and then exposed to UV light at 254 nm for 15 min. Each of the lids of the microplates was coated with 4 ml of Triton X-100 (0.05%) in 20% ethanol to avoid water condensation during measurement.⁴⁰ Then Triton solution was poured off and microplates were then air-dried before use. For growth curve measurement, 200 μL of the bacterial

cultures (with or without nanocages) was transferred to the microplate wells and the covered microplates were placed in a microplate reader (BioTek Synergy H1 Hybrid) to monitor both the fluorescence (excitation = 488 nm; emission = 525 nm) and the optical density (OD) at 600 nm of the bacteria in the wells. LB (200 μ L) medium supplemented with ampicillin were used as blanks. Measurements were obtained every 10 min for 48 h at 37 $^{\circ}$ C and rotating at 355 rpm. Each sample was measured with 4–6 replicates. The time series of the fluorescence-based growth curves for each sample was obtained by subtracting the mean of the fluorescence of the blanks at each time point from the mean of the fluorescence of the sample.

4.4. Results and Discussion

Synthesis of Ag- AuNCs

During the galvanic replacement reaction, the HAuCl_4 is used as a precursor for Au and AgNCs were used as a template for synthesis of Ag-Au nanocages. AgNCs of edge length of 35 nm according to TEM (**Figure 1A**) was synthesized using a polyol method and was used as a template to make the Ag-Au alloy nanocages with chloroauric acid. The driving force for the galvanic replacement reaction is the electrochemical potential differences between Ag^+/Ag and Au^+/Au . $\text{AuCl}_4^-/\text{Au}$ (0.99 V vs. SHE) is more positive than that of AgCl/Ag (0.22 V vs. SHE). Thus, Ag nanocubes can as a template (cathode) for the reaction.^{23, 24}

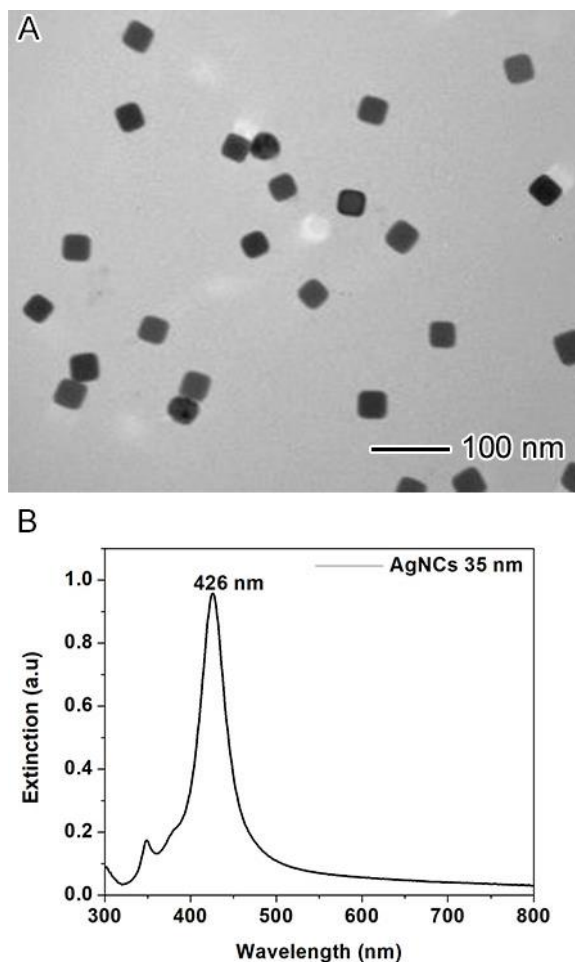


Figure 1: (A) TEM image of AgNCs synthesized to be used for galvanic replacement; and (B) UV-Vis spectrum of the AgNCs aqueous suspension corresponding to the sample shown in (A).

The mechanisms of galvanic replacement are well established and can be summarized in four stages that were illustrated in **Figure 2**. It starts with initiation of Ag dissolution from a site with poor protection, such as defects on the side face of a cube with sharp corners or the corners of a cube with truncated corners.^{41, 42} The second stage is when bulk Ag dissolve from the interior of the particle through the initial sites and concurrent deposition of Au on the rest of the surface.^{42, 43} After that a nanobox with uniform wall thickness forms due to alloying between Ag and Au. Lastly, Ag on (111) facets are dealloyed to generate pores on the walls of the nanobox, which eventually leads to the formation of Ag-Au nanocages. The LSPR of the Ag-Au nanocages was

tuned by changing the molar ratio of AgNCs to HAuCl_4 . The volume of 1 mM HAuCl_4 titrated to AgNCs solution was changed to make Ag-AuNCs of different molar ratios between Ag to Au in the nanocages. By controlling the volume of Au precursor added, the LSPR peaks of resulted Ag-AuNCs nanocages were tuned from 430 nm to NIR as the molar ratio of Ag to Au decreased. The LSPR was tuned to control the pore size of the resulting nanocages.

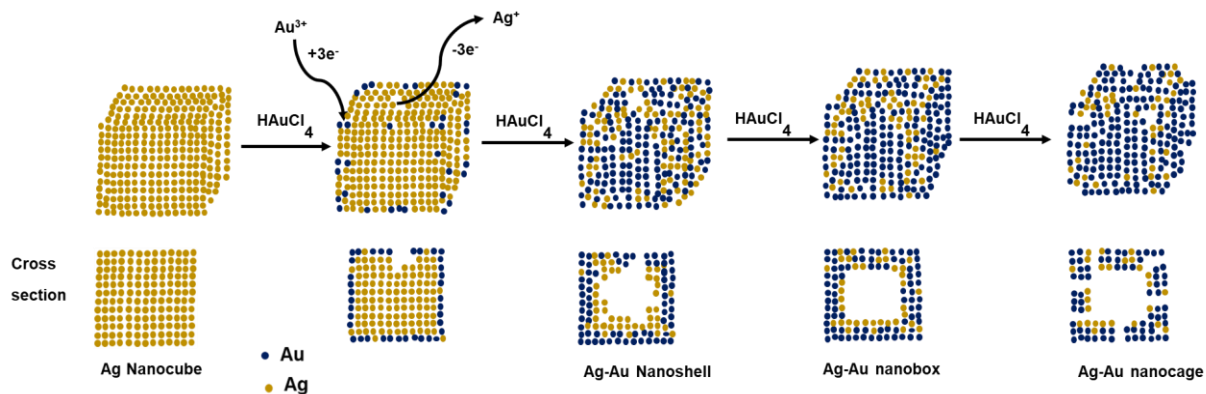


Figure 2: Schematic representation of galvanic replacement for synthesis of Ag-Au alloy nanocages using AgNCs as a template with chloroauric acid.

As shown in **Table 1**, six samples of Ag-AuNCs with various Ag/Au molar ratios (Ag-AuNCs 450nm, Ag-AuNCs 500nm, Ag-AuNCs 600nm, Ag-AuNCs 700nm, Ag-AuNCs 800nm, and Ag-AuNCs 900nm) were synthesized respectively with the addition of 1 mL, 1.3 mL, 1.5 mL, 2.2 mL, 2.9 mL, and 3.4 mL of 1mM HAuCl_4 solution to the same concentration of AgNCs. The concentration of Ag and Au were determined by ICP-MS. The LSPR peak red shift was observed by change in colors from yellow-reddish brown-purple-blue-to purple confirmed the transformation from nanocubes to nanocages (**Figure 3**).

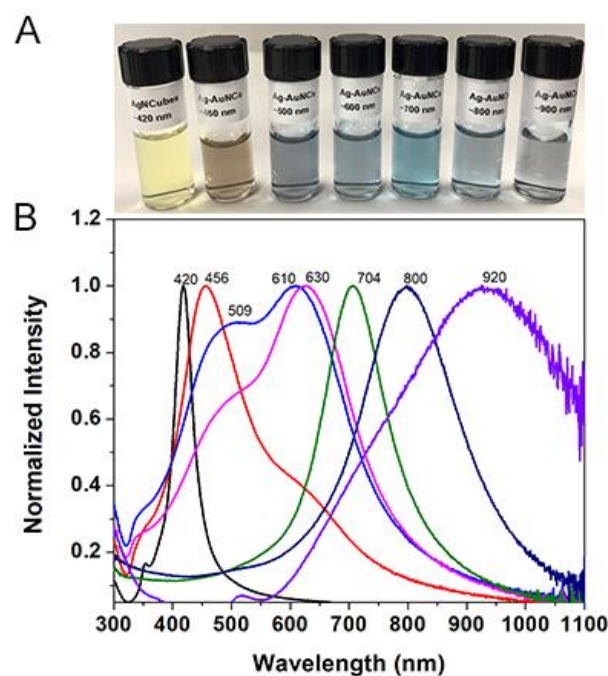


Figure 3: Ag/Au alloy nanocages of different mole ratios of Ag and Au. (A) Photograph of the Ag/Au nanocages showing change in color as wavelength was tuned from UV to infrared. (B) UV-Vis spectra of Ag/Au nanocages tuned to different wavelengths by increasing the amount of H_{AuCl}₄.

Table 1: Table showing Ag-Au nanocages with different molar concentrations ratio of Ag and Au in the nanocages.

Ag-AuNC samples	Ag (at %)	Au (at %)
AgNCs	100	0.00
Ag-AuNC ~450 nm	92.99	7.04
Ag-AuNC ~500 nm	75.08	24.91
Ag-AuNC ~600 nm	70.07	29.92
Ag-AuNC ~700 nm	46.44	53.55
Ag-AuNC ~800 nm	36.64	65.35
Ag-AuNC ~900 nm	13.16	86.83

The hollow structures of the nanocages can be observed with TEM images where higher LSPR peak show more hollow structure and porous walls (**Figure 4**). It was observed that Ag-AuNCs 900 nm have smaller nanoparticles which could be broken cages (**Figure 4F**). The hollow interior and porous walls of the nanocages was more pronounced at high wavelength (**Figure 4E, F**). In addition, DLS and zeta potential of the Ag-AuNCs of different mole ratios of Ag to Au were performed in aqueous suspensions. Hydrodynamic diameters explained the process happening where it starts with Ag dissolving from the structure as the Au deposition creating hollow structures. Dealloying of Ag as more HAuCl_4 was added to the solution creates defect and truncated corners that is indicated by smaller hydrodynamic diameter (D_h) around 75 nm for Ag-AuNCs 600 nm. The dealloying process observed was described by Erlebacher et al.⁴⁴ More Au deposition created thicker wall, hence bigger D_h to 95 nm for Ag-AuNCs 800 nm (**Table 2**). Interestingly, Ag-AuNCs 900 nm showed D_h of 150 nm, and this can be due to small nanoparticles (observed in Figure 4F) that tend to be agglomerated in the suspension. The zeta potential showed negatively charged surfaces of the nanocages that reduced from -9 mV to -5 mV as HAuCl_4 was added to the AgNPs which was observed before.³

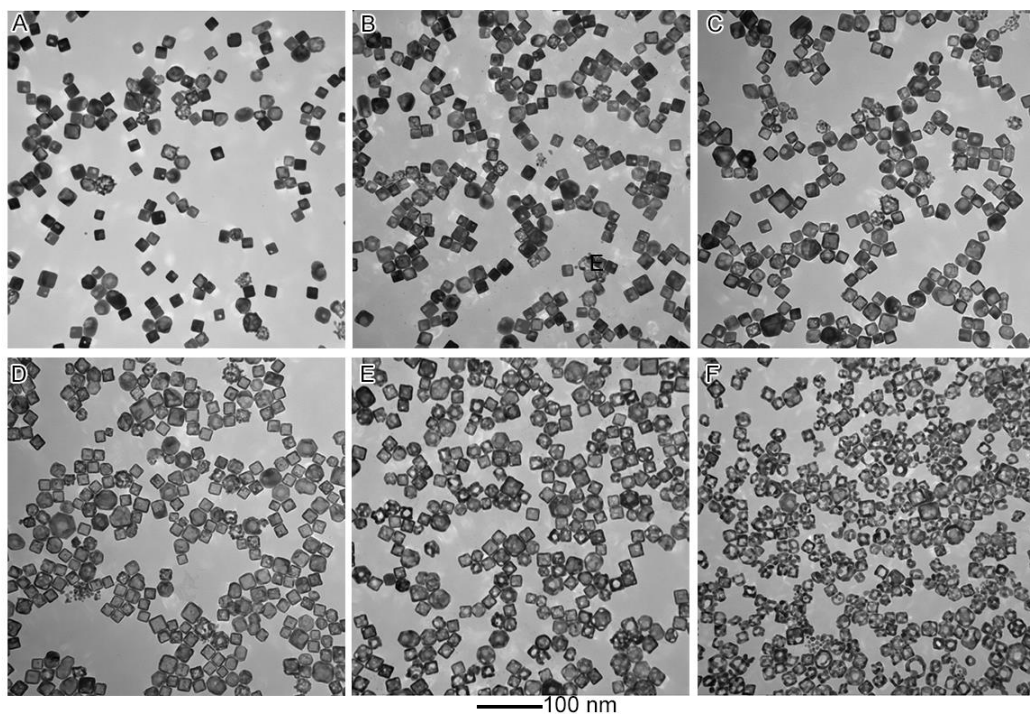


Figure 4: TEM images of Ag/Au nanocages of different molar ratio and different pore sizes. (A) AgAuNC 450 nm, (B) AgAuNC 500 nm, (C) AgAuNC 600 nm, (D) AgAuNC 700 nm, (E) AgAuNC 800 nm and (F) AgAuNC 900 nm.

Table 2: Summary of characterization of Ag-Au alloy nanocages.

Sample ID	LSPR (nm)	Hydrodynamic diameter, Dh (nm)	Zeta potential (mV)
AgNCs	420	136	-9.35±1.10
Ag-AuNC ~450 nm	455	93.5	-9.35±1.07
Ag-AuNC ~500 nm	509 and 610	86.3	-11.39±0.18
Ag-AuNC ~600 nm	630	75.6	-10.74±1.73
Ag-AuNC ~700 nm	704	81.5	-9.99±1.05
Ag-AuNC ~800 nm	800	95.7	-10.95±1.15
Ag-AuNC ~900 nm	920	150.9	-5.52±0.95

Antimicrobial evaluation of Ag-AuNCs against *E. coli*

The antimicrobial activities of Ag-AuNCs of different Ag/Au molar ratios on *E. coli* was investigated using fluorescence-based growth curves. *E. coli* was treated with different concentrations (0, 20, 40, 60, 80 and 100 $\mu\text{g/mL}$) of Ag-AuNCs of different Ag/Au molar ratios (**Table 1**). The antimicrobial activity of these nanostructures was found to be concentration-dependent where highest concentration of Ag-AuNCs used (100 $\mu\text{g/mL}$) presented the highest effect on inhibition of the bacteria growth (**Figure 5**) for all set of the samples. All of Ag-AuNCs display some degrees of bacterial inhibition effects, but Ag-AuNCs 600 nm and Ag-AuNCs 700 nm suppress the bacteria after 48 hr incubation up to 100 $\mu\text{g/mL}$.

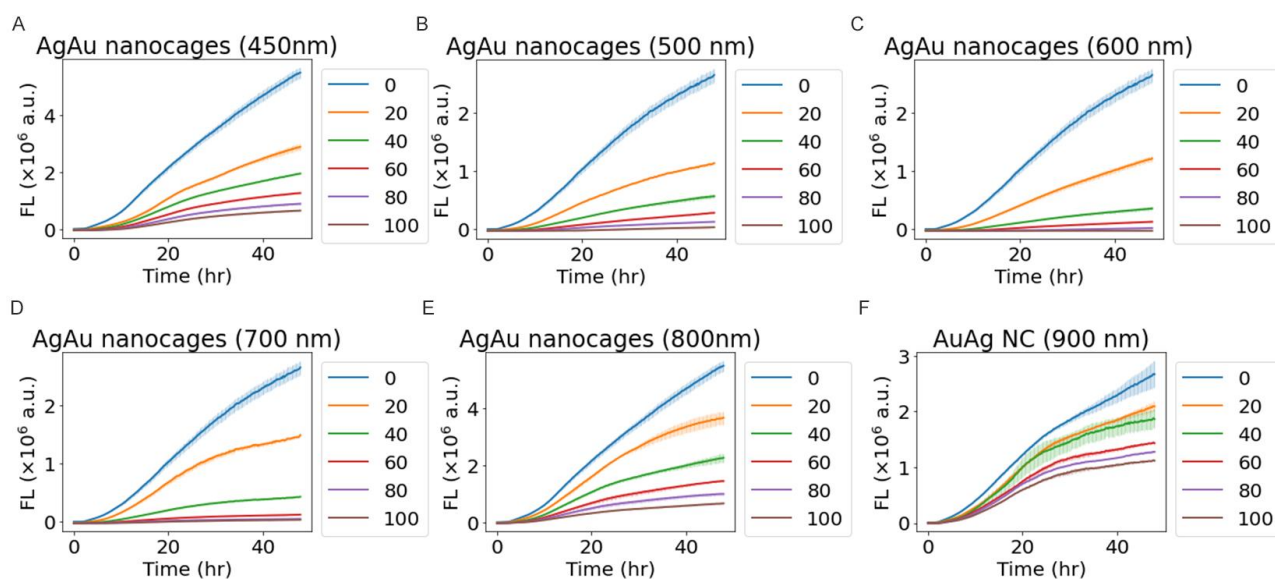


Figure 5: Fluorescence-based growth curves of the bacteria treated with Ag-Au nanocages with different concentration. (A) Ag-Au nanocages 450 nm, (B) Ag-Au nanocages 500 nm, (C) AgAu nanocages 600 nm, (D) AgAu nanocages 700 nm, (E) Ag-Au nanocages 800 nm, and (F) AgAu nanocages 900 nm. The fluorescence curves are shown as a function of time at different concentrations of 0 $\mu\text{g/mL}$ (untreated, negative control, blue lines), 20 $\mu\text{g/mL}$ (orange lines), 40 $\mu\text{g/mL}$ (green lines), 60 $\mu\text{g/mL}$ (red lines), 80 $\mu\text{g/mL}$ (violet lines), and 100 $\mu\text{g/mL}$ (purple lines).

AgNPs are known for high antimicrobial performance against *E. coli* that is better than AuNPs⁴⁵, but Ag-Au alloy nanoparticles exhibited high activity.^{45, 46} Therefore, one can expect

decreasing Ag/Au molar ratio in Ag-AuNCs would decrease their antimicrobial activity. When compared different ratios of Ag to Au, it was expected that antimicrobial performance of Ag-AuNCs would decrease as molar ratio of Ag/Au decreases according. However, we observed a different trend. The antimicrobial effectiveness of Ag-AuNCs followed the order of Ag-AuNC 700 nm > Ag-AuNC 600 nm > Ag-AuNC 500 nm > Ag-AuNC 450 nm > Ag-AuNC 800 nm > Ag-AuNC 900 nm (**Figure 5**). In addition, Ag-AuNCs 600 and 700 showed better antimicrobial activity than both pure AgNPs and AuNPs (**Figure 6**) especially at high concentration showing almost complete inhibition of bacteria growth. This suggest that the great antimicrobial activities of Ag-AuNCs observed is not an additive effect from Gaps and AuNPs rather a synergistic effect.

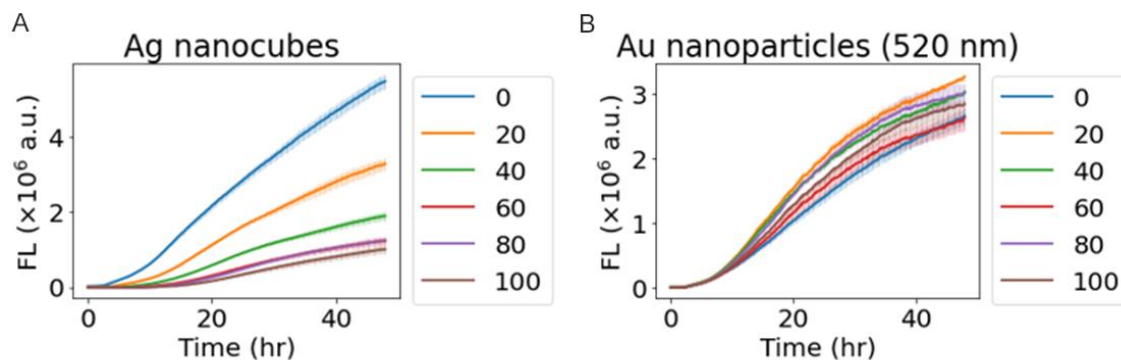


Figure 6: Fluorescence-based growth curves of the bacteria treated with (A) Ag nanocubes of 35 nm edge length and (B) Au nanoparticles with LSPR at 520 nm and 15 nm edge length. The fluorescence curves are shown as a function of time at different concentrations of 0 $\mu\text{g/mL}$ (untreated, negative control, blue lines), 20 $\mu\text{g/mL}$ (orange lines), 40 $\mu\text{g/mL}$ (green lines), 60 $\mu\text{g/mL}$ (red lines), 80 $\mu\text{g/mL}$ (violet lines), and 100 $\mu\text{g/mL}$ (purple lines).

The high antimicrobial activity of Ag-AuNCs 600 nm (**Figure 5C**) and Ag-AuNCs 700 nm (**Figure 5D**) observed compared to pure AgNCs and other tested Ag-AuNCs can be explained by the structural differences of these alloy nanostructures that vary from nanoshell to nanobox then to nanocage depending on the stage of the galvanic replacement (**Figure 2**). Wang et al. found out

that Ag-AuNCs of Ag/Au mass concentration ratio of 2.5 exhibited the greatest inhibition of bacteria growth for different strains of bacteria including *E. coli* compared to Ag-AuNCs with higher Ag/Au ratios and pure AgNCs.³ One can explain the antimicrobial performance to the structural properties of the Ag-Au alloy nanostructures which depends on the stage of the galvanic replacement stage; starting from nanoshell to more hollow structures/nanobox to nanocage (**Figure 2**) as more H₂AuCl₄ is added. It is possible that when alloying is not completed the Ag⁺ ions be easily leached in the media and be the source of inhibited bacteria growth observed for Ag-AuNC 600 nm and Ag-AuNC 700 nm. The easily released Ag in the suspension can possibly make the Ag-AuNCs 600 and 700 nm more effective compared to the rest of the nanocages. Ag-AuNCs 700 nm has almost equimolar ratios of Ag to Au which can explain the nanobox structures with uniform walls (**Figure 2**). When the alloying is not complete the Ag can easily be released from the structure, as it was reported that Au-Ag alloy nanoparticles are stable and resist oxidation.⁴⁷ One can suspect that dealloying process of Ag atoms at the later stage of galvanic replacement would result in alloy with more Au than Ag, hence less antimicrobial activity, which explains lower antimicrobial activity of Ag-AuNCs 800 nm (**Figure 5E**) and Ag-AuNCs 900 nm (**Figure 5F**).

In addition, Ag and Au of different shapes and sizes were synthesized and their antimicrobial properties against *E. coli* were studied to evaluate the effect of shape on antimicrobial properties of these nanoparticles. Three shapes were evaluated: cubic, triangular plates and stars. Smaller AgNPs have more antimicrobial potency compared to bigger NPs (**Figure S1 B, D and F**). The size effect has been explored before and our results agrees with the literature.⁴⁸⁻⁵¹ The antimicrobial of the nanostructures showed a shape-dependent effect. For Ag nanoparticles, when nanocubes were compared to nanoplates, there was no significant difference in their antimicrobial performance (**Figure S5**) which was used to the difference in sizes (**Figure**

S2) where AgNCs used had 33 nm edge lengths while Ag nanoplates were 62 nm. The data suggests that in case of smaller Ag nanoplates than what was used, the antimicrobial performance would be higher which would agree with the literature.⁵²⁻⁵⁴ For Au nanostructures, all tested Au nanocubes and Au nanoplates showed very high antimicrobial activity against *E. coli* especially at high concentration where they completely inhibited the bacteria growth (**Figure S6 A-D**). Au nanostars exhibited little to no antimicrobial effect even at high concentration of nanoparticles used (100 µg/mL) (data not shown). To investigate the mechanisms behind high antimicrobial performances of the Au nanoplates and nanocubes of various sizes, we investigated on the surface ligand effect. As control, the antimicrobial properties of CTAB and CTAC were studied when *E. coli* was treated with different concentrations (0,1,2,4,6,8,10, and 20 µg/mL) of CTAB and CTAC. Both the Au nanocubes and nanoplates were prepared using CTAB and CTAC as surfactants. It was found that surface chemistry of nanoparticles played a big effect on antimicrobial performance of the nanoparticles as both CTAB and CTAC show a high antimicrobial activity at low concentrations with complete inhibition of the bacterial growth at 20 µg/ml (**Figure S6 E and F**). The high antimicrobial activity of CTAC played part in antimicrobial activity of Au nanostructures. For instance, Au nanostructures show the antimicrobial activity close to that of Ag nanoparticles because of the additive effect of CTAC that was used as a surfactant. In addition, the attempt to replace CTAC by PVP on Au nanoplates did not improve its antimicrobial since even small concentration of CTAC still show great antimicrobial performance. Therefore, great antimicrobial activities of Au nanostructures are mostly from the surface ligand (CTAC and CTAB) rather than the nanoparticles themselves. Antimicrobial of CTAB has been studied before and the mechanisms was associated with ROS generation.⁵ Low antimicrobial activity of AuNPs was observed regardless of shape and size.

4.5. Conclusion

In this chapter, Ag-Au nanocages of different Ag/Au molar ratios were synthesized using a simple reaction of galvanic replacement. AgNCs of 35 nm in edge length were used as a template for the reaction to make nanocages with tuning LSPR peaks to different wavelengths and controlling hollow structures and pore sizes of the nanocages. The antimicrobial performance of the nanocages was evaluated using fluorescence-based growth curves on *E. coli*. Ag-AuNCs 600 nm (75 at % Ag and 25 at% Au) and Ag-AuNCs 700 nm (46 at % Ag and 53 at% Au) showed better antimicrobial activities compared to pure AgNPs and other tested Ag-AuNCs. The antimicrobial performance of the Ag-AuNCs is thought to be dependent on the structures of the nanocages which vary with different Ag/Au molar ratios that is determined by the stage of the galvanic replacement from pure nanocubes to alloyed nanoshell to nanobox then to nanocages. It was thought that Ag⁺ ions could be easily released from the Ag-AuNC 600 and 700 nm in case of incomplete alloying in these two samples which could inhibit bacteria growth more than pure AgNPs or completely alloyed nanocages. The mechanistic details of the observed synergistic effect between Au and AgNCs in these nanocages is being explored at the molecular level to further understand the effect of Ag and Au composition on Ag-AuNCs' antimicrobial properties. The antimicrobial data of Ag and Au NPs of different shapes and sizes supported that Ag-AuNCs' great antimicrobial properties come from Ag or synergistic effects of Ag and Au due to controlled release of Ag because AuNPs did not have any antimicrobial activity if ligand (CTAC) effect was eliminated.

4.6. References

1. S. Marin, G. M. Vlasceanu, R. E. Tiplea, I. R. Bucur, M. Lemnaru, M. M. Marin and A. M. Grumezescu, *Current Topics in Medicinal Chemistry*, 2015, **15**, 1596-1604.
2. M. K. Peiris, C. P. Gunasekara, P. M. Jayaweera, N. D. H. Arachchi and N. Fernando, *Memorias Do Instituto Oswaldo Cruz*, 2017, **112**, 537-543.
3. Y. Wang, J. Wan, R. J. Miron, Y. Zhao and Y. Zhang, *Nanoscale*, 2016, **8**, 11143-11152.
4. K. Tomankova, J. Horakova, M. Harvanova, L. Malina, J. Soukupova, S. Hradilova, K. Kejlova, J. Malohlava, L. Licman, M. Dvorakova, D. Jirova and H. Kolarova, *Food Chem Toxicol*, 2015, **82**, 106-115.
5. K. Nakata, T. Tsuchido and Y. Matsumura, *J Appl Microbiol*, 2011, **110**, 568-579.
6. S. Kittler, C. Greulich, J. Diendorf, M. Köller and M. Epple, *Chemistry of Materials*, 2010, **22**, 4548-4554.
7. D. Tiedemann, U. Taylor, C. Rehbock, J. Jakobi, S. Klein, W. A. Kues, S. Barcikowski and D. Rath, *Analyst*, 2014, **139**, 931-942.
8. J.-P. Kaiser, M. Roesslein, L. Diener, A. Wichser, B. Nowack and P. Wick, *Journal of nanobiotechnology*, 2017, **15**, 5-5.
9. W. H. De Jong, L. T. Van Der Ven, A. Sleijffers, M. V. Park, E. H. Jansen, H. Van Loveren and R. J. Vandebriel, *Biomaterials*, 2013, **34**, 8333-8343.
10. J. Ma, X. Lü and Y. Huang, *Journal of Biomedical Nanotechnology*, 2011, **7**, 263-275.
11. R. J. Vandebriel, E. C. M. Tonk, L. J. de la Fonteyne-Blankestijn, E. R. Gremmer, H. W. Verharen, L. T. van der Ven, H. van Loveren and W. H. de Jong, *Particle and Fibre Toxicology*, 2014, **11**, 21.
12. B. Hu, N. Wang, L. Han, M.-L. Chen and J.-H. Wang, *Acta biomaterialia*, 2015, **11**, 511-519.
13. M. Banerjee, S. Sharma, A. Chattopadhyay and S. S. Ghosh, *Nanoscale*, 2011, **3**, 5120-5125.
14. Z. Lu, J. Zhang, Z. Yu, X. Liu, Z. Zhang, W. Wang, X. Wang, Y. Wang and D. Wang, *New Journal of Chemistry*, 2017, **41**, 5276-5279.
15. S. Shankar, L. Jaiswal, R. S. L. Aparna and R. G. S. V. Prasad, *Materials Letters*, 2014, **137**, 75-78.

16. C. W. Chen, C. Y. Hsu, S. M. Lai, W. J. Syu, T. Y. Wang and P. S. Lai, *Adv Drug Deliv Rev*, 2014, **78**, 88-104.
17. C. Fasciani, M. J. Silvero, M. A. Anghel, G. A. Argüello, M. C. Becerra and J. C. Scaiano, *Journal of the American Chemical Society*, 2014, **136**, 17394-17397.
18. M. S. Yavuz, Y. Cheng, J. Chen, C. M. Cobley, Q. Zhang, M. Rycenga, J. Xie, C. Kim, K. H. Song, A. G. Schwartz, L. V. Wang and Y. Xia, *Nat Mater*, 2009, **8**, 935-939.
19. D. G. Meeker, S. V. Jenkins, E. K. Miller, K. E. Beenken, A. J. Loughran, A. Powless, T. J. Muldoon, E. I. Galanzha, V. P. Zharov, M. S. Smeltzer and J. Y. Chen, *Acs Infectious Diseases*, 2016, **2**, 241-250.
20. J. Yang, Y. Zhao, J. Cao, C. Gong, J. Zuo, N. Zhang and Y. Zhao, *International Journal of Pharmaceutics*, 2020, **586**, 119505.
21. T. Bai, P. Lu, K. Zhang, P. Zhou, Y. Liu, Z. Guo and X. Lu, *Journal of Biomedical Nanotechnology*, 2017, **13**, 1178-1209.
22. S. V. Jenkins, T. D. Gohman, E. K. Miller and J. Y. Chen, *Journal of Chemical Education*, 2015, **92**, 1056-1060.
23. S. E. Skrabalak, J. Chen, Y. Sun, X. Lu, L. Au, C. M. Cobley and Y. Xia, *Accounts of Chemical Research*, 2008, **41**, 1587-1595.
24. Y. Xia, W. Li, C. M. Cobley, J. Chen, X. Xia, Q. Zhang, M. Yang, E. C. Cho and P. K. Brown, *Acc Chem Res*, 2011, **44**, 914-924.
25. Y. Xia and D. J. Campbell, *Journal of Chemical Education*, 2007, **84**, 91.
26. D. Kumar, S. Bala, H. Wadhwa, G. Kandhol, S. Mahendia, F. Chand and S. Kumar, *AIP Conference Proceedings*, 2019, **2093**, 020048.
27. J. R. Daniel, L. A. McCarthy, E. Ringe and D. Boudreau, *RSC Advances*, 2019, **9**, 389-396.
28. Y. Sun and Y. Xia, *Science*, 2002, **298**, 2176-2179.
29. Z. Qin, Y. Zheng, T. Du, Y. Wang, H. Gao, J. Quan, Y. Zhang, Y. Du, L. Yin, X. Wang and H. Jiang, *Chemical Engineering Journal*, 2021, **414**, 128779.
30. P. Makvandi, C. Y. Wang, E. N. Zare, A. Borzacchiello, L. N. Niu and F. R. Tay, *Advanced Functional Materials*, 2020, **30**, 40.
31. B. Ruozi, P. Veratti, M. A. Vandelli, A. Tombesi, M. Tonelli, F. Forni, F. Pederzoli, D. Belletti and G. Tosi, *Int J Pharm*, 2017, **518**, 281-288.

32. D. G. Meeker, T. Wang, W. N. Harrington, V. P. Zharov, S. A. Johnson, S. V. Jenkins, S. E. Oyibo, C. M. Walker, W. B. Mills, M. E. Shirliff, K. E. Beenken, J. Chen and M. S. Smeltzer, *International journal of hyperthermia : the official journal of European Society for Hyperthermic Oncology, North American Hyperthermia Group*, 2018, **34**, 209-219.
33. X. Jiang, X. Fan, W. Xu, R. Zhang and G. Wu, *ACS Biomaterials Science & Engineering*, 2020, **6**, 680-689.
34. R. Lima, F. S. Del Fiol and V. M. Balcão, *Front Pharmacol*, 2019, **10**, 692.
35. J. Liu, D. A. Sonshine, S. Shervani and R. H. Hurt, *ACS Nano*, 2010, **4**, 6903-6913.
36. S. Panicker, I. M. Ahmady, C. Han, M. Chehimi and A. A. Mohamed, *Materials Today Chemistry*, 2020, **16**, 100237.
37. P. N. H. Diem, T. N. M. Phuong, N. Q. Hien, D. T. Quang, T. T. Hoa and N. D. Cuong, *Journal of Nanomaterials*, 2020, **2020**, 7195048.
38. Q. Li, F. Lu, H. Ye, K. Yu, B. Lu, R. Bao, Y. Xiao, F. Dai and G. Lan, *ACS Sustainable Chemistry & Engineering*, 2018, **6**, 9813-9821.
39. Q. A. Zhang, W. Y. Li, L. P. Wen, J. Y. Chen and Y. N. Xia, *Chemistry-a European Journal*, 2010, **16**, 10234-10239.
40. J. D. Brewster, *Journal of Microbiological Methods*, 2003, **53**, 77-86.
41. M. Hu, J. Chen, Z.-Y. Li, L. Au, G. V. Hartland, X. Li, M. Marquez and Y. Xia, *Chemical Society Reviews*, 2006, **35**, 1084-1094.
42. Y. Sun and Y. Xia, *Journal of the American Chemical Society*, 2004, **126**, 3892-3901.
43. J. Chen, F. Saeki, B. J. Wiley, H. Cang, M. J. Cobb, Z.-Y. Li, L. Au, H. Zhang, M. B. Kimmey, X. Li and Y. Xia, *Nano Letters*, 2005, **5**, 473-477.
44. J. Erlebacher, M. J. Aziz, A. Karma, N. Dimitrov and K. Sieradzki, *Nature*, 2001, **410**, 450-453.
45. A. I. El-Batal, M. Abd Elkodous, G. S. El-Sayyad, N. E. Al-Hazmi, M. Gobara and A. Baraka, *International Journal of Biological Macromolecules*, 2020, **165**, 169-186.
46. S. Basu, P. Maji and J. Ganguly, *Journal of Experimental Nanoscience*, 2016, **11**, 660-668.
47. D. M. Mott, D. T. N. Anh, P. Singh, C. Shankar and S. Maenosono, *Advances in Colloid and Interface Science*, 2012, **185-186**, 14-33.
48. S. Agnihotri and S. Mukherji, *Rsc Advances*, 2014, **4**, 3974-3983.

49. S. Alqahtani, P. Promtong, A. W. Oliver, X. T. T. He, T. D. Walker, A. Povey, L. Hampson and I. N. Hampson, *Mutagenesis*, 2016, **31**, 695-702.
50. V. D. Badwaik, L. M. Vangala, D. S. Pender, C. B. Willis, Z. P. Aguilar, M. S. Gonzalez, R. Paripelly and R. Dakshinamurthy, *Nanoscale Research Letters*, 2012, **7**, 11.
51. O. Choi and Z. Q. Hu, *Environmental Science & Technology*, 2008, **42**, 4583-4588.
52. A. Alshareefa, K. Laird and R. B. M. Cross, *Applied Surface Science*, 2017, **424**, 310-315.
53. T. Ghoshal, M. C. Cruz-Romero, J. P. Kerry and M. A. Morris, *Acs Applied Nano Materials*, 2019, **2**, 6325-6333.
54. J. Helmlinger, C. Sengstock, C. Gross-Heitfeld, C. Mayer, T. A. Schildhauer, M. Koller and M. Epple, *Rsc Advances*, 2016, **6**, 18490-18501.

4.7. Appendix: Supplemental information: Effect of shape on antimicrobial properties of Ag and Au nanostructures.

4.7.1. Synthesis of Ag nanostructures of different shapes and size

Synthesis of Ag nanocubes

Ag nanocubes (AgNCs) of small size (around 25 nm) were synthesized using a modified protocol developed from the literature.^{1,2} In this protocol, the polyol method is adapted with diethylene glycol (DEG) as a solvent and reducing agent instead of ethylene glycol (EG). In this protocol, 5 mL of DEG was heated to 150 °C in an oil bath in 25 mL round bottom three-neck flask. Then 0.06 mL of 3 mM NaHS was added. After 4 minutes, 0.5 mL of 3 mM HCl was added followed by injection of 1.25 mL of PVP (MW = 55,000, 20 mg/mL) after 2 minutes. Finally, 0.4 mL of CF₃COOAg solution (282 mM) was introduced. After adding all reagents to the reaction flask, the reaction was capped and run for 30 minutes. The reaction mix was quenched in an ice bath. Nanoparticles were collected by centrifugation at 14,000 rpm for 15 min then purified in water with 2 cycles of centrifugations at 14,000 rpm for 10 minutes.

AgNCs of bigger edge lengths (>50 nm) were synthesized using smaller seed particles as a template in a seed-mediated synthesis.^{2,3} The Ag seeds (around 30 nm average edge length) were prepared using the established polyol method.¹ Then, AgNPs of greater edge lengths were prepared following procedure from J. Am. Chem. Soc 132 (32), 2010.⁴ During the seed-mediated synthesis, 5 mL of EG was put in an 8 mL glass vial and heated in an oil bath to 150 °C under magnetic stirring and 1.2 mL of PVP (20 mg/ml) was added. After 10 min, 50, 100, 200, or 400 μL of Ag seeds (32 nm, 10 nM) was added, followed by the addition of 800 μL of AgNO₃ (282 mM) to make AgNCs of 125, 100, 75, and 50 nm edge length, respectively. The reaction was stopped after 4 hr. The reaction mixtures for each synthesis were quenched by putting the vial in

an ice bath. Then, the product was washed in acetone (5:1 ratio) and water three times at 14000 rpm for 15 minutes and 10 minutes for the last two washes. The final pellets were dispersed in water for future use.

Synthesis of Ag nanoplates

Ag nanoplates (AgNPs) synthesis was done using a modified literature protocol.⁵ Typically, the total volume of the reaction solution was fixed to 25.00 mL. In 24.04 mL of pure water, an aqueous solution of silver nitrate (0.05 M, 50 μ L), sodium citrate (75 mM or 17.5 mM, 0.5 mL), poly (vinylpyrrolidone) (PVP, weight-average molecular weight $M_w \sim 8,000$ g/mol 75 mM, 0.1 mL), and H_2O_2 (30 wt%, 60 μ L) were combined and vigorously stirred at room temperature in air. Sodium borohydride ($NaBH_4$, 100 mM, 250 μ L) was rapidly injected into this mixture to produce the nanoplates. After ~ 3 min, the colloid changed to a deep-yellow color due to the formation of small silver nanoparticles. Within 30 minutes, the morphology continued to change from seed particles to nanoplates, accompanied by the solution color change from yellow to deep blue. The nanoparticles were put in 1.5 mL Eppendorf tubes and washed by 2 cycles of centrifugation at 14,000 rpm for 10 minutes each cycle.

4.7.2. Synthesis of Au nanostructures of different shapes and sizes

Synthesis of Au nanocubes

Au nanocubes were synthesized using the modified protocol from Park et al. 2018.⁶ The reaction was done in three steps. The first step was synthesis of gold seeds that are used to make nanospheres that are later converted into nanocubes.

Synthesis of gold seeds capped with CTAB

Au seeds capped with cetyltrimethylammonium bromide (CTAB) were first prepared by adding 250 μ L of 10 mM tetrachloroauric acid ($HAuCl_4$) solution to 9.75 mL of 100 mM CTAB

solution in a 50 mL round-bottom flask. Subsequently, 600 μL of freshly made ice-cold 10 mM sodium borohydride (NaBH_4) solution was added quickly. The solution was mixed with a stirring bar for 3 min and stored at 21 $^\circ\text{C}$ for 3 h before the next step. The seeds were used as they were for the next step.

Synthesis of Au nanospheres

The prepared CTAB nanosphere seeds were used to make bigger nanospheres that are used for synthesis of Au nanocubes. In an experiment to make big seeds (nanospheres), a 20 mL vial was used and 2 mL of 200 mM, cetyltrimethylammonium chloride (CTAC), 1.5 mL of 100 mM ascorbic acid, and 50 μL of the previously prepared seeds solution were mixed sequentially. Then, 2 mL of a 0.5 mM HAuCl_4 solution was injected while the solution was being mixed with a constant speed of 500 rpm. The solution was incubated at room temperature for 15 min with constant stirring. The solution was washed by centrifugation twice, first redispersed in 1 mL 18 M Ω water and then in 1 mL of a 20 mM CTAC solution for future use (13000 rpm, 30 min).

Synthesis of Au nanocubes of different sizes

6 mL of 100 mM CTAC was mixed with 30 μL of sodium bromide (20 mM NaBr). A defined volume of freshly prepared seeds was added depending on the desired size (less seeds produced big nanocubes). The previously prepared Au nanospheres were diluted to the final concentration of 22.7 pM. Then, 30 μL , 9 μL or 2 μL of the diluted seed solution (22.7 pM) was added to 390 μL of a 10 mM ascorbic acid solution and mixed thoroughly to make 100 nm, 50 nm and 30 nm Au nanocubes, respectively. Finally, 6 mL of a 0.5 mM HAuCl_4 solution was added with one shot while the solution was being mixed with a stirring bar at 500 rpm. The solution was

incubated for 25 min with mixing, followed by centrifugation and redispersion in 18 M Ω water twice, respectively at 14,000 rpm for 15 minutes.

Synthesis of Au nanotriangles (Au NTs)

Au nanotriangles were synthesized by following the protocol developed by Scarabelli et al. 2014.⁷ The synthesis was done in two steps: Synthesis of Au capped with CTAC (Au@CTAC seeds) then growth nanotriangles from the seeds.

Synthesis of Au@CTAC seed

In this step, 25 μ L of 50 mM HAuCl₄ solution was added to 4.7 mL of a 0.1 M CTAC solution and stirred for 3 min. Then, 300 μ L of freshly prepared NaBH₄ 10 mM solution was injected while stirring. The seed solution was left for 2 hr before we could be used to grow the nanotriangles.

Growth of Au nanotriangles capped with CTAC (Au NTs@CTAC)

To grow Au nanotriangles, 2 solutions (A and B) were prepared. To prepare Solution A, 8mL H₂O, 1.6 mL of 0.1 M CTAC solution, and 40 μ L of 50 mM HAuCl₄ solution were combined in 20 mL vial. Solution B was prepared by mixing 78 mL of 0.05 M CTAC, 978 μ L of 50 mM HAuCl₄, and 588 μ L of 10 mM NaI solutions in 250 mL round bottom flask. After preparing and mixing all solutions well, the initial CTAC seeds were diluted 10 times in 0.1 M CTAC solution. Then, 40 μ L of 100 mM ascorbic acid solution was added to Solution A and 780 μ L of 100 mM ascorbic acid solution was added to Solution B—the solution was previously shaken until it was colourless. 400 μ L of the diluted Au@CTAC seeds were added to Solution A and shaken until it became colourless. Then the entire Solution A was immediately poured into Solution B and shaken. Everything was left undisturbed for 3 hr. The colour was initially strongly pink, but it changed to purple and finally blue. To change the size of the nanotriangles, the volume of solution

A injected in solution B in the final step was varied—small volume of seeds was used to make large AuNTs and vice versa.

PVP-coating of Au NTs (AuNTs@PVP)

The capping agent was changed from CTAC to PVP. In this ligand-exchange reaction, Au NTs@CTAC were centrifuged at 4000 rpm for 15 min and the pellet was dispersed in 50 μ L of a 0.1 M CTAC solution and sonicated. Then PVP (1 mg/mL) final concentration was added to the Au NTs@CTAC with vigorous stirring. This solution was stirred overnight at room temperature. The nanoparticles were washed by a series of centrifugation at 14000 rpm for 15 minutes.

Synthesis of Au nanostars

Au nanostars were synthesized using protocol developed by Xi W. et al.⁸ The synthesis of nanostars was performed by the reduction of chloroauric acid (HAuCl_4) by 4-(2-hydroxyethyl)-piperazine-1-ethanesulfonic acid (HEPES) buffer. In a typical synthesis, the pH of a 40 mM HEPES stock solution was adjusted to 7.48 (± 0.01) using 1 M NaOH: The HEPES solution was stirred in a 250 mL round-bottom flask for 1 min. 200 μ L of a 20 mM HAuCl_4 solution was then added to 20 mL of the HEPES stock solution and gently stirred for 30 min. The solution was placed in the dark at RT for 1 hr to promote the nanostars' growth. The Au nanostar solutions were centrifuged for 30 minutes at 4610 rpm, redispersed in 20 mM and then 10 mM HEPES and stored at 4 °C until use.

4.7.3. Evaluation of antimicrobial properties of the Ag and Au nanostructures

The same protocol that was described in section 4.3.3 was used to evaluate the effect shape of Ag and Au nanostructures of different shapes on growth of *E. coli*. The 96 well plates were used for fluorescence measurements at 37 °C. The samples were preheated to the next step. The samples

were run for total 48 hours with 10 minutes intervals. There were 289 total reads, and the reading was continuous. During the measurements, the samples were shaken at a constant speed at 205 rpm (5 mm). Fluorescence measurements were run at excitation wavelength at 488 nm and emission wavelength at 525 nm.

4.7.4. Characterization of Ag and Au nanostructures of different shapes and their antimicrobial properties

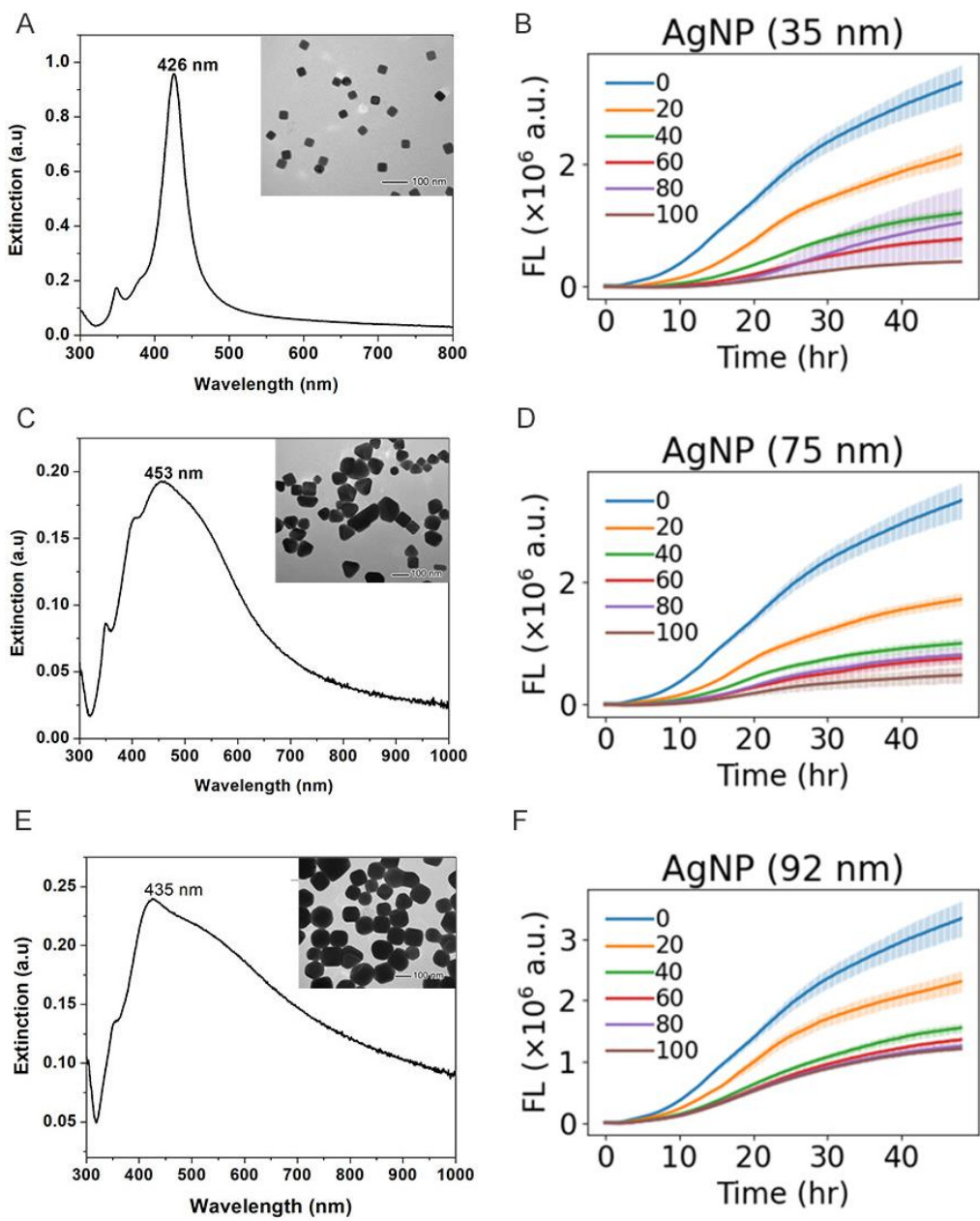


Figure S1: UV-Vis spectra of (A) AgNP 35 nm (C) AgNP 75 nm and (E) AgNP 92 nm with inserts showing TEM image of corresponding AgNPs with a 100 nm scale bar. Fluorescence-based growth curves of the bacteria treated with (B) AgNP 35 nm, (D) AgNP 75 nm, and (F) AgNP 92 nm.

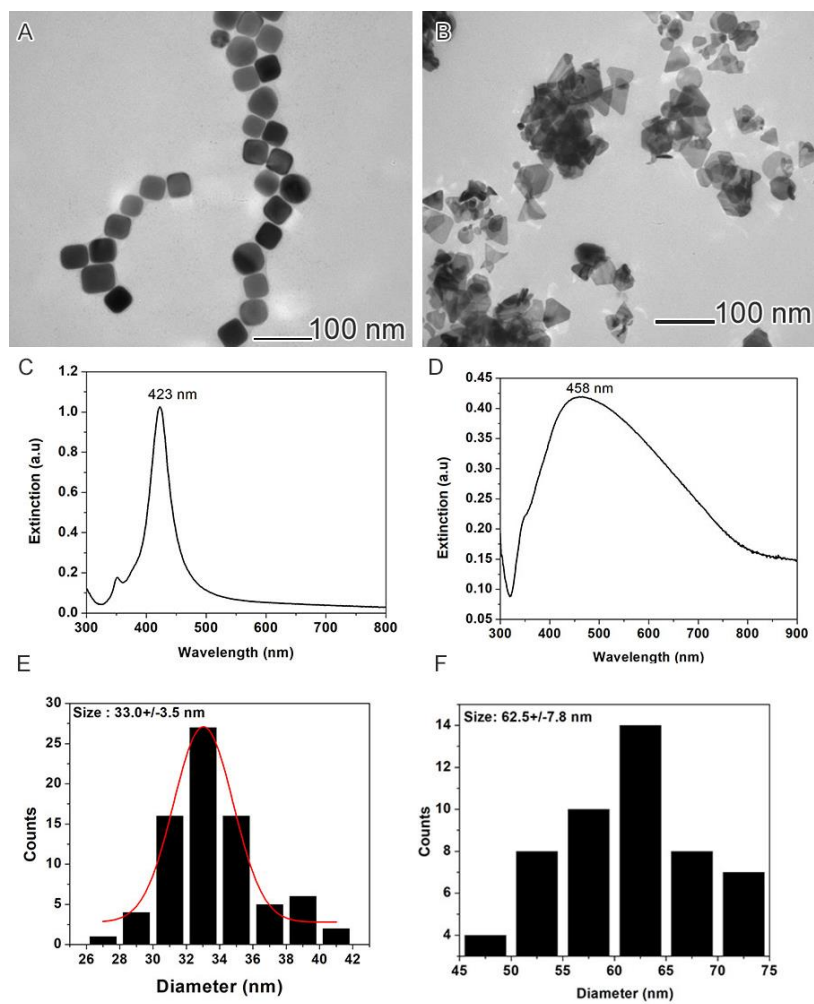


Figure S2: TEM images of (A)Ag nanocubes; and (B)Ag nanoplates. UV-Vis spectra of Ag nanocubes (C) shown in (A) and Ag nanoplates (D) represented in (B) Size distribution of (E) Ag nanocubes and (F) Ag nanoplates.

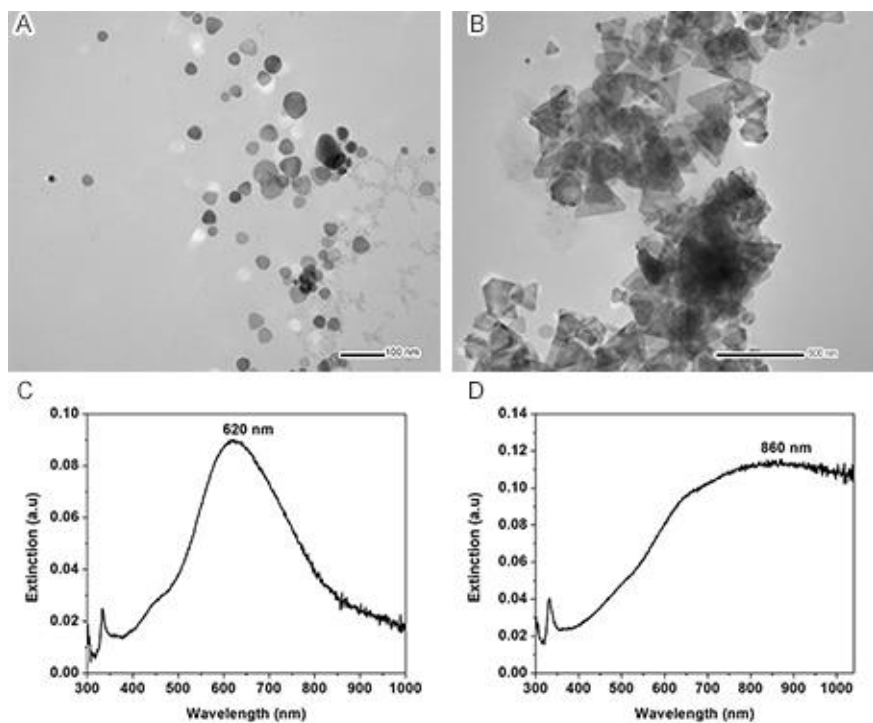


Figure S3: TEM images of (A) Ag nanoplates of 35 nm edge length synthesized with 75 mM PVP (scale bar is 100 nm) and (B) of Ag nanoplates of 58 nm edge length synthesized with 17.5 mM PVP (scale bar is 500 nm). UV-Vis spectra of (C) Ag nanoplates (35 nm) and (D) Ag nanoplates of 58 nm edge length.

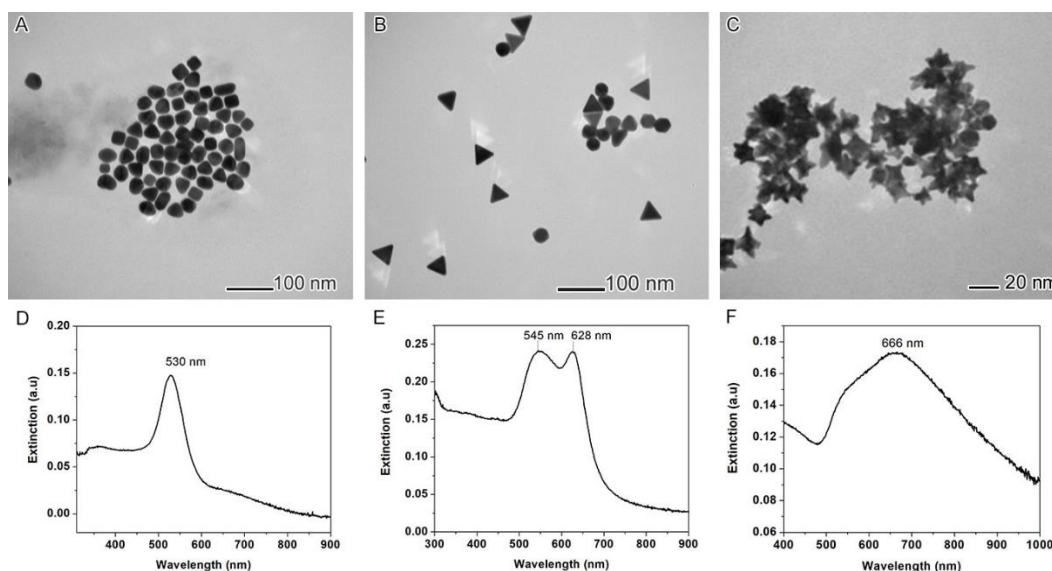


Figure S4: (A-C) TEM images of Au nanoparticles of different shapes. (A) Au nanocubes, (B) Au nanotriangles and (C) Au nanostars. (D-F) UV-Vis spectra of Au nanostructures: Au nanocubes (D), Au nanotriangles (E) and Au nanostars (F).

Table S1: Summary of characterization of Ag and Au nanostructures.

Samples	Size, from TEM (nm)	Hydrodynamic Diameter (nm)	Zeta Potential (mV)	Surface/surfactant
Au Nanocubes	42	118.2 ± 15.9	-5.10	CTAC
Au Nanoplates	36	154.8 ± 10.0	-26.68	CTAC+PVP
Au Nanoplates	47	114.6 ± 1.5	-8.33	CTAC+PVP
Au nanostars	30	118.2 ± 4.4	-9.46	HEPES
Ag nanocubes	35	134.8 ± 2.0	-7.68	PVP
Ag nanoplates	33	135.0 ± 0.9	-11.13	PVP+CITRATE

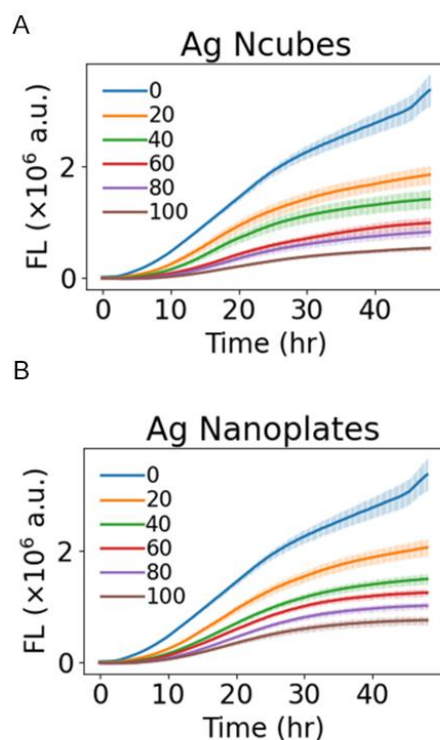


Figure S5: Fluorescence-based growth curves of the bacteria treated with (A) Ag nanocubes, (B) Ag nanoplates. The fluorescence curves are shown as a function of time at different concentrations of 0 $\mu\text{g/mL}$ (untreated, negative control, blue lines), 20 $\mu\text{g/mL}$ (orange lines), 40 $\mu\text{g/mL}$ (green lines), 60 $\mu\text{g/mL}$ (red lines), 80 $\mu\text{g/mL}$ (violet lines), and 100 $\mu\text{g/mL}$ (purple lines).

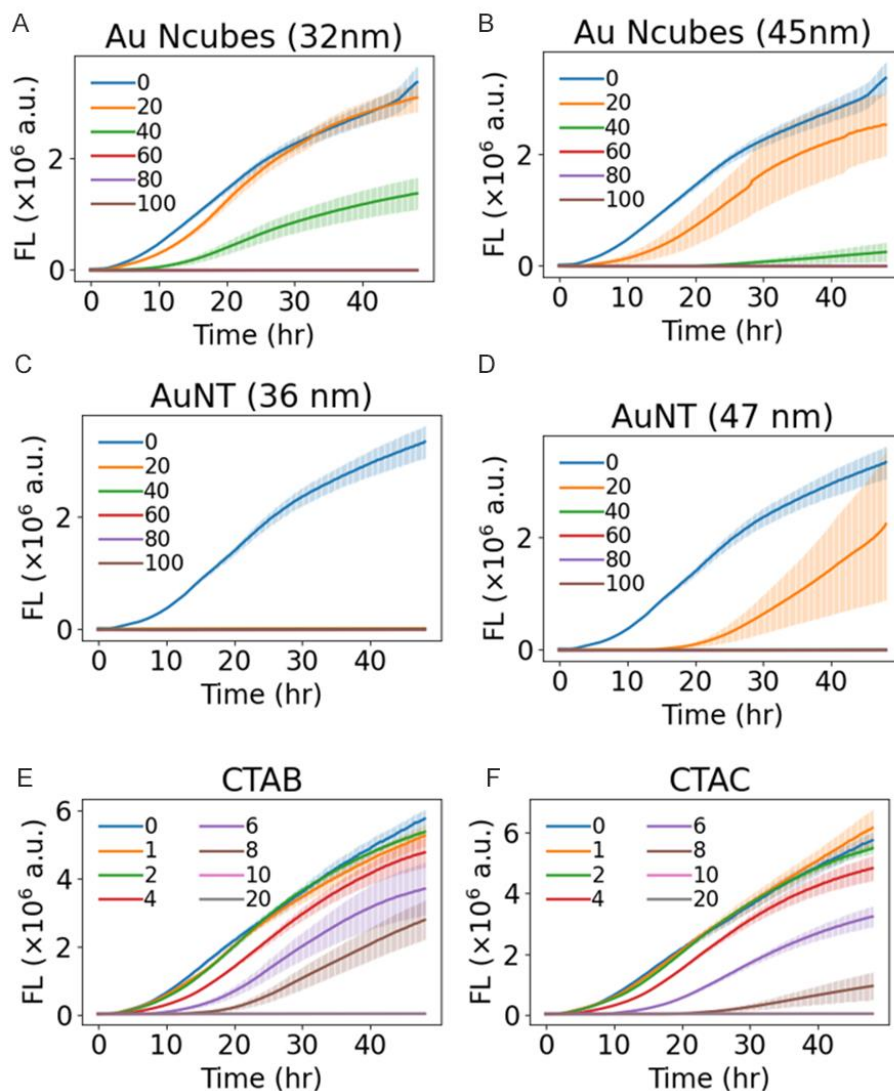


Figure S6: Fluorescence-based growth curves of the bacteria treated with Au nanostructures of different shapes. (A) Au nanocubes 45 nm ; (B) Au nanocubes of 45 nm edge length, (C) Au nanotriangular plates (AuNT 36 nm), (D) Au nanotriangular plates (AuNT 47 nm), (E) CTAB used as a surfactant and (F) CTAC (surfactant). The fluorescence curves are shown as a function of time at different concentrations of 0 $\mu\text{g/mL}$ (untreated, negative control, blue lines), 20 $\mu\text{g/mL}$ (orange lines), 40 $\mu\text{g/mL}$ (green lines), 60 $\mu\text{g/mL}$ (red lines), 80 $\mu\text{g/mL}$ (violet lines), and 100 $\mu\text{g/mL}$ (purple lines).

4.8. References

1. Y. Wang, Y. Q. Zheng, C. Z. Huang and Y. N. Xia, *Journal of the American Chemical Society*, 2013, **135**, 1941-1951.
2. Q. A. Zhang, W. Y. Li, L. P. Wen, J. Y. Chen and Y. N. Xia, *Chemistry-a European Journal*, 2010, **16**, 10234-10239.
3. I. I. Niyonshuti, V. R. Krishnamurthi, D. Okyere, L. Song, M. Benamara, X. Tong, Y. Wang and J. Chen, *ACS Applied Materials & Interfaces*, 2020, **12**, 40067-40077.
4. Q. A. Zhang, W. Y. Li, C. Moran, J. Zeng, J. Y. Chen, L. P. Wen and Y. N. Xia, *Journal of the American Chemical Society*, 2010, **132**, 11372-11378.
5. Q. Zhang, N. Li, J. Goebel, Z. D. Lu and Y. D. Yin, *Journal of the American Chemical Society*, 2011, **133**, 18931-18939.
6. J. E. Park, Y. Lee and J. M. Nam, *Nano Letters*, 2018, **18**, 7419-7419.
7. L. Scarabelli, M. Coronado-Puchau, J. J. Giner-Casares, J. Langer and L. M. Liz-Marzan, *Acs Nano*, 2014, **8**, 5833-5842.
8. W. J. Xi and A. J. Haes, *Journal of the American Chemical Society*, 2019, **141**, 4034-4042.

Chapter V: Conclusion and Future Work

This research consists of two parts with Part I focusing on synthesis of PEG-based hydrogels for wound healing applications and Part II centering on Ag and Ag/Au alloy nanostructures for antimicrobial applications. This chapter concludes the study of each part and its future work, as well as lays out the possible directions for the combination of the two parts.

In Part I, PEG-based anionic hydrogels P(OEGA-AA-NIPAM) were designed and synthesized in an effort for sustained release of the positively charged proteins. Vibrational spectroscopic studies confirmed that all the monomers were polymerized and crosslinked in the hydrogel. Increasing the concentration of AA in the copolymer has led to increased thermal stability. The AA functional group provided the negatively charges to the hydrogel for control release of positively charged proteins such as lysozyme through electrostatic interactions, but little effect on negatively charged proteins such as BSA. In the absence of NIPAM, the electrostatic interaction of hydrogel and hFGF1 is too strong resulting in the retention of most hFGF1 encapsulated in the hydrogel for prolong period. Incorporating NIPAM in the hydrogel net reduces the charge density of the hydrogel, thereby facilitating the control release of hFGF1 in a short period of time relevant to the need of wound healing applications. The release profile of hFGF1 from P(OEGA-AA-NIPAM) was increased by 6 folds compared to P(OEGA-co-AA) hydrogel. An in vivo animal study supported the P(OEGA-AA-NIPAM) hydrogel-controlled delivery of hFGF1 for a faster wound closure compared to the control group. Wounds that were treated with hydrogel loaded with hFGF1 closed faster than control (hydrogels alone) over a period of 10 days. The significant difference in wound closure was more pronounced on days 3 and 5 of wound healing which ensured that hFGF1 released was still active and acted in proliferation phase

of wound healing process. Hydrolytic degradation studies show that the hydrogel is partially degradable with 55% degradation rate in 40 days. This work promises a hydrogel system with tunable charge distribution which gives control over controlled delivery of a wide range of positively charged proteins with preserved bioactivity. Future work will continue to explore the possibilities of making the injectable hydrogels biodegradable which would provide additional tuning knob to control the release the entrapped proteins depending on their degradation rates. The biodegradation with a reasonable rate can be achieved by using crosslinkers with easily breakable bonds such as ester^{1, 2} and polysaccharide like chitosan^{3, 4}, or bonds susceptible to enzymatic degradation⁵⁻⁷ with metalloproteinase enzymes present at the wound sites such as collagenase.

Part II investigated the effects of surface chemistry, morphology, and composition of AgNPs and Ag/AuNCs on their antimicrobial properties. Positive charged PEI-AgNPs improved the antimicrobial efficacy of these nanoparticles by causing reorganization of H-NS protein of *E. coli* compared to negatively charged PVP-passivated AgNPs. Further study showed synergistic effect of PDA and AgNPs to enhance antimicrobial properties due to the coordination between Ag and catechol groups of the PDA coating, which leads to ROS generation and cell wall destruction. Finally, the antimicrobial properties of Ag-AuNCs were evaluated. Different molar ratios of Ag/Au were used and Ag-AuNCs 600 nm (75 at % Ag and 25 at% Au) and Ag-AuNCs 700 nm (46 at % Ag and 53 at% Au) exhibited higher antimicrobial activity than pure AgNPs and Ag-AuNCs of higher Ag/Au molar ratios. Au enhanced antimicrobial activity of AgNPs at a certain Ag/Au molar ratio which could be attributed to the controlled release of Ag due to the formation of alloy. In depth studies on structural and morphological properties of these alloyed nanoparticles will provide insights on the Au and Ag synergistic effect on antimicrobial activity of the metal NPs.

There is potential for combining the knowledge learnt from two parts of this dissertation to make a nanocomposite hydrogel. Hydrogels can be synthesized in presence of AgNPs, which will provide increased crosslinking and enhanced mechanical strength to the nanocomposite hydrogel.^{8, 9} For instance, in case Ag-Au NPs coated with PDA are used, the surface functionalization would provide more interactions between polymer and Ag/AuNPs.¹⁰ Ag-AuNPs would also provide light sensitivity while polymers like PNIPAM provide stimuli responsiveness to the nanocomposite hydrogel.¹¹⁻¹⁴ The nanocomposite hydrogel could then exert excellent drug delivery properties than can be tuned depending on the drug of interest. This nanocomposite hydrogel can be tested for antimicrobial activity and its dual responsiveness (light and temperature) can be of advantage for drug delivery of antibiotics.

References

1. K. M. Eckes, K. Baek and L. J. Suggs, ACS Omega, 2018, 3, 1635-1644.
2. S. Murakami, N. Aoki and S. Matsumura, Polymer Journal, 2011, 43, 414-420.
3. Z. Li and Z. Lin, Aggregate, 2021, 2, e21.
4. S. M. F. Kabir, P. P. Sikdar, B. Haque, M. A. R. Bhuiyan, A. Ali and M. N. Islam, Progress in biomaterials, 2018, 7, 153-174.
5. R. J. Wade, E. J. Bassin, C. B. Rodell and J. A. Burdick, Nature communications, 2015, 6, 6639-6639.
6. T. Sedlačák, H. Studenovská and F. Rypáček, J Mater Sci Mater Med, 2011, 22, 781-788.
7. S. Amar, L. Smith and G. B. Fields, Biochimica et Biophysica Acta (BBA) - Molecular Cell Research, 2017, 1864, 1940-1951.
8. A. K. Gaharwar, N. A. Peppas and A. Khademhosseini, Biotechnology and bioengineering, 2014, 111, 441-453.
9. C. Balazs Anna, T. Emrick and P. Russell Thomas, Science, 2006, 314, 1107-1110.
10. F. Caruso, Advanced Materials, 2001, 13, 11-22.

11. M. A. Haq, Y. Su and D. Wang, *Materials Science and Engineering: C*, 2017, 70, 842-855.
12. M. Lehmann, P. Krause, V. Miruchna and R. von Klitzing, *Colloid and Polymer Science*, 2019, 297, 633-640.
13. S. Ashraf, H.-K. Park, H. Park and S.-H. Lee, *Macromolecular Research*, 2016, 24, 297-304.
14. S. Shekhar, M. Mukherjee and A. K. Sen, *Polymer Bulletin*, 2016, 73, 125-145.